

ABSTRACT

Title of Document: ATOMIC LAYER DEPOSITION OF SOLID
ELECTROLYTES FOR BEYOND LITHIUM-ION
BATTERIES

Alexander Campbell Kozen, Doctor of Philosophy, 2015

Directed By: Professor Gary W. Rubloff, Department of Materials
Science & Engineering

This thesis outlines methodology and development of an atomic layer deposition (ALD) process for the well-known solid-state electrolyte lithium phosphorous oxynitride (LiPON). I have developed a quaternary ALD LiPON process through a novel stepwise additive development procedure. ALD process kinetics and chemistry were investigated using *in-operando* spectroscopic ellipsometry and *in-situ* x-ray photoelectron spectroscopy (XPS). ALD LiPON exhibits a tunable ionic conductivity proportional to N content, with the highest conductivity of 6.5×10^{-7} S/cm at 16.3% N.

Two applications of ALD LiPON are investigated: ALD LiPON films as a protection layer for next-generation lithium metal anodes in the lithium sulfur battery system, and as solid electrolytes in 3D thin film batteries with discussion towards development of an all ALD 3D battery.

Lithium metal is considered the “holy grail” of battery anodes for beyond Li-ion technologies, however, the high reactivity of Li metal has until now prevented its commercial use. Here, ALD protection layers are applied directly to the Li anode to

prevent chemical breakdown of the liquid electrolytes while allowing ion transport through the protection layer. Protection of lithium metal is investigated with two materials: low ionic conductivity ALD Al_2O_3 , demonstrating a 60% capacity improvement in Li-S batteries by protecting the Li anode from sulfur corrosion during cycling, and high ionic conductivity ALD LiPON, demonstrating a 600% improvement in Li-S battery capacity over unprotected anodes. Interestingly, ALD LiPON also forms a self-healing protection layer on the anode surface preventing deleterious Li dendrite formation during high rate cycling.

Solid Li-based inorganic electrolytes offer two profound advantages for energy storage in 3-D solid state batteries: enhanced safety, and high power and energy density. Until now, conventional solid electrolyte deposition techniques have faced hurdles to successfully fabricate devices on challenging high aspect ratio structures, required for improvements in both device energy and power density. In this thesis, I demonstrate fabrication of ALD heterostructures suitable for use in 3D solid batteries, and although this work is incomplete I discuss progress towards future use of ALD LiPON solid electrolytes in all ALD solid-state 3D batteries.

ATOMIC LAYER DEPOSITION OF SOLID ELECTROLYTES FOR BEYOND
LITHIUM-ION BATTERIES

by

Alexander Campbell Kozen

Dissertation submitted to the Faculty of the Graduate School of the
University of Maryland, College Park in partial fulfillment
of the requirements for the degree of
Doctor of Philosophy
2015

Advisory Committee:
Professor Gary W. Rubloff, Chair
Professor Sang-Bok Lee
Professor Marina S. Leite
Professor Ichiro Takeuchi
Professor Christopher J. Lobb

© Copyright by
Alexander Campbell Kozen
2015

Acknowledgements

I would first like to profoundly thank Professor Gary Rubloff, who has been a tremendous role model and advisor throughout my years at Maryland. Thanks for encouraging me to pursue my crazy ideas, and for always making time for me despite your insanely busy schedule.

Thanks to my predecessors in the Rubloff research group who were instrumental in teaching me the necessary skills to succeed and helping me develop as a scientist and researcher: Dr. Laurent Lecordier, Dr. Parag Banarjee, Dr. Xinyi Chen, and Dr. Keith Gregorczyk.

Thanks to the current colleagues in the Rubloff research group, with whom I have spent many hours of toil, discussion, brainstorming: Dr. Malakhi Noked, Dr. Chuan-Fu Lin, Dr. Marshall Schroeder, Alex Pearse, and Chanyuan Liu.

Thanks to my friends and colleagues in the UMD Materials Science Department for many hours of discussion, complaining, and brainstorming: Elliot Bartis, Dr. Colin Gore, Amy Marquardt, Sean Fackler, and Dr. Norvik Voskanian.

Thanks to the FabLab staff, who keep the world on their shoulders: Dr. Jim O'Connor, Jon Hummel, Tom Loughran, John Abrahams, and Mark Lecates.

Thanks to the IREAP support staff, who make sure the lights stay on: Nolan Ballew, Jay Pyle, Don Martin, and Bryan Quinn.

Thanks to my committee members for their guidance, direction, and insight during the course of my research and during the progression of this thesis.

Thanks to my bandmates in BRNDA & Show Pony for giving me some slack and letting me take time off music to do Science.

None of this would have been possible without the love, support, and encouragement from my parents: Frances and Dexter, and my brothers: Geoff and Tim throughout my time in grad school.

Thanks to my wonderful girlfriend, Jen Shih, for all the support and understanding for my late nights working. I love you. I couldn't have done this without you. I bet you're not going to miss Saturday date night at the lab.

Lastly, thanks to my two cats: Pickles and Beta, for somehow knowing exactly the most inappropriate times to sit on my computer's keyboard

Finally, I would like to acknowledge my funding sources over the course of my Ph.D. This work has been supported in part by Nanostructures for Electrical Energy Storage (NEES), an Energy Frontier Research Center funded by the U.S. Department of Energy, Office of Science, Office of Basic Energy Sciences under award number DESC0001160.

Table of Contents

ABSTRACT	i
Acknowledgements	ii
Table of Contents	iv
Chapter I: Beyond Li-Ion Batteries	1
Motivation	1
Next Generation Materials	2
3D Nanobattery Architectures	4
Solid Nanoheterostructured Batteries	6
Atomic Layer Deposition (ALD)	8
Lithium Phosphorus Oxynitride (LiPON)	8
Next Generation Metal Anodes for Beyond Li-ion Batteries	10
ALD Solid Electrolyte Process Development Strategy	13
Chapter II: Laboratory Design, Equipment, and Experimental Methods	15
Ultraclean, Ultrahigh Vacuum System	15
Substrate Preparation	17
Atomic Layer Deposition (ALD)	18
ALD Additive Synthesis	18
X-ray Photoelectron Spectroscopy (XPS)	20
Spectroscopic Ellipsometry	20
Chapter III: ALD Li ₂ O Process Development	22
Introduction	22
Thermal ALD Using H ₂ O	22
Plasma ALD Using O ₂	27
Elucidating Hydration/Dehydration Reactions	28
Deconstructing the Air-Reactivity of Li ₂ O	31
High Aspect Ratio Deposition	34
Chapter Summary	36
Chapter IV: ALD Li ₃ PO ₄	37
Introduction	37
Process Development	37
ALD Li ₃ PO ₄ Characterization	38
External Characterization	39
Chapter Summary	40
Chapter V: ALD LiPON	41
Background	41
Stepwise Process Optimization	42
Chemical Characterization	47
ALD LiPON Ionic Conductivity Determination	55
CR2032 Coin Cells	56
Conductivity Measurements With Solid-State MIM Devices	58
Single Nanopore Conductivity Measurements	61

Chapter Summary	62
Chapter VI: Lithium Metal Protection with ALD Solid Electrolytes	64
Solid Electrolyte Interphase	64
ALD LiPON as an Artificial SEI Layer	64
LiPON For Silicon Electrode Stabilization	65
Lithium Metal Anode Protection	66
Motivation	67
Deposition of ALD Protection Coatings on Lithium Metal Anodes	69
Lithium Corrosion Prevention in Three Environments	71
Atmospheric Corrosion	71
Organic Solvent Corrosion	72
Sulfur/DME Corrosion	74
Lithiation Behavior of the Protected Anode	76
Lithium Sulfur Battery Testing	80
Lithium Dendrite Prevention via Self-Healing Protection Layers	86
Chapter Summary and Conclusions	89
Chapter VII: Solid 3D Battery Development	92
Motivation	92
ALD Solid Battery Fabrication Strategy	93
2D Device Fabrication	95
3D Device Fabrication	97
Nanocone Template	97
Lightsmyth Diffraction Grating Template	98
Future Outlook for ALD Sold State Batteries	99
Thesis Summary and Professional Output	101
Appendix: Experimental Parameters	103
Atomic Layer Deposition	103
Atomic Force Microscopy (AFM)	105
Battery Testing	106
Optical Image Analysis	107
X-Ray Diffraction (XRD)	107
Transmission Electron Microscopy (TEM)	108
Quadrupole Mass Spectroscopy (QMS)	108
Electrochemistry	109
X-ray Photoelectron Spectroscopy	110
Spectroscopic Ellipsometer	111
References	113

Chapter I: Beyond Li-Ion Batteries

Motivation

Over the past 25 years, the world's demand for greater energy storage capacity has increased exponentially, however battery technology has not achieved the same remarkable performance gains as have been achieved in the semiconductor industry.¹ This lack of advancement is due partially to slowing materials development, as well as a conservative risk-averse battery industry reluctant to introduce new materials technologies to the market. Currently, most Li-ion batteries consist of a graphitic carbon anode, an organic liquid electrolyte, and a LiCoO_2 cathode. Both electrodes are composed of micron-sized particles of active material mixed with conductivity enhancing additives and binders. A cartoon cross section of a conventional Li-ion battery is shown in Figure 1. While these batteries are cheap, and the performance is sufficient for practical use, significant opportunities exist to improve both the capacity and performance of Li-ion batteries.²

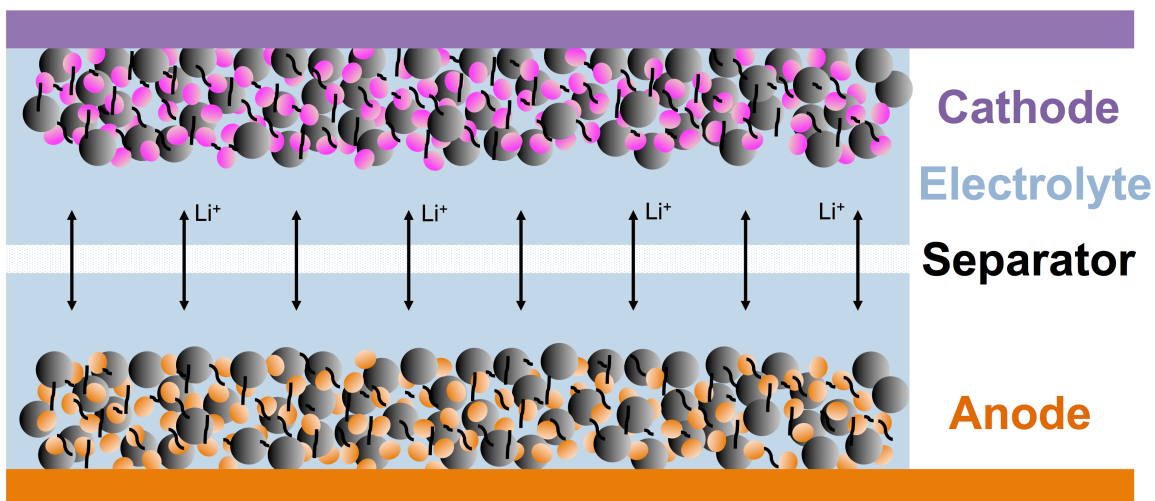


Figure 1. Cartoon of current Li-ion battery technology, showing aggregate anode and cathode composed of active material, binder, and conductive additives bathed in an organic electrolyte, and separated by a polymeric ion permeable separator.

Two of the most promising avenues for improving both gravimetric and volumetric energy density of batteries are by improving the battery materials themselves, and by changing the architecture and morphology of the battery electrodes.

Next Generation Materials

The capacity of both current and future Li-ion battery materials is summarized as a function of electrochemical potential vs. gravimetric capacity is shown in Figure 2. Currently commercialized batteries are limited by both the capacity of the graphite anode (372 mAh/g) and the LiCoO_2 cathode (300 mAh/g). On the cathode side, Li-rich nickel manganese cobalt oxide (LNMC) shows the most immediate commercialization promise as both a higher capacity and a higher voltage cathode material.^{3,4} Other promising cathode materials include gaseous O_2 ^{5,6} and elemental sulfur⁷, however fundamental chemistry issues currently prevent these battery systems from commercialization in the next 5 years.

On the anode side, both silicon (4200 mAh/g) and lithium metal (3850 mAh/g) represent the most promising high capacity anode materials, however they suffer from a number of challenges to widespread adoption.⁸ Silicon undergoes a massive volume expansion of ~400% when fully lithiated, and repeated cycling results in cracking and pulverizing of the material.⁹ Reducing the size of the silicon particles accommodates for the lithiation strain, however requires exotic processing techniques to realize nanostructured silicon.^{10,11}

The ideal anode for a lithium-based battery is pure Li metal, as it has a gravimetric capacity of 3840 mAh/g, and an electrochemical potential of 0V. Indeed the first Li-based batteries commercialized by Sony used Li metal anodes. However, after a number of spectacular failures due to Li dendrite formation these batteries were removed from the commercial market due to safety concerns. This phenomenon will be described further in Chapter VI.

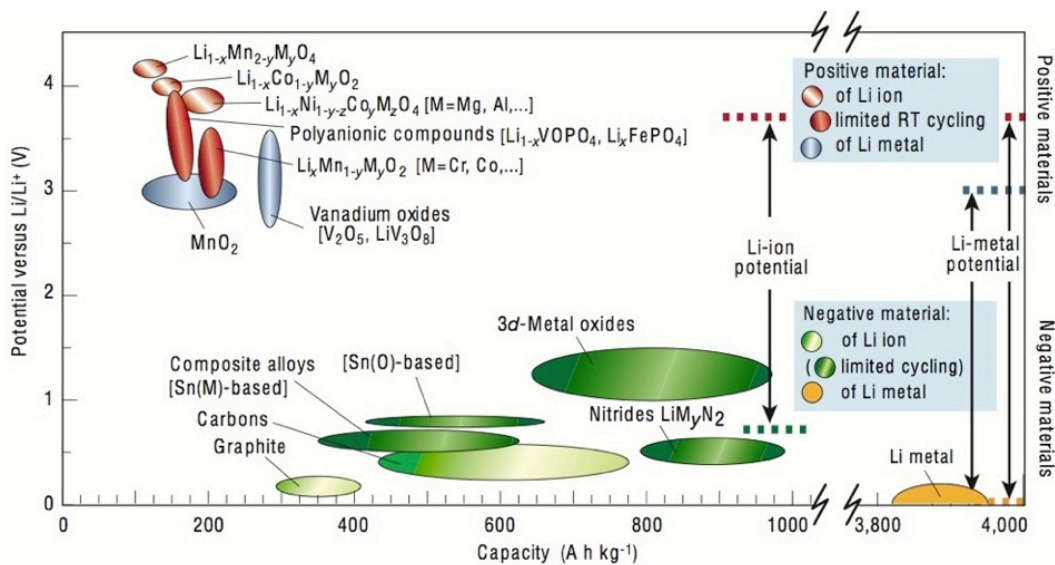


Figure 2. Summary of chemistries used as electrode materials for Li-based batteries. From Tarascon and Armand, *Nature*, 2001.¹²

3D Nanobattery Architectures

When incorporating high concentrations of charge-carrying ions, in this case Li^+ , into an anode or cathode material, a limiting factor is the ion transport kinetics of the diffusing ion. For a fixed diffusivity, D , of an ion in a material phase, the ion transport time, τ , varies as the square of the distance travelled, l^2 . In an electrode, this relationship means thicker storage layers require increasingly longer times for ion diffusion than thinner layers. The storage capacity of thicker layers can only be accessed at low charge and discharge rates, and the devices only achieve their full energy density (full lithiation) by sacrificing power capability. Yet, the need for power as well as energy is important - even critical - in many demanding energy storage applications such as defense and space applications.

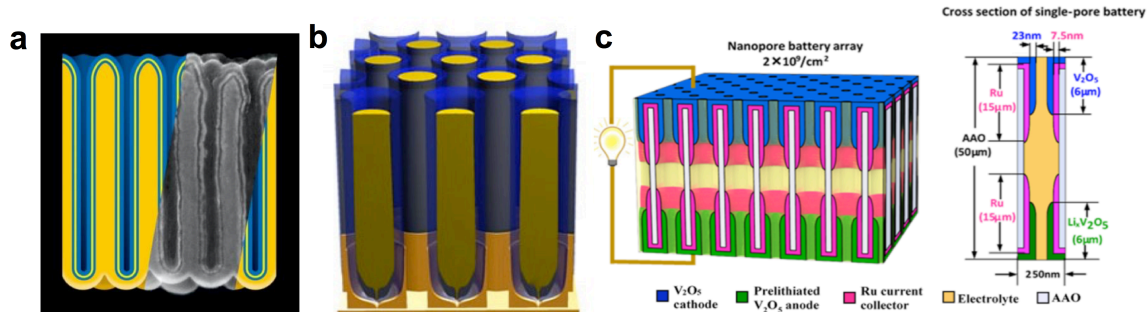


Figure 3. Example high aspect ratio 3D battery geometries. (a) interdigitated MIM electrostatic capacitor;¹³ (b) self-aligned electrodeposited electrochemical supercapacitor;¹⁴ (c) array of individual nanopore batteries.¹⁵

While chemistry is the determining factor affecting the lithiation behavior of electrochemical storage materials, experimental and computational studies have made critical advances in understanding and optimizing the chemistries of cathode materials such as oxides^{12 16-21} and anode materials such as carbons²² and silicon²³. Further device improvement can be realized through novel architectures, especially nanoheterostructured materials, which open the possibility of using thinner storage layers with much larger surface area to access ions in the electrolyte for high power operation.

The motivation and ability to create nanostructured electrodes for electrochemical energy storage has been recognized for some time^{10,24-35}, and recent advances in nano science and technology provide new capability to construct multicomponent nanostructures and storage devices.

Indeed, recent nanostructured energy storage systems have demonstrated the radical increase in both power density and gravimetric energy density of these nanoheterostructured systems³⁶⁻³⁸. As these devices approach the size limits of scalable architectures they indicate a need for new alignment, deposition, and patterning techniques to realize device performance³⁹. Atomic layer deposition (ALD) is ideally

suited to fabricate these next-generation nanostructures due to its low temperature deposition, highly conformal and tunable nature, and self-alignment to a nanopatterned scaffold⁴⁰⁻⁴³, all fundamental requirements for fabrication of nanoheterostructured batteries.

Solid Nanoheterostructured Batteries

Despite the high power and energy density realized by nanostructuring electrodes in conventional batteries, and even the nanopore battery array, it still includes a liquid electrolyte, which due to recent accidents involving battery overheating and subsequent failure underscore the importance of proper battery thermal management. This issue becomes especially important when using nanoheterostructured devices during high rate charge/discharge, as these devices may not be able to achieve long device lifetimes under high power operating conditions due to increased thermal and mechanical stress.

Additionally, liquid electrolytes suffer from formation of an insulating solid electrolyte interphase (SEI), which is caused by electrolyte breakdown at the active materials interface due to electron transfer mechanisms during charge/discharge⁴⁴. Clearly, replacement of liquid electrolytes with their solid counterparts is the ideal solution to both safety and device degradation challenges, since while all solid-state 3D batteries have been proposed⁴⁵, extensive processing difficulties remain^{46,47}, mostly due to the limitations of sputtered ceramic electrolytes^{37,48}.

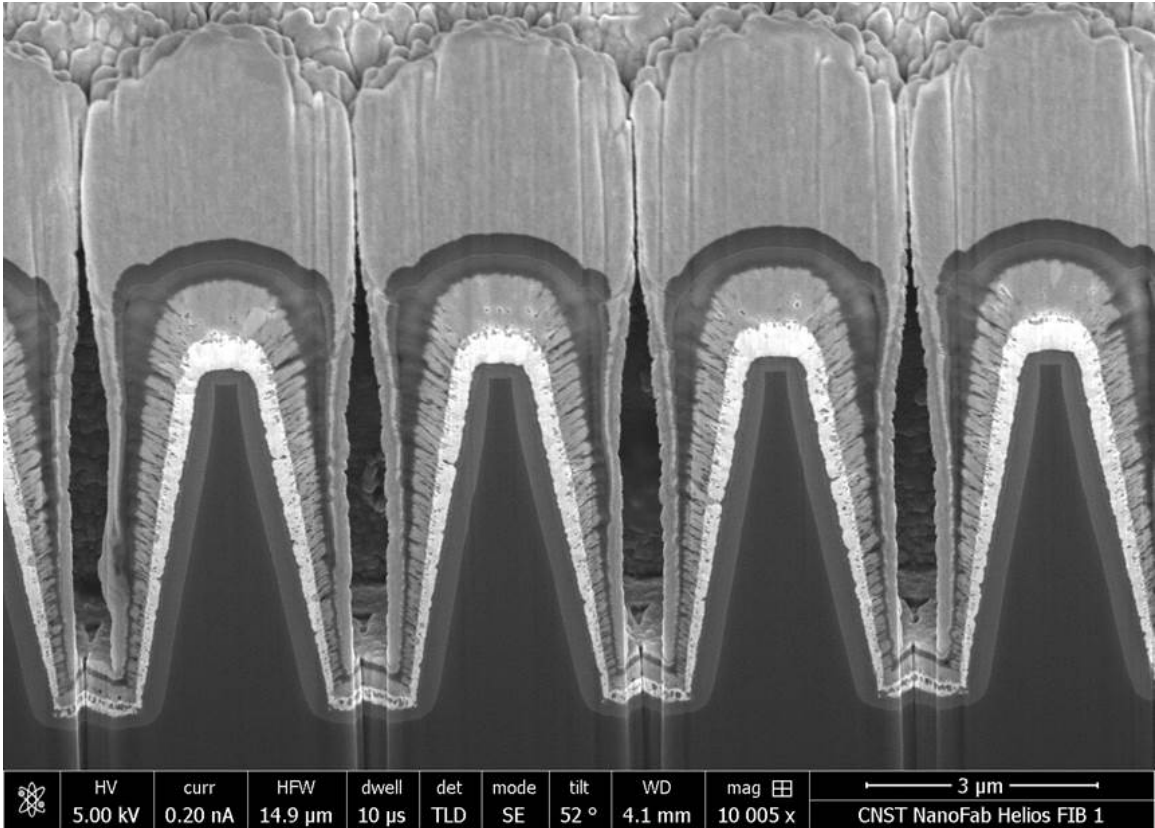


Figure 4. FIB X-section of solid 3D battery fabricated using sputtering techniques for all active material layers. Note the major non-uniformities inherent from the line of sight sputtering technique result in poor interfacial and film quality. Image courtesy of A. Alec. Talin.

Sputtering is a line of sight deposition technique that has been well utilized to fabricate planar solid batteries with great success^{46,48-50}, however it is limited to aspect ratios of ~ 10 , limiting the increases in power and energy density available due to nanostructuring⁵¹. Also, sputtered solid electrolyte films do not perform well at thickness < 70 nm due to inhomogeneities and voids at the interface between the electrode and the sputtered solid electrolyte³⁷.

Atomic Layer Deposition (ALD)

ALD is one of the most promising ways to deposit electrochemically active materials onto high aspect ratio templates. ALD's high degree of conformality and unprecedented thickness control enable the deposition of electrochemically active films as thin as 5 nm on templates with aspect ratios of up to 1000⁴³. ALD of electrochemically active films has so far been limited to only a few materials: V₂O₅⁵², Ru⁵³ and RuO₂⁵⁴, and TiO₂⁴¹, however there has also been significant work on using thin ALD films as protective coatings on both anode⁵⁵⁻⁵⁸ and cathode⁵⁹⁻⁶¹ materials, as well as using ALD for the deposition of TiN current collectors in nanoheterostructured EES devices^{13,62}. More recently, a nanopore battery array was developed using ALD materials for conformal current collectors as well as both anode and cathode materials¹⁵. This device can retain 50% of the active material's theoretical capacity when operated at 150C discharge rate (75 full charge/discharge cycles per hour), illustrating the remarkable performance possible with nanoheterostructured batteries.

Lithium Phosphorus Oxynitride (LiPON)

One of the first and most popular solid electrolytes developed is lithium phosphorous oxynitride (LiPON). The ionic conductivity of LiPON can be as high as $\sim 5 \times 10^{-6}$ S/cm, and LiPON is stable against Li metal anodes, potentially enabling the use of Li metal anodes in all-solid devices. Due to the body of literature available on the characterization and behavior of LiPON^{50,63-73}, this material was selected as the best candidate for ALD solid electrolyte development.

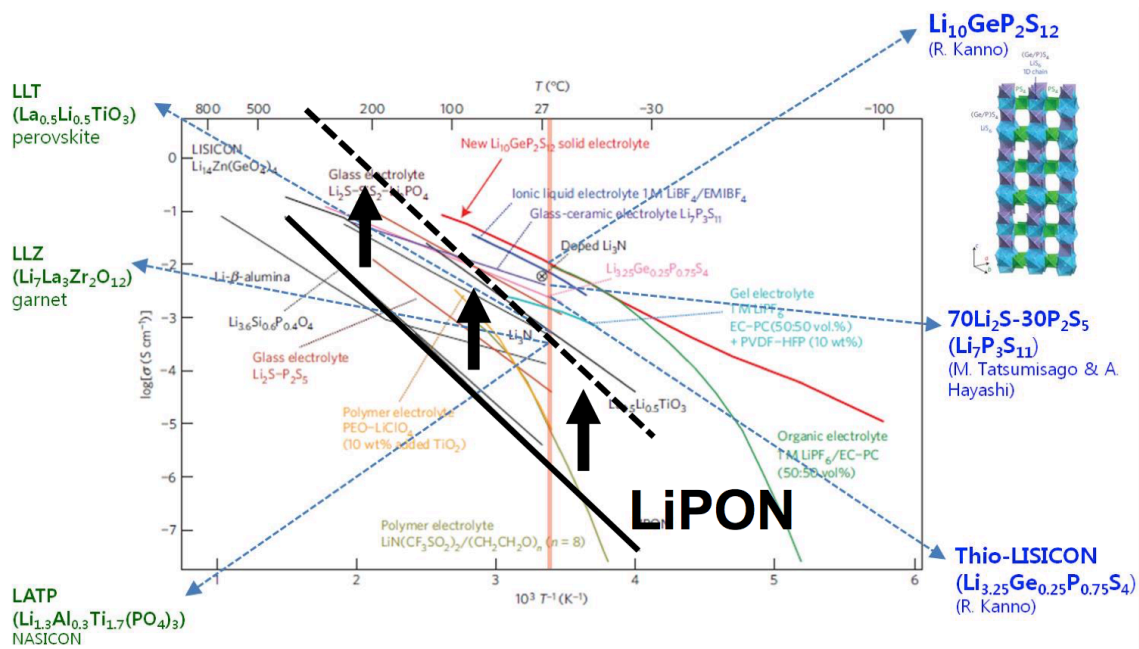


Figure 5. Summary of ionic conductivities for well-known Li^+ solid electrolytes, adapted from Tarascon.¹² The arrows to the dotted line indicate the effective conductivity enhancement possible by using a thin solid electrolyte on high aspect ratio nanostructures for enhanced device surface area.

As such, this thesis focuses on the methodology and progress toward development of an ALD process for the solid-state electrolyte LiPON. Nitrogen will be included in the ALD Li_3PO_4 films using either NH_3 gas or an NH_3 or N_2 remote plasma source. The influence of film growth and processing parameters will be investigated to understand the process parameters that define conductivity, morphology, and stability. Lastly, development of an ALD process for the solid electrolyte LiPON will facilitate future development of all-ALD solid-state batteries on highly aspect ratio nanostructured scaffolds.

Next Generation Metal Anodes for Beyond Li-ion Batteries

The ever increasing demand for higher energy density storage devices for transportation (electric vehicles), grid storage (power leveling), and other applications is challenging the scientific community to develop a rechargeable battery with cycle life comparable to Li-ion but with significantly higher capacity. Major R&D centers increasingly look to metal anode systems, including Li-S, Li-O₂, and advanced oxide cathode systems combined with Li metal anodes for increased performance. Recent analysis of beyond-Li-ion options by the Joint Center for Energy Storage Research (JCESR) highlights the high priority for metal anode systems, while recognizing that the reactivity of the metal anode poses serious technical and manufacturing challenges.⁸

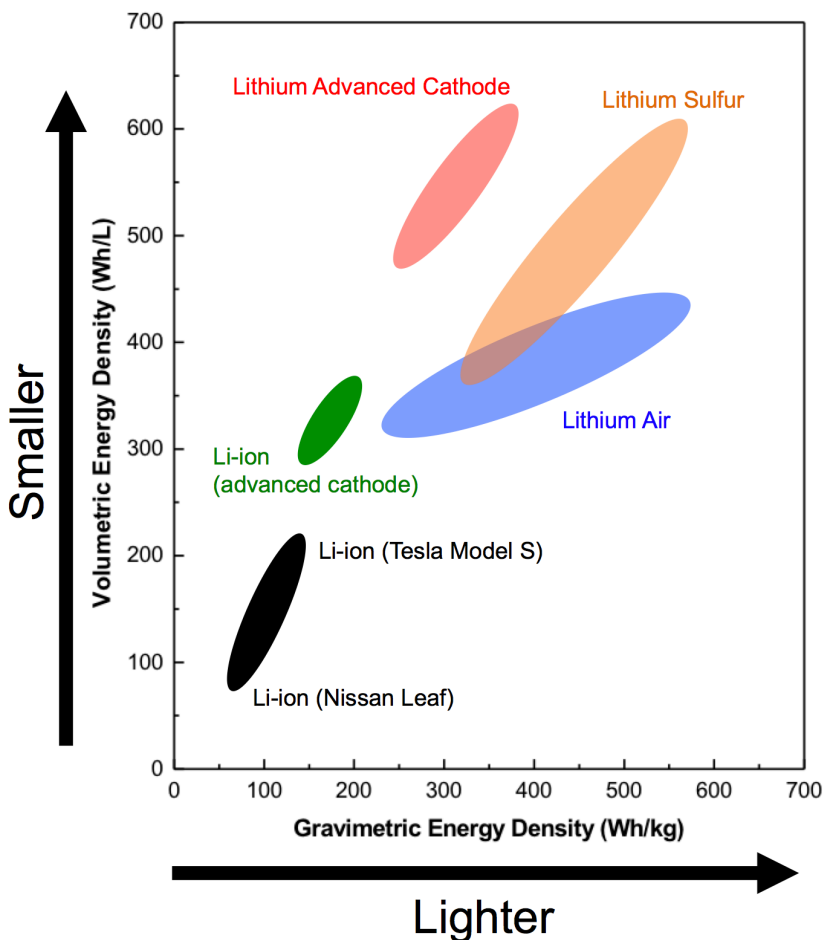


Figure 6. Potential beyond Li-ion battery chemistries. Note that the three most promising options: Lithium advanced cathode, Lithium sulfur, and Lithium air all utilize Li metal anodes. Adapted from Gallagher et.al.⁸

electrolyte, eventually leading to degradation of the anode, consumption of electrolyte and active materials, and eventual battery failure.

In fact, the battery industry expended considerable effort to commercialize Li metal anodes *via* electrolyte additive engineering in the late 1980s.⁷⁴⁻⁷⁶ However due to the propensity of lithium metal to form dangerous dendrites upon repeated cycling, resulting in a number of high profile fires in 1989, the use of lithium anodes decreased in popularity.⁷⁵

From an operational point of view, lithium's high reactivity with most organic chemicals used in battery electrolytes causes corrosion reactions to occur during cycling due to reduction of solvents, active species, or impurities in the

Realization of stable Li metal anodes in rechargeable batteries is a challenge with many facets. From a processing perspective, lithium metal will oxidize and corrode under atmospheric conditions *via* reaction with H₂O and CO₂ *via* the stepwise reactions



producing a characteristic black tarnish on the Li metal surface.⁷⁷ This oxidation is prevented by limiting the exposure of the Li metal to H₂O, necessitating the use of costly dry rooms for lithium metal extrusion and battery assembly.

Lithium metal protection is particularly important in systems where the active material diffuses freely through the electrolyte (e.g. polysulfide in Li-S cells), or if inherent contamination is present in the electrolyte (e.g. H₂O, CO₂, and N₂ in a real Li-air system). In both of these cases the highly reactive Li anode forms a high impedance solid electrolyte interphase (SEI) layer on its surface consuming electrolyte and active material resulting in practical capacity loss and low of Coulombic efficiency.⁷⁸

Previous attempts to passivate Li metal with organic molecules^{79,80} and polymeric coatings^{81,82} have achieved limited success due to poor thickness and compositional control of the applied protection layer. Protection with sputtered solid electrolytes,^{64,83} while effective at preventing electrolyte decomposition on the Li metal surface, can result in large cell overpotentials during recharge at even moderate rates due to the large thicknesses (~μms) and low ionic conductivity of the sputtered solid electrolytes. Recently, protection of the Li surface with self-assembled carbon spheres⁸⁴ has proven effective at preventing Li dendrite growth upon cycling, but offers limited options for

scalable manufacturing and also adds significant mass to the anode. Lithium metal powder is commercially available from the FMC company, and shows promise towards stable lithium anodes.^{79,85}

I demonstrate a new approach to study Li metal surface stabilization *via* application of ALD protection layers directly on the Li metal, creating a new thin phase between the metal and various corrosive surroundings. Using a unique UHV system described elsewhere,⁸⁶ I deposit ALD Al₂O₃ coatings directly on Li metal foil to mitigate corrosion reactions due to both atmosphere and electrolyte exposure. I determine and measure directly, for the first time, the nominal layer thickness for effective Li metal protection, and use Li-S cells to demonstrate a dramatic capacity increase of protected Li metal anodes over their unprotected counterparts *via* mitigation of the Li corrosion by sulfur species shuttling in the electrolyte.⁸⁷ While the focus of this work is on Li metal anodes, these studies open a new opportunity for realization of other metal anode based systems such as Na, Mg, and Al rechargeable batteries, and for protection of those metal by various thin layers deposited atomically or molecularly.

ALD Solid Electrolyte Process Development Strategy

There are two ways to consider quaternary ALD process development. First, quaternary process development can be seen as the combination of multiple constituent ALD processes in different ratios. For example, in our case this would be a combination of the Li₃PO₄, Li₂O, and LiN ALD processes. Each of these individual materials is composed of two precursors (e.g. A+B, C+D, and E+F), and combining these constituent

materials in different ratios of ALD supercycles can result in a degree of tunability in the resulting nanolaminate film.

However, this approach presents a few problems. First, if two of the constituent ALD materials use the same precursor, then this creates a precursor pulse redundancy during the process. Second, due to the surface termination of the films, some precursors may only be compatible with specific surface species, preventing the incorporation of elements into the resulting films due to differences in ligand exchange reaction energies. Lastly, in order to control film stoichiometry different ratios of the constituent ALD precursors must be used, which can result in nanolaminates with an uneven distribution of constituent elements.

Instead, I take a novel additive synthesis approach to quaternary ALD process development, starting with the thermal ALD process for Li_2O and LiOH ,⁸⁸ a full description of which is discussed in Chapter III: ALD Li_2O Process Development. From this binary ALD process, I add an additional precursor, TMP, and determine the saturation dose of the ternary Li_3PO_4 ALD process, discussed in detail in Chapter IV: ALD Li_3PO_4 . I next add an additional ALD precursor, plasma N_2 , and subsequently optimize the ALD process for the quaternary material LiPON, discussed in detail in Chapter V: ALD LiPON.

Chapter II: Laboratory Design, Equipment, and Experimental Methods

Ultraclean, Ultrahigh Vacuum System

To pursue the objectives of this Thesis, a custom UHV system (integrated system) was designed and constructed in order to be able to deposit, transfer, and characterize Li-containing ALD materials without air exposure, facilitating novel materials discovery and chemical analysis. This integrated ultraclean deposition and characterization system is based upon a previous system used to investigate the utility of ALD Al_2O_3 dielectric films for fabrication of Josephson junction superconducting qubit devices. This initial study was published in *Applied Physics Letters* in 2013,⁸⁶ and illustrates the utility of ultraclean integrated synthesis and characterization.

In particular, this system offers a unique experimental configuration that links ultraclean (i.e., high vacuum) ALD process capability (*Cambridge Nanotech Fiji F200*) with *in-operando* spectroscopic ellipsometry (*J.A. Woollam M-2000D*) and *in-situ* x-ray photoelectron spectroscopy (XPS) (*Kratos AXIS Ultra DLD*) characterization for materials analysis.

The *Kratos* AXIS Ultra DLD surface analysis platform is outfitted for x-ray and ultraviolet photoelectron spectroscopy (XPS/UPS) including x-ray imaging and mapping capabilities using a monochromated Ag/Al XPS source, scanning Auger microscopy (SAM), and scanning electron microscopy (SEM). Additional components that are extremely useful include an Ar^+ /Coronene/ He^+ ion cannon for sputter depth profiling and

ion scattering spectroscopy (ISS), and a charge neutralization system for charge balancing insulating materials. All of the XPS measurements discussed in this work were collected with this system.

The integrated system was designed around a central *Kurt J. Lesker* RTTA radial UHV transfer chamber, which is isolated via 8" diameter pneumatic gate valves to 4 other vacuum chambers: one aluminum evaporator/load lock chamber, one load lock/sample holding chamber, one *Ultratech* Fiji F200 ALD tool (Mario), and one *Kratos* Ultra DLD surface analysis system. Both load lock chambers and the RTTA chamber on the integrated system have their own dedicated maglev turbo pump (*Oerlikon-Leybold*, 80 L/s), each of which is both backed and roughed by a dedicated mechanical pump (*Oerlikon-Leybold*, 14 cfm). These pumps hold the base pressure of the system at $< 1 \times 10^{-8}$ Torr. The ALD chamber is maintained at 1×10^{-6} Torr, while the XPS is maintained at 2×10^{-9} Torr. The UHV section of the integrated system is connected to an *MBraun* Labmaster Ar glovebox for battery assembly and testing, which is also integrated to a second *Ultratech* Fiji F200 ALD system (Luigi). The glovebox is customized with multiple 8" conflat port attachments for direct integration with other vacuum systems attachments. One of these CF ports connects to the UHV system, while a second one is attached to another vacuum chamber with an effusion cell for thermal evaporation of lithium metal, providing a cleaner, thin film alternative to the lithium ribbon used in most battery experiments.

Sample transfers between the ALD system and the surface analysis system are fast (1 minute), minimizing potential contamination from chamber outgassing, even at UHV pressure regimes. A schematic of this system is shown in Figure 7.

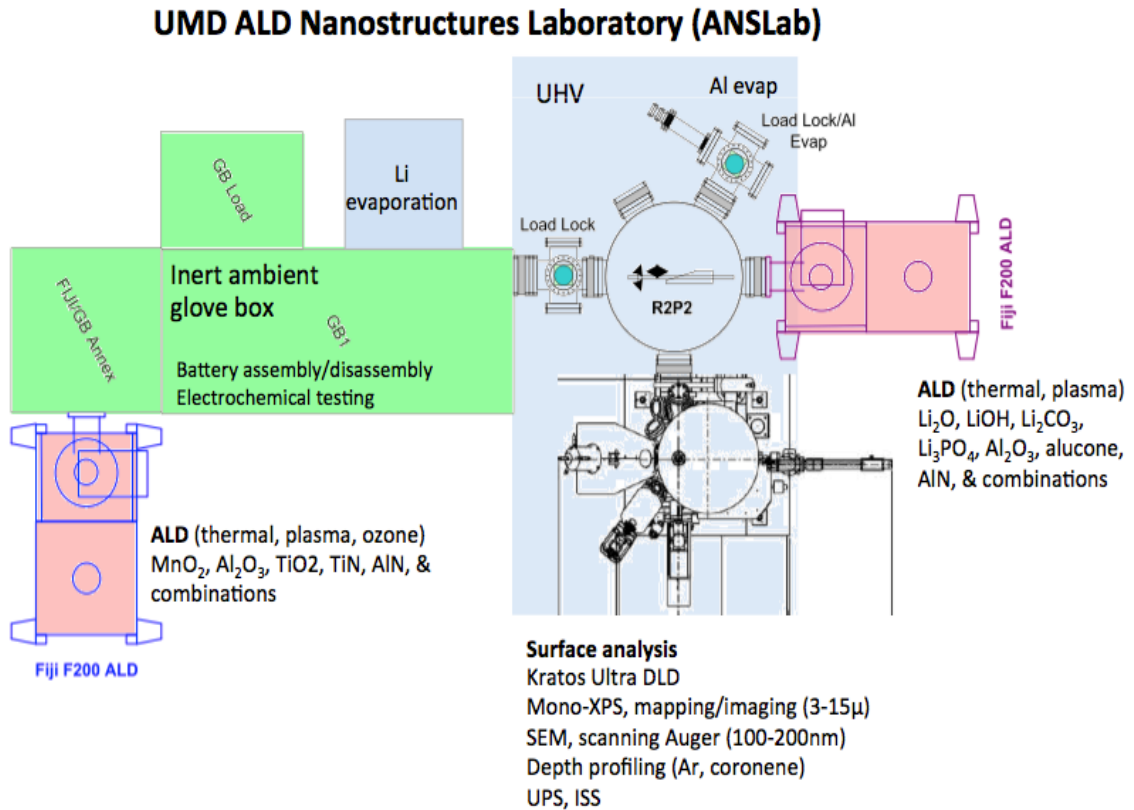


Figure 7. Schematic and setup of the UHV integrated system in the ALD Nanostructures Lab (ANSLab) at the University of Maryland, College Park.

Substrate Preparation

3" diameter silicon wafers were used for ALD process development for a few reasons. First, the entire integrated system is tooled for 3" wafers to simplify sample handling and transfer. Second, given the difficulty of developing optical models to enable accurate ellipsometric monitoring of deposition processes, selection of a well-characterized substrate is necessary to simplify the process. Lastly, since ALD processes

are known to be substrate dependent due to the surface energy and availability of reactive hydroxyl ligands, so Si wafers allow materials deposition on a clean, smooth, and consistent substrate.

Silicon substrates were cleaned with stepwise acetone, methanol, and isopropanol rinses, blown dry with compressed air, and then rinsed with deionized H₂O and blown dry again. Once clean, the substrates were pumped down in the load lock chamber until a base pressure of $< 5 \times 10^{-8}$ Torr was achieved, and then transferred to the ALD system for materials deposition.

Atomic Layer Deposition (ALD)

ALD is a low temperature sequential pulse-purge thin film growth technique known for high quality films with angstrom tunable thickness. ALD uses conventional CVD metalorganic and oxidation precursors, however instead of introducing both precursors into the reactor at the same time, ALD alternates pulsing and purging of each precursor sequentially. Therefore, instead of a vapor phase chemical reaction, the reaction is limited to chemisorbed species on the surface. This results in incredible conformality, but does suffer from much slower deposition rates than CVD. The ALD tool most used in this thesis is a *Ultratech* Fiji F-200 system, custom-designed for UHV operation and integration into a UHV radial transfer chamber.

ALD Additive Synthesis

There are two ways to consider quaternary ALD process development. First, quaternary process development can be seen as the combination of multiple constituent

ALD processes in different ratios. For example, in our case this would be a combination of the Li_3PO_4 , Li_2O , and LiN ALD processes. Each of these individual materials is composed of two precursors (A+B, C+D, and E+F respectively). Combining these constituent materials in different ratios of ALD supercycles can achieve limited tunability of the resulting films. For example, the following pulse sequence would be achieved:



This approach presents a few problems. First, if two of the constituent ALD materials used in the quaternary process use the same precursor, then there is a precursor pulse redundancy during the process, slowing deposition time and potentially wasting expensive ALD precursor chemicals. Second, due to the surface chemistry of the films, some precursors may only react with specific surface ligands, preventing the incorporation of some precursors into the resulting films or resulting in non-ideal growth. Last, in order to control film stoichiometry different ratios of the constituent ALD precursors must be used, which can result in highly nonuniform, lamellar films where the desired dopants are not evenly distributed among the final film.

Instead, a different approach to quaternary ALD process development will be taken, starting with the thermal ALD process for Li_2O ⁸⁸ using H_2O and LiO^tBu . Once this process is fully characterized, a second precursor, trimethylphosphate (TMP) will be added to the process. Once deposition conditions for the ternary ALD material are optimized, nitrogen will be incorporated into this ternary ALD process to determine the optimal deposition parameters for high ionic conductivity and stability. I will use NH_3 gas, NH_3 plasma, and N_2 plasma doses at various points during the ALD process. The

amount of N incorporated into the LiPON films will either be tuned by varying the N precursor pulse time, if favorable, or by using multiple doses of the N precursor at multiple points in the ALD process.

X-ray Photoelectron Spectroscopy (XPS)

XPS analysis provides information on chemical composition and atomic binding environment at the film surface. All XPS spectra collected during the course of this thesis were collected using a *Kratos* Ultra DLD surface analysis system. Due to the low escape depth of ejected photoelectrons, generally XPS is only able to sample < 10 nm from the material surface. XPS is one of the few methods available that is sensitive to Li due to the low electron cross section and generally low signals from Li from most other measurement techniques.

During XPS data collection, no charge neutralization was used, as due to the high reactivity of lithium compounds even at low currents (1 nA) the electron flux from the charge neutralizer was found to degrade the ALD films, consistent with previous reports⁸⁹. XPS data was analyzed using *CasaXPS* using a Shirley background algorithm, and quantification was performed using peak areas normalized by standard photoionization cross sections corrected for our instrument geometry⁹⁰.

Spectroscopic Ellipsometry

This thesis relies heavily on the use of both *in-operando* and *ex-situ* spectroscopic ellipsometry in order to measure thickness from both in-situ ALD thin film deposition and post-deposition ex-situ ALD films. Both arrangements use the same *J.A. Woollam*

M-2000D spectroscopic ($\lambda = 193\text{-}1000\text{ nm}$) ellipsometer, whose source and detector can easily be moved from the ex-situ goniometer to fixed angle (72°) fixtures attached to the *Cambridge Nanotech* Fiji F200 ALD tool for *in-situ* data collection. Spectroscopic ellipsometry uses both the phase shift and polarization shift of elliptically polarized light reflected off thin, transparent films in order to measure the refractive index as a function of wavelength using the Cauchy and Sellmeier relationships⁹¹. To determine thin-film thicknesses, optical models must be employed to convert the phase shift of the light (Δ) to the film thickness. Optical models for the ALD materials described in this thesis were developed in concert with the *J.A. Woollam* company, and thickness measured using these models are externally calibrated using profilometry and TEM/SEM imaging measurements on MWCNT and SiNW substrates.

Chapter III: ALD Li₂O Process Development

Introduction

Lithium compounds play multiple critical roles in electrochemical energy storage. Typically Li is incorporated into either anode or cathode structures in a battery during manufacture, so the development and understanding of ALD processes for Li-containing electrode compounds is essential to next-generation materials design. Li₂O represents an attractive starting point for ALD of Li compounds - a superionic conductor in its own right⁹² and a model process for incorporating Li into multicomponent ALD materials for electrodes and electrolytes.

Previously, ALD films deposited using lithium *tert*-butoxide (LiO^tBu) and H₂O have been reported⁹³, but the chemistry of the deposited films has not been conclusively identified due to the extreme air sensitivity of lithium oxides and hydroxides and the lack of *in-situ* characterization. In the course of this thesis, ALD films of ultrapure LiOH and Li₂O have been deposited and characterized via XPS for the first time, resulting in the only known carbon-free (< .1%) XPS spectra of these materials in the literature. These results have been published in the Journal of Physical Chemistry C⁸⁸, and are summarized in this chapter.

Thermal ALD Using H₂O

First, saturation doses for the ALD Li₂O process were determined by fixing the H₂O pulse time and varying the LiO^tBu pulse time at fixed purge times, shown in Figure 8.

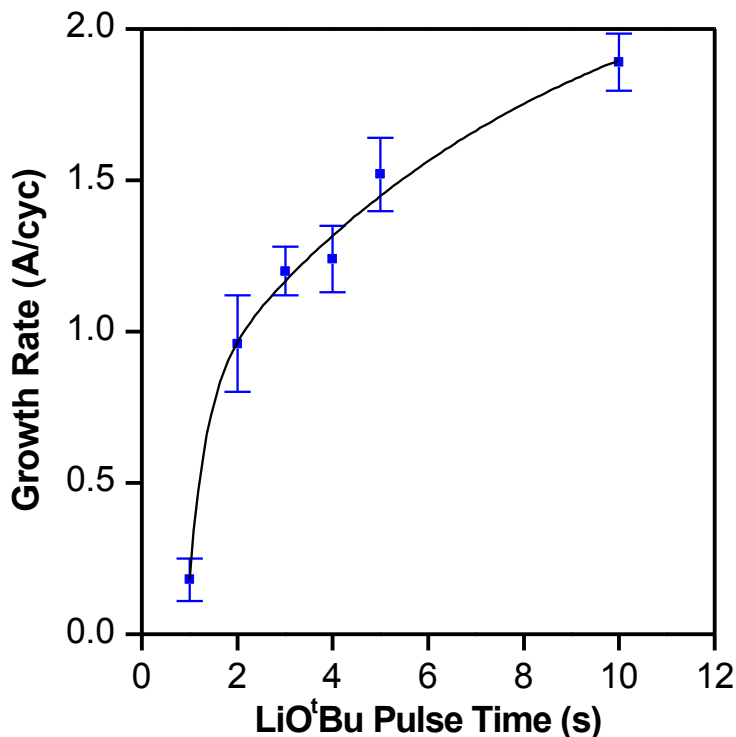


Figure 8. Growth curve demonstrating self-saturating behavior for ALD Li_2O as a function of LiOtBu pulse time at 250°C . H_2O pulse time was fixed at 0.06 s, and purge times for both precursors were 30 seconds. The data points are fit to an arbitrary function.

of the LiOtBu precursor on the substrate, leading to CVD-like growth. As such, the LiOtBu pulse time is fixed at 3s for this work to enable a reasonable growth rate of the ALD materials.

Thermal ALD using the precursors LiOtBu and H_2O is favorable within the temperature window from 225°C to 300°C as shown by the thermal ALD results in Figure 9(survey, 250°C) and Figure 10A-C (hi-resolution spectra, multiple temperatures). [Note that Figure 10A-C also include $^{16}\text{O}_2$ spectra, with features relevant to carbonate, discussed below in terms of energy axis calibration and plasma-based ALD process.]

Unlike many other ALD processes, the $\text{LiOtBu} + \text{H}_2\text{O}$ system does not exhibit saturating growth as a function of LiOtBu precursor dose, consistent with previous studies in literature using these precursors⁹⁴. This non-saturating growth is attributed to possible decomposition

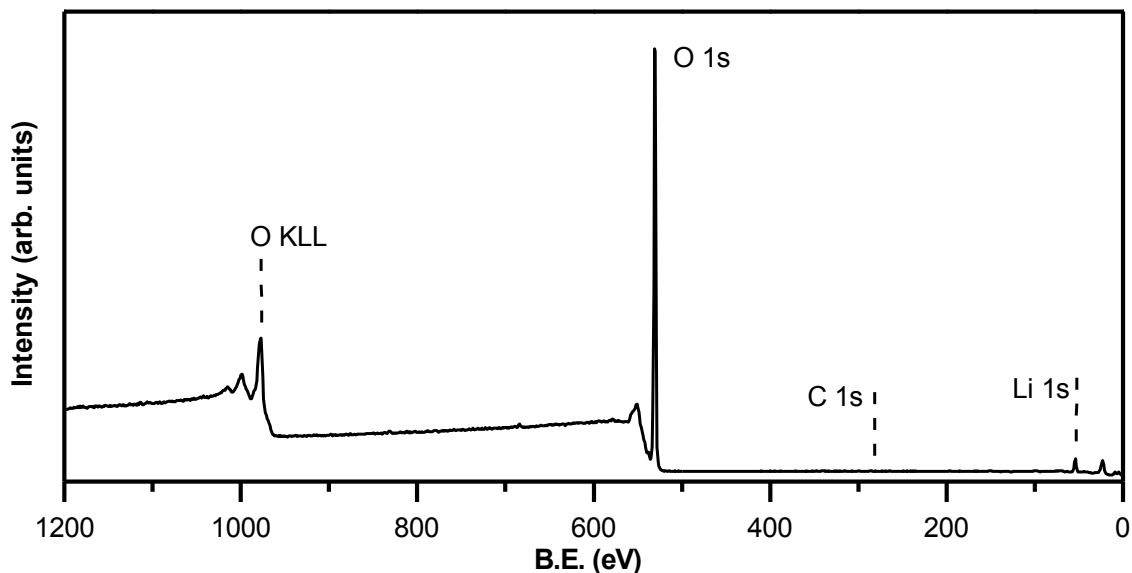


Figure 9. In-situ XPS survey spectra of as-deposited ALD Li_2O at 250°C demonstrating ultraclean carbon-free nature of the as-deposited films. Carbon content is $< .1\%$ as determined by the signal to noise ratio of the data.

XPS reveals that films deposited at 225°C are composed almost entirely of LiOH , while films deposited at 240°C , 265°C and 300°C are composed of Li_2O with a hydroxylated surface layer.

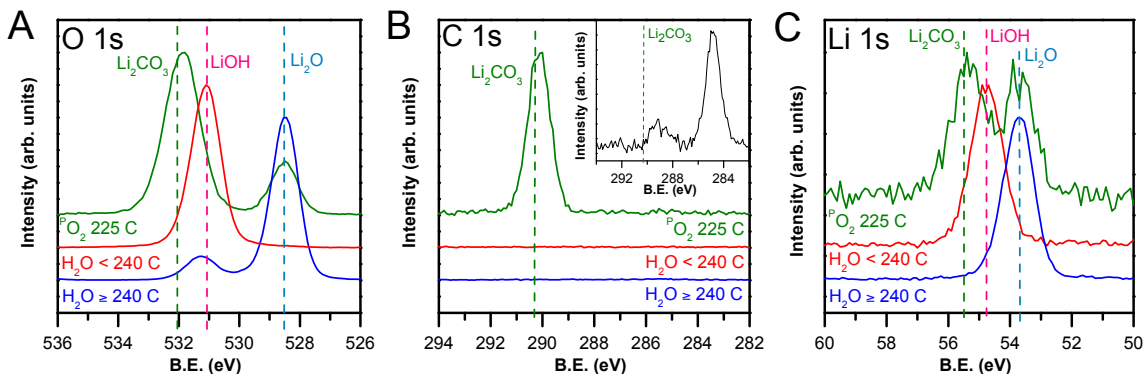


Figure 10. High resolution in-situ (a) $\text{O}1s$; (b) $\text{C}1s$; and (c) $\text{Li}1s$ XPS spectra of as-deposited ALD films using LiO^iBu , H_2O , and plasma O_2 with deposition ending on the oxidation precursor half cycle. Inset in (b): XPS $\text{C}1s$ spectra of Li_2O deposited at 250°C ending on the LiO^iBu half cycle. All spectra have been normalized to the same arbitrary intensity to highlight peak locations and peak shapes.

While it has been suggested in prior work that the carbon in ALD deposited films is due to incomplete reaction of the butyl ligands from the LiO^tBu precursor⁹⁴, The thermal ALD processing ending with the LiO^tBu dose do show carbon (Figure 10B inset) only limited to submonolayer coverage, but distinctly different from Li_2CO_3 spectra, while the process ending in an H_2O dose shows no carbon signal due to the complete ligand exchange reaction of the LiO^tBu .

Due to the simple nature of the measured spectra, the film chemistry can be conclusively identified via atomic quantification. Low temperature deposition (225°C) results in a close to 1:1 Li:O ratio consistent with LiOH , while deposition at all attempted higher temperatures shows a 2:1 Li:O ratio consistent with Li_2O . We always find a slight oxygen excess inconsistent with theoretical stoichiometry, probably due to both hydroxyl termination of the Li_2O surface⁹⁵ and also sub-surface photoelectron screening by surface oxygen. While a 1:1 Li:O ratio would also be consistent with Li_2O_2 , we consider this unlikely due to the reactivity of Li_2O_2 with H_2O ⁹⁶.

Conventionally, XPS peak positions are calibrated to the adventitious C 1s peak at 284.8 eV as a reference. However given the absence of carbon in these XPS spectra, the spectra are calibrated by assigning the Li_2O O1s peak to 528.5 eV based on a consensus of reported literature values⁹⁷. Given this calibration, the LiOH O 1s photoelectron peak is placed at 531.1 eV, with a $\text{LiOH-Li}_2\text{O}$ O 1s peak separation of 2.6 eV. Notably, after energy calibration of all spectra to this O1s peak, upon air exposure and reexamination of the LiOH films both the C1s peaks attributed to Li_2CO_3 at 290.3 eV (observed only for the $^p\text{O}_2$ process and discussed later) and adventitious carbon at 285.0 eV (discussed later)

are at their nominally correct locations. It is worth noting that both the Li_2O and LiOH O 1s photoelectron peaks are present to some degree in each sample, likely due to the surface hydroxylation of the Li_2O films during transfer and characterization in UHV. In the Li 1s spectra (Figure 10C), there is a peak associated with Li_2O at 53.8 eV in the high temperature films, while a different peak associated with LiOH is located at 54.7 eV in the low temperature films, generally consistent with previous studies⁹⁷.

The chemical mechanisms controlling half-cycle reactions for this ALD process are not well understood. Lithium tert-butoxide is an alkoxide precursor, but it differs considerably from other common alkoxide precursors such as hafnium or zirconium tert-butoxide in that lithium is monovalent. In the multivalent *tert*-butoxides, a self-limiting surface reaction is realized through the hydrolysis of one of the tert-butoxide ligands, preserving the remaining ligands as inert site-blockers. In the case of LiO^tBu , hydrolysis of the single ligand would produce lithium hydroxide and tert-butanol, putting the existence of a stable, self-limiting surface species in question. Indeed, previous studies by Cavanaugh et al. relate non-saturating growth rates as a function of LiO^tBu pulse time to a mechanism involving the chemisorption of the intact LiO^tBu molecule on the surface⁹³. Identification of the surface species present after the LiO^tBu pulse was attempted using in-situ XPS (Figure 10B, inset). There are two hydrocarbon peaks, one at ~285 eV and a small peak centered at ~289 eV. The peak at 289 eV is possibly consistent with carboxylate species, however a chemical origin is not identified at this time. This spectrum is likely incompatible with the presence of intact tert-butoxide ligands, from which a peak associated with the C-O bond in a 1:4 areal ratio with and at approx. 2 eV

above the hydrocarbon peak would be expected. Further work will be needed to identify the exact nature of the half-cycle surface chemistry. Nevertheless, the film chemistry of the $\text{LiO}^t\text{Bu}/^p\text{O}_2$ process strongly supports the existence of significant amounts of carbon-containing surface species.

Plasma ALD Using O_2

Deposition using LiO^tBu and $^p\text{O}_2$ as the oxidation precursor was attempted between 225°C and 300°C . While this has been previously used to deposit Li_2O as one component of the multicomponent ALD material LiCoO_2 ⁹⁸, here it is found that use of $^p\text{O}_2$ as the oxidation precursor results in films that are composed of both Li_2CO_3 and Li_2O , the ratios of which are independent of deposition temperature and plasma dose. The presence of significant amounts of Li_2CO_3 for the $^p\text{O}_2$ process demonstrates that stable carbon-containing surface species are formed by the plasma ALD process during the LiO^tBu half-cycle. High resolution XPS spectra of the as-deposited films, shown in Figure 10A-C, identify the resulting films as a mixture of Li_2CO_3 and Li_2O . The formation of Li_2CO_3 when $^p\text{O}_2$ is used as the oxidation precursor is attributed to an incomplete combustion reaction that causes significant residual carbon to be trapped in the films, resulting in the formation of Li_2CO_3 . Consistent with the previous analysis, the O1s Li_2O binding energy is calibrated to 528.5 eV. However, in this case the O1s Li_2CO_3 peak is shifted to a slightly lower binding energy at 531.9 eV, a peak separation of 3.4 eV from the Li_2O O1s peak. The peak at 290.1 eV is assigned to the C1s of Li_2CO_3 , while the Li 1s spectra shows two peaks at 53.8 and 55.3 eV, consistent with Li_2O and Li_2CO_3 respectively.

Elucidating Hydration/Dehydration Reactions

Consistent with previous work by Comstock⁹⁹, ALD films deposited at 225°C and subjected to extended purging at the same temperature result in a ~ 20% decrease in film thickness. This mass loss is attributed to thermal decomposition of LiOH and H₂O product evolution, as the reaction product LiOH formed below 240°C exhibits the decomposition when held post-process at elevated (225°C) temperature. ALD films deposited at higher temperatures do not exhibit post-deposition thickness relaxation, as the LiOH decomposition time is less than the purge time, allowing the films to continuously relax during the ALD process.

XPS results shown in Figure 11A-C demonstrate this thermal decomposition of LiOH via the following reaction⁹⁶:



The as-deposited film is dehydrated here due to deposition at 250°C.

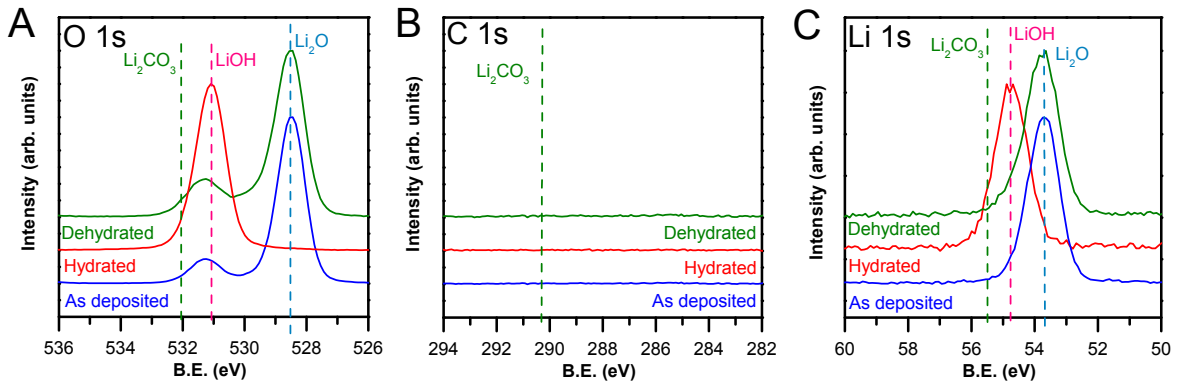


Figure 11. Hi resolution in-situ (a) O1s; (b) C1s; and (c) Li1s XPS spectra of as-deposited, fully hydrated, and subsequent 24-hour dehydrated Li₂O ALD films using LiO^tBu and H₂O at 250°C with deposition ending on the oxidation precursor half cycle. All XPS data are from the same wafer.

Subsequent treatment of the Li₂O film with sequential ALD half-cycle H₂O pulses reverses the reaction (Equation 1), forming LiOH. This reaction is highly reversible, and

could conceivably be driven back and forth forever, given the favorable formation of LiOH from Li₂O in an H₂O atmosphere and the thermal decomposition temperature of LiOH.¹⁰⁰

To understand the reaction kinetics of this hydration/dehydration reaction, the same ALD Li₂O film was fully hydrated by exposure to water vapor at 250 mTorr in our ALD chamber at temperatures from 225°C to 275°C. Once the film was fully hydrated to LiOH as determined by real-time spectroscopic ellipsometry and XPS, real-time spectroscopic ellipsometry was again used to track the dehydration rates of the ALD films at different temperatures as plotted in Figure 12A.

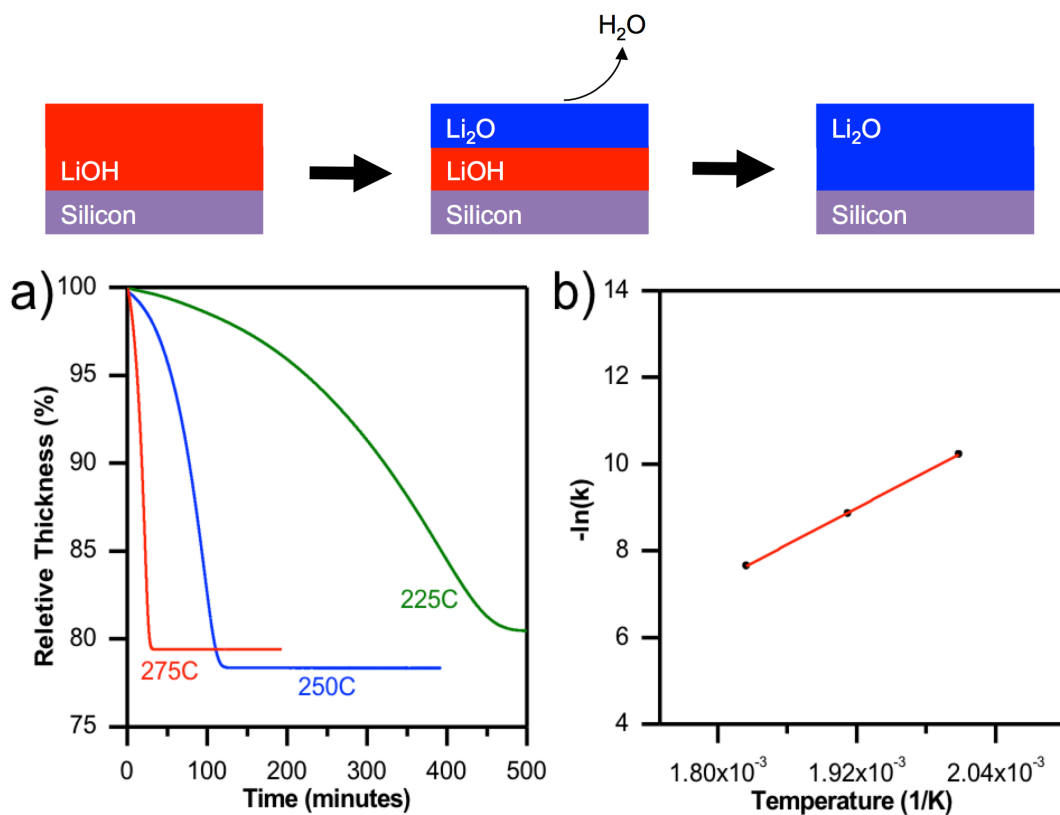


Figure 12. (a) Real time in-situ ellipsometric measurement of the dehydration of LiOH to Li₂O as a function of temperature under vacuum at different temperatures; (b) Arrhenius plot of the LiOH to Li₂O dehydration reaction along with linear fit.

These data can be used to plot an Arrhenius relationship (Figure 12B) and then extract an activation energy of 112.7 ± 0.6 kJ/mol for the reaction in Equation 1, consistent with results from previous studies¹⁰¹. This technique is useful to quantify and track changes in both film thickness and optical properties during a chemical reaction, but requires no prior knowledge of the sample chemistry, thickness, or even the reaction mechanism. As long as the optical properties and thickness change during the reaction, the onset and completion of the chemical reaction can be identified with relative precision. In this case, a 5-layer graded optical model combining B spline models for both Li₂O and LiOH was used to model the dehydration of the ALD films as occurring from the top down.

The activation energy of 112.7 kJ/mol was then applied to develop an “ALD phase diagram” of the LiO^tBu + H₂O process as a function of process purge time and reactor temperature for the chosen precursor pulse times, shown in Figure 13. As long as the purge time during the ALD process is longer than the time required for the deposited monolayer to decompose from LiOH to Li₂O, the film will continuously relax during the deposition process, resulting in Li₂O at temperatures below 240°C. Given this knowledge, the resulting ALD films can be tailored at a given temperature to be LiOH or Li₂O simply by changing the purge times while keeping static precursor pulse times. Notably, this is the first example where a “hybrid” ALD + relaxation process has been deconvoluted and characterized. For the purposes of this thesis, selection of the Li₂O phase is critical, given that H in the deposited films competes with Li for active sites in LiPON and may drastically decrease the conductivity of the eventual ALD LiPON.

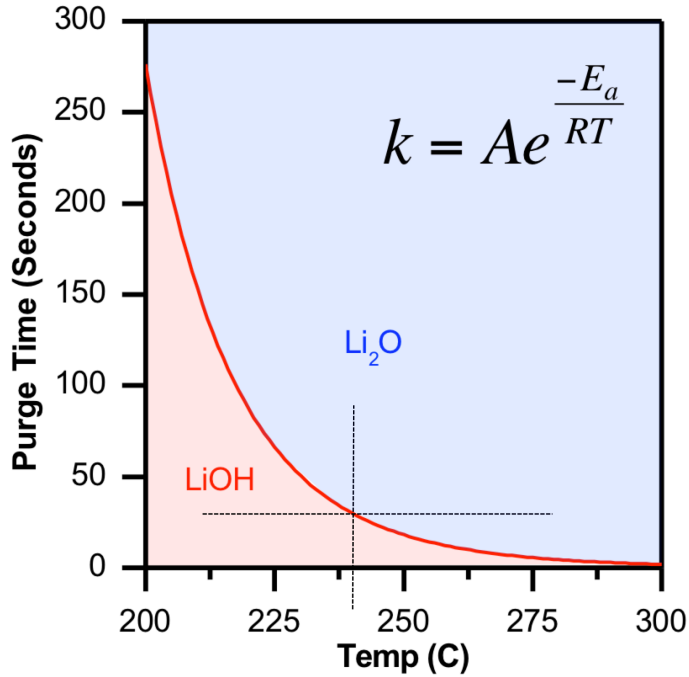


Figure 13. Phase diagram of the LiO'Bu + H₂O ALD process at fixed (.06s, 30s, 3s, 30s pulse and purge times for the H₂O and LiO'Bu precursors respectively). Phase boundary is calculated based on experimental fit to the Arrhenius equation using experimental data. This phase diagram allows selection of LiOH or Li₂O depending on temperature and purge time of the ALD process.

Deconstructing the Air-Reactivity of Li₂O

The extreme air reactivity of lithium containing thin films is well known, and is challenging for materials characterization. Indeed, upon exposure of the as-deposited Li₂O films to atmosphere for 60 seconds and then subsequent reintroduction to the integrated system, XPS

shows that the surface LiOH formed has completely reacted with atmospheric CO₂, irreversibly forming a surface layer of Li₂CO₃, shown in Figure 14.

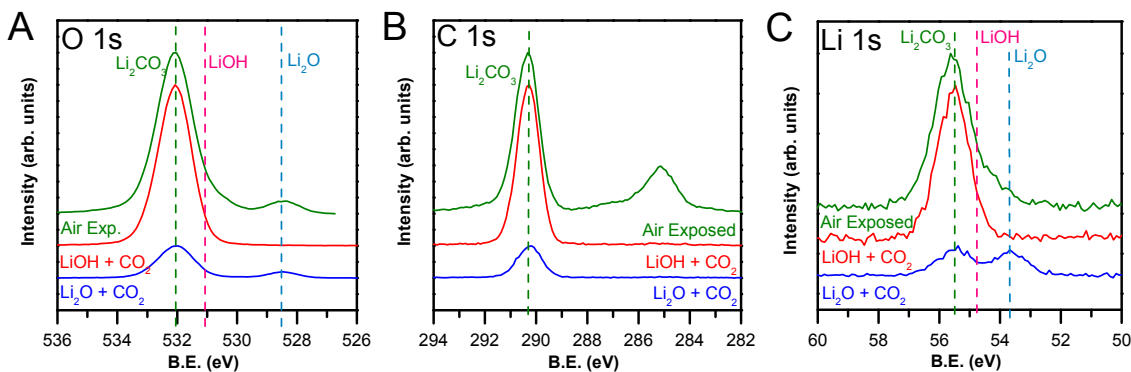


Figure 14. High resolution in-situ (a) O1s; (b) C1s; and (c) Li1s XPS spectra of ALD LiOH and Li₂O ALD films after saturating exposures to CO₂ at 225°C, as well as air-exposed ALD Li₂O.

The reaction of Li₂O with CO₂ is known to occur with the top few nm of Li₂O between 200°C and 400°C via the following reaction¹⁰²:



Since air exposure forms LiOH from Li₂O, Li₂CO₃ is expected to be formed by the LiOH-CO₂ reaction even at ambient conditions according to:



continuing until the entire bulk LiOH is converted to Li₂CO₃. This well-known reaction is used in the military and space industry to remove waste CO₂ from the atmosphere of contained environments like submarines and spacecraft.

To further investigate this reaction, ALD films of LiOH at 225°C and Li₂O at 250°C were deposited for 1500 cycles. Then, samples were removed from the ALD chamber into a high vacuum holding chamber, while the ALD chamber cooled to 225°C. The samples were returned to the ALD chamber at 225°C and dosed with CO₂ via a repeating 1 second pulse / 5 second Ar purge cycle. Real time *in-situ* ellipsometric data collected during these reactions is shown in Figure 15, where the phase shift of the incident light (Δ) is plotted against CO₂ dosing process time.

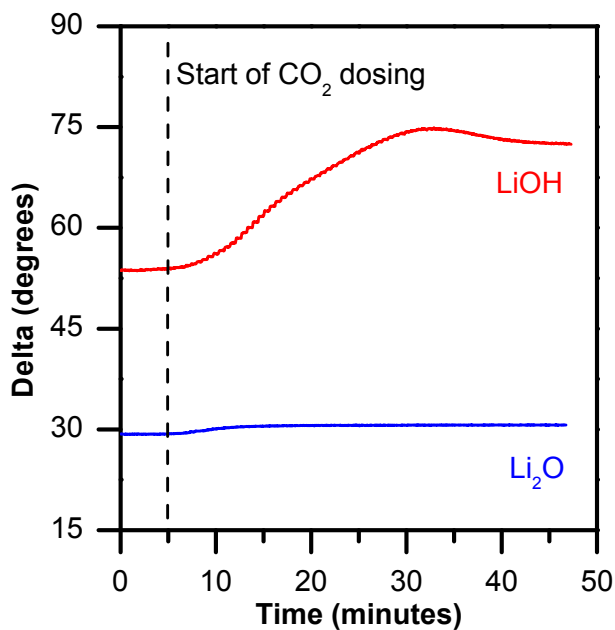


Figure 15. Real time in-situ ellipsometric measurement of the reaction between an ALD film of LiOH + CO₂ and an ALD film of Li₂O + CO₂ at 225C and $\lambda=598$ nm.

Since the CO₂ is pulsed, the amount of reactant available is limited, allowing gas-phase titration the carbonation reaction Equation 3 to measure the relative amounts of LiOH in the ALD films. XPS spectra of both LiOH + CO₂ and Li₂O + CO₂ films are shown in Figure 14, along with air-exposed Li₂O for reference. The spectra

demonstrate that the LiOH surface is fully reacted to Li₂CO₃, while the Li₂O surface still shows some unreacted Li₂O (~14%), suggesting that reaction 3 is considerably faster than reaction 2. Because of the surface sensitivity of XPS, it can be concluded that the Li₂O-CO₂ reaction is limited to the surface region.

This high reactivity of LiOH with CO₂ explains why previous XPS studies of Li₂O and LiOH have exhibited significant surface carbonate contamination upon air exposure, and illustrates the importance of ultraclean synthesis and characterization on Li containing ALD process development. The differential reactivity of CO₂ provides an intriguing path to discriminate the surface composition and chemistry of Li₂O films versus thicker LiOH films.

High Aspect Ratio Deposition

The developed ALD process for Li_2O was used to coat a multiwalled carbon nanotube (MWCNT) sponge to not only calibrate thicknesses of deposited films using TEM, but also to characterize the conformality of the ALD Li_2O process. Samples produced were transferred under inert packaging to the TEM, where they were loaded with < 5 minutes air exposure. Figure 16 shows ALD Li_2O on a MWCNT, demonstrating both the amorphous nature of the as-deposited ALD films, and the highly conformal deposition of these films on a MWCNT substrate with aspect ratio ~ 66 . This conformal deposition is necessary to enable the future fabrication of templated nanostructures for advanced batteries.

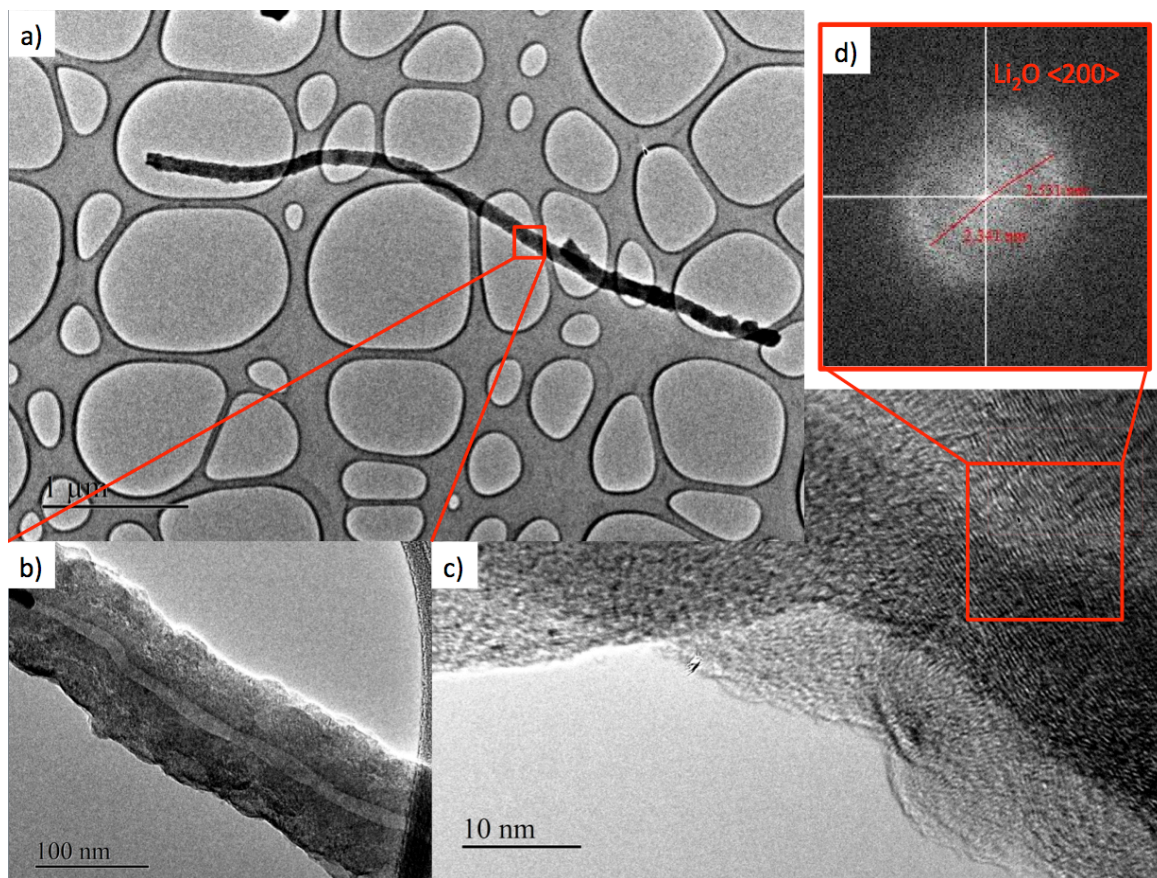


Figure 16. (a, b, c) TEM images of ALD Li_2O deposited using LiO^iBu and H_2O at 250°C on to a MWCNT substrate demonstrating ability to conformally coat high aspect ratio nanostructures; (d) electron diffraction image of one Li_2O crystal showing the $\langle 200 \rangle$ plane.

Chapter Summary

The first ultraclean synthesis and characterization of Li_2O , LiOH , and Li_2CO_3 thin films using LiO^tBu , H_2O , and $^p\text{O}_2$ as precursors has been demonstrated. At 225°C , the thermal ALD process results in thin films of LiOH , while above 225°C the ALD process results in films of Li_2O with a hydroxylated surface layer. Use of plasma excitation ($^p\text{O}_2$) complicates the deposition product and introduces carbon, leading to a combination of Li_2CO_3 and Li_2O , the ratios of which do not vary with temperature. Further, these experiments demonstrate the extreme air reactivity of ALD Li_2O films due to reversible surface hydroxylation by H_2O followed by irreversible carbonate formation at room temperature. Given this and the differential reactivity of Li_2O vs. LiOH to CO_2 , control of process ambient and intentional gas dosing provide new avenues for understanding the relevant surface and bulk chemistries of Li oxide materials, underscoring the value of ultraclean synthesis and in-situ characterization.

Chapter IV: ALD Li_3PO_4

Introduction

Others have combined the LiO^tBu and H_2O chemistry in ternary ALD processes for metal oxide cathodes⁹⁸, anodes¹⁰³, and solid electrolytes^{99,104,105}, however again a fundamental understanding of the film growth processes and surface chemistry during deposition is incomplete due to both the high reactivity of the Li-containing ALD materials and the difficulty of developing multicomponent ALD processes. Previously, Lithium phosphate ALD films have been demonstrated using the binary process of LiO^tBu + trimethylphosphate (TMP)¹⁰⁵, however the published ALD process did not include H_2O as a precursor, simplifying deposition chemistry.

Process Development

Starting with the ALD Li_2O chemistry at 250°C , the TMP is added at two different points in the ALD process: after the H_2O pulse and before the H_2O pulse, resulting in two different precursor orders: $\text{LiO}^t\text{Bu}\rightarrow\text{H}_2\text{O}\rightarrow\text{TMP}$, and $\text{LiO}^t\text{Bu}\rightarrow\text{TMP}\rightarrow\text{H}_2\text{O}$. Precursor saturation doses for the $\text{LiO}^t\text{Bu}\rightarrow\text{H}_2\text{O}\rightarrow\text{TMP}$ pulse order are shown in Figure 17 as determined by *in-situ* spectroscopic ellipsometry. There is no functional difference between both precursor pulse orders as determined by the chemistry and morphology of the resulting films, suggesting that considerable atomic and molecular reorganization is occurring during the ALD growth process. The saturation dose for TMP is .4s when inserted into to the ALD Li_2O chemistry, with a saturating growth rate of $1.2 \text{ \AA}/\text{cycle}$. ALD Li_3PO_4 films have been deposited between 150°C and 300°C , however the growth

rate remains constant over the examined temperature range, indicating a large and robust growth process window.

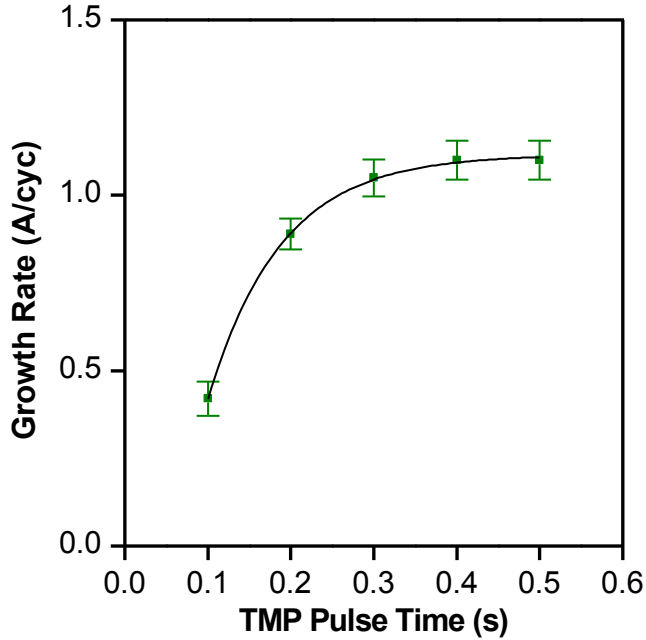


Figure 17. Growth curve demonstrating self-saturating behavior for ALD Li_3PO_4 as a function of TMP pulse time at 250°C for the deposition sequence $\text{Li}^{\text{O}^{\text{t}}\text{Bu}}\text{H}_2\text{O}\text{TMP}$. $\text{Li}^{\text{O}^{\text{t}}\text{Bu}}$ and H_2O pulse times were 3 s and 0.06 s respectively, and purge times for all precursors were 30 seconds. The data points are fit to an arbitrary exponential function.

ALD Li_3PO_4 Characterization

In-situ XPS determines that ALD films deposited using the ternary $\text{Li}^{\text{O}^{\text{t}}\text{Bu}}\text{H}_2\text{O}\text{TMP}$ process sequence (as well as those deposited using the alternate process sequence) result in a film chemistry and stoichiometry of Li_3PO_4 , shown in Figure 18. These films do show residual carbon contamination ($\sim 1.5\%$), most

likely due to the incomplete exchange of the methyl ligands from the TMP precursor during the ALD process. Without the addition of the water pulse the TMP will not fully react with the $\text{Li}^{\text{O}^{\text{t}}\text{Bu}}$ -terminated surface, resulting in significantly higher ($\sim 10\%$) carbon contamination in the resulting films. Addition of the water precursor after the $\text{Li}^{\text{O}^{\text{t}}\text{Bu}}$ pulse ensures a fully hydroxylated surface during the TMP pulse, nearly eliminating carbon from the ALD films via complete ligand exchange during the TMP pulse and increasing the saturating growth rate to $\sim 1.1 \text{ \AA/cycle}$.

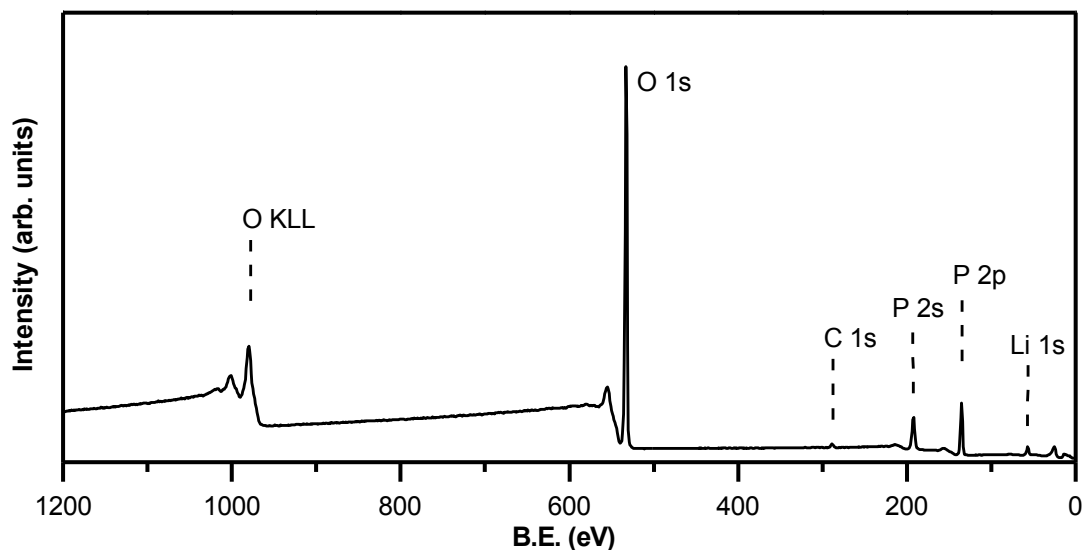


Figure 18. In-situ XPS survey spectra of as-deposited ALD Li_3PO_4 at 250°C . Some residual carbon ($\sim 1.5\%$ at.) is present due to the incomplete reaction of the trimethylphosphate ligands with the LiO^tBu .

External Characterization

The now-developed ALD process for Li_3PO_4 was used again to coat a MWCNT sponge for both external thickness calibration and to characterize the conformality of the ALD Li_3PO_4 process. Samples produced were transferred under inert packaging to the TEM, where they were loaded with < 5 minutes air exposure. Figure 19A shows ALD Li_3PO_4 on a MWCNT. Here, as opposed to the ALD Li_2O process, the as-deposited films are polycrystalline, in agreement with previous results¹⁰⁵. XRD data confirming the ALD film crystallinity are shown in Figure 19B. The labeled XRD peaks are consistent with multiple Li_3PO_4 patterns from the ICDD database.

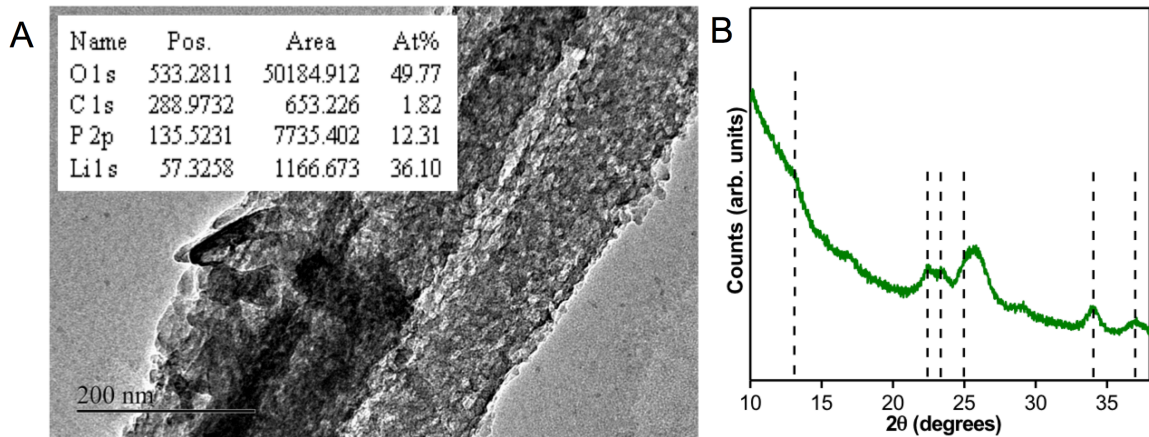


Figure 19. (a) TEM image of ALD Li_3PO_4 deposited on a MWCNT sponge substrate showing the polycrystalline nature of the as-deposited film. Inset is the atomic composition of the heterostructure as determined by *in-situ* XPS; (b) XRD pattern of the ALD Li_3PO_4 as-deposited on the MWCNT substrate. XRD peaks are consistent with Li_3PO_4 from the ICDD database.

Chapter Summary

An ALD process for Li_3PO_4 has been developed and characterized. The ALD process window is between 150°C and 300°C with a stable growth rate of $\sim 1.1 \text{ \AA}/\text{cycle}$ as determined by *in-operando* spectroscopic ellipsometry. ALD Li_3PO_4 is deposited in crystalline form, and the ionic conductivity is determined to be $8 \times 10^{-9} \text{ s/cm}$, comparable with values in literature^{105,106}.

Chapter V: ALD LiPON

Background

Since its discovery in the early 1990s,¹⁰⁷ LiPON (lithium phosphorous oxynitride) has been one of the most popular solid-state electrolytes used for planar lithium ion microbatteries. LiPON thin films are commonly deposited using reactive sputtering of a Li_3PO_4 target in an N_2 atmosphere.^{64,66,68,108,109} Generally, sputtered LiPON films are $\sim 1\mu\text{m}$ thick, but sputtering of much thinner LiPON films (12 nm) has recently been demonstrated.¹¹⁰ As a physical deposition technique, sputtering is generally unable to deposit high quality films on 3D geometries.³⁷ Also, the low reactivity of the N_2 gas during the sputtering process also has difficulty doping these films with $> 2\%$ N.

Highly tunable N doping of LiPON is possible through e-beam evaporation of Li_3PO_4 coupled with a N_2 plasma discharge above the substrate,¹¹¹ however this technique is also limited to planar substrates.

More recently, Kim et al. developed a MOCVD process for LiPON,¹¹² but high deposition temperatures (500 C) are undesirable for co-processing with many battery materials and chip packaging components, and preclude deposition on materials such as Li_2CoO_3 cathodes without degradation during the deposition process or on metallic Li metal anodes without melting them.

ALD has emerged as the premier deposition process for fabrication of uniform thin, conformal films on high aspect ratio scaffolds.^{40-42,113} ALD has been used to fabricate $\text{Li}_x\text{A}_2\text{IO}_3$ ^{99,104,105}, $\text{Li}_x\text{Si}_y\text{Al}_2\text{O}_3$,¹¹⁴ and LiLaTiO_2 .¹¹⁵

Stepwise Process Optimization

During this phase of the ALD process development nitrogen is incorporated into Li_3PO_4 thin films via inclusion of NH_3 gas, NH_3 plasma, or N_2 plasma precursors during the ALD process. During the process sequence, there are 12 possible places to include N in the ALD process sequence:

- 1: $\text{LiO}^t\text{Bu} - \text{H}_2\text{O} - \text{TMP} - \text{N}$
- 2: $\text{LiO}^t\text{Bu} - \text{H}_2\text{O} - \text{N} - \text{TMP}$
- 3: $\text{LiO}^t\text{Bu} - \text{N} - \text{H}_2\text{O} - \text{TMP}$
- 4: $\text{LiO}^t\text{Bu} - \text{N} - \text{TMP} - \text{H}_2\text{O}$
- 5: $\text{LiO}^t\text{Bu} - \text{TMP} - \text{H}_2\text{O} - \text{N}$
- 6: $\text{LiO}^t\text{Bu} - \text{TMP} - \text{N} - \text{H}_2\text{O}$
- 7: $\text{H}_2\text{O} - \text{LiO}^t\text{Bu} - \text{TMP} - \text{N}$
- 8: $\text{H}_2\text{O} - \text{LiO}^t\text{Bu} - \text{N} - \text{TMP}$
- 9: $\text{H}_2\text{O} - \text{N} - \text{LiO}^t\text{Bu} - \text{TMP}$
- 10: $\text{H}_2\text{O} - \text{N} - \text{TMP} - \text{LiO}^t\text{Bu}$
- 11: $\text{H}_2\text{O} - \text{TMP} - \text{LiO}^t\text{Bu} - \text{N}$
- 12: $\text{H}_2\text{O} - \text{TMP} - \text{N} - \text{LiO}^t\text{Bu}$

As before, real-time, *in-operando* spectroscopic ellipsometry is utilized to develop variable-dose ALD recipes during process development, eliminating the need to deposit all 12 precursor permutations in separate ALD runs on separate substrates. This methodology drastically increases process development and optimization time, while allowing real-time process metrology. ALD recipes with 100 cycles of each set of parameters (1-6) were developed, with the process stopped after each permutation for XPS characterization and analysis. After analysis, the same wafer was transferred from the XPS back into the deposition chamber for the next deposition sequence, allowing process development without film contamination due to air exposure and eliminating waiting periods during substrate pump down times. Process sequences 6-12 were not

run, as these are identical to sequences 1-6 through translational symmetry. After the first two precursor pulses, the rest of the sequence is identical.

Thickness calibration of the optical model for ALD LiPON is an iterative process, requiring thickness confirmation using both an external profilometer and TEM imaging, followed by re-analysis of previously collected ellipsometric data. The optical model used for ALD LiPON is a B-Spline model developed in conjunction with the J.A. Woollam company, and verified for accuracy within 10% thickness. This optical model is shown in Figure 20.

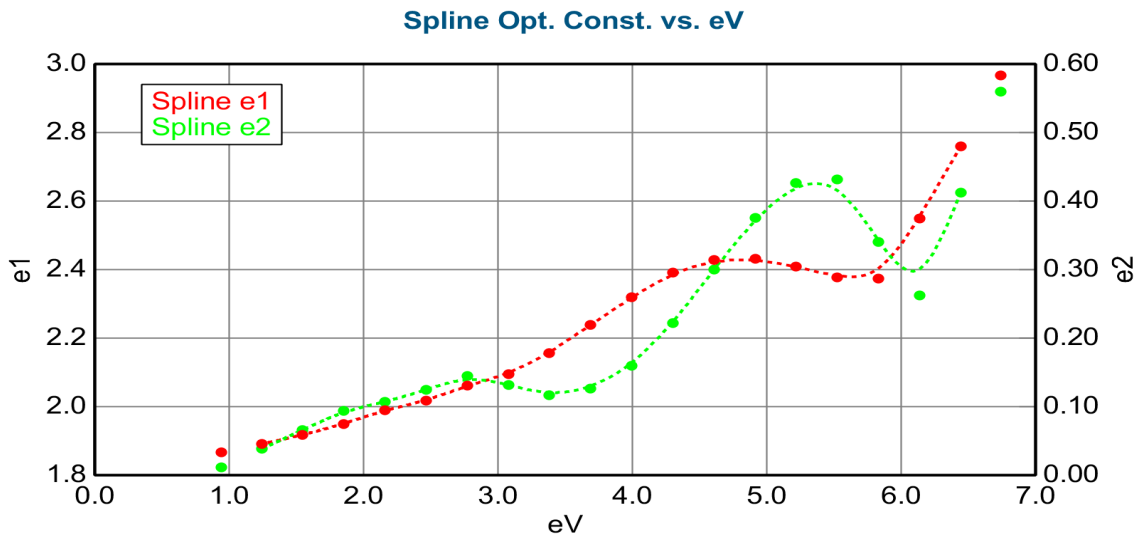


Figure 20. B-Spline optical model used for ALD LiPON developed in conjunction with the J.A. Woollam company.

The most promising N precursor for ALD LiPON is NH_3 gas in order to avoid plasma enhanced ALD process, which are known to have limited conformality as compared to the thermal ALD processes due to the short mean-free path of the plasma radicals, however use of NH_3 gas at any point in the ALD process results only in deposition of

Li_3PO_4 films. As these depositions were unsuccessful at fabrication of ALD LiPON , this data is not shown in this thesis.

Next, doping of ALD Li_3PO_4 films using plasma N_2 pulses during the ALD process was attempted at each possible step of the process sequence, which while offering lowered conformality over thermal ALD processes, can in certain cases facilitate deposition of challenging chemistries due to the high reactivity of the plasma species.

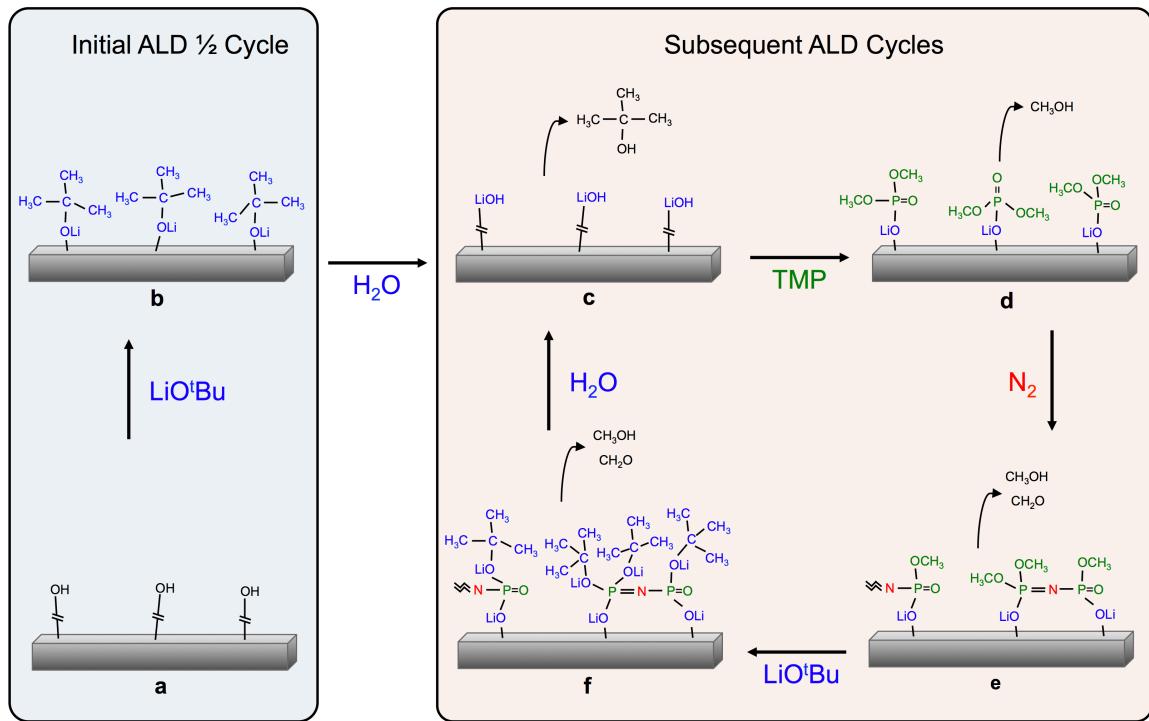


Figure 21. Cartoon of the proposed ALD LiPON process chemistry. (a) Hydroxyl terminated substrate; (b) metastable surface after the LiO^tBu pulse; (c) H_2O pulse removes the tert-butanol ligands and forms LiOH on the surface; (d) TMP reacts with surface LiOH through ligand exchange reaction, evolving CH_3OH ; (e) N_2 plasma crosslinks phosphorous atoms and evolves CH_3OH ; (f) LiO^tBu reacts with $-\text{OCH}_3$ ligands and evolves both CH_2OH and CH_2O . The initial LiO^tBu and H_2O pulses shown in (a) and (b) are required “activate” the substrate prior to deposition. For all subsequent ALD cycles, the process chemistry in (c) through (f) is repeated as one ALD cycle.

Indeed, use of $^{15}\text{N}_2$ during the ALD process can successfully dope N into Li_3PO_4 , however this only works with one specific precursor pulse sequence, as most of the surface terminating ligands are non-reactive towards $^{15}\text{N}_2$. We managed to incorporate

Nitrogen into the ALD films only when the $^{15}\text{N}_2$ was applied after the TMP pulse, directly before the LiO^tBu pulse.

The full quaternary ALD LiPON process sequence is shown in Figure 21, which elucidates the impact of ligand chemistry on the ALD process sequence. Application of the $^{15}\text{N}_2$ dose in any other location during the process sequence resulted in deposition of nitrogen-free polycrystalline Li_3PO_4 , likely due to the nature of the nitrogen bonding in LiPON.¹¹⁶ In doped phosphate glasses, nitrogen atoms serve as either doubly or triply coordinated bridges among phosphorous atoms. In the ALD process, incoming N ions presumably act to “crosslink” otherwise disparate TMP fragments on the surface, which we believe aids in the amorphization of the film. If the phosphorous atoms are not the surface species (such as after any other precursor pulse aside from TMP) then the stable bonding sites for N are unavailable due to steric hindrance from ligands on the other precursors, preventing incorporation of N into the ALD films.^{68,70}

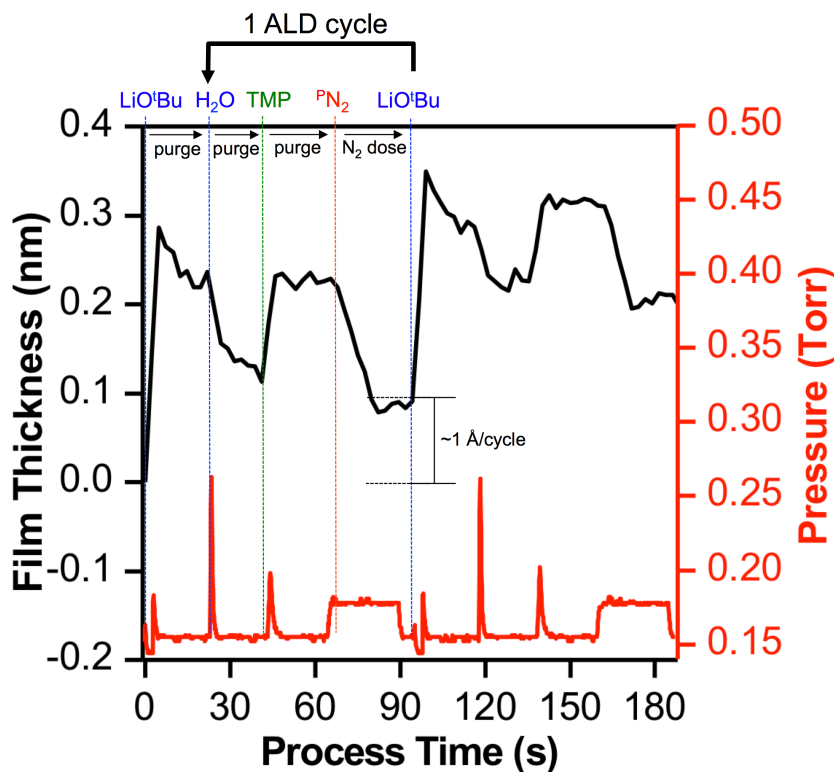


Figure 22. (left axis, black) Spectroscopic ellipsometry data for the fully optimized ALD LiPON process demonstrating the growth and shrinkage due to precursor chemisorption and ligand exchange reactions during the individual steps of the ALD cycle. (right axis, red) Pressure trace in the ALD reactor showing corresponding precursor pulses during ALD growth.

Figure 22 shows a pressure trace overlaid with an in-situ ellipsometric thickness measurement for one complete ALD cycle of the optimized process. The changes in film thickness are generally in line with the mechanism

proposed in Figure 21. The addition of LiO^tBu species to the surface leads to a thickness gain of approximately 0.3 nm, which is reduced somewhat during the purge period due to a combination of vaporization and decomposition. The measured thickness sharply decreases upon the addition of H₂O, which is consistent with a ligand exchange reaction liberating *tert*-butanol and leaving behind the smaller LiOH unit (Figure 21, b to c). The addition of TMP again increases the thickness of the film consistent with a stable, surface bound methyl phosphate species. Finally, the application of a remote N₂ plasma coincides with a linear decrease of film thickness, which is consistent with the crosslinking reaction

proposed in Figure 21 steps d to e. We note that while the N_2 plasma is a remote process, some high energy ions and neutrals may be reaching the film and etching the surface, although the overall growth rate is clearly positive in all cases.

Chemical Characterization

Figure 23 shows an XPS survey spectra of ALD LiPON, while Figure 24 shows high-resolution XPS spectra of the ALD LiPON films demonstrating the impact of the PN_2 dose on the binding environment of the ALD films.

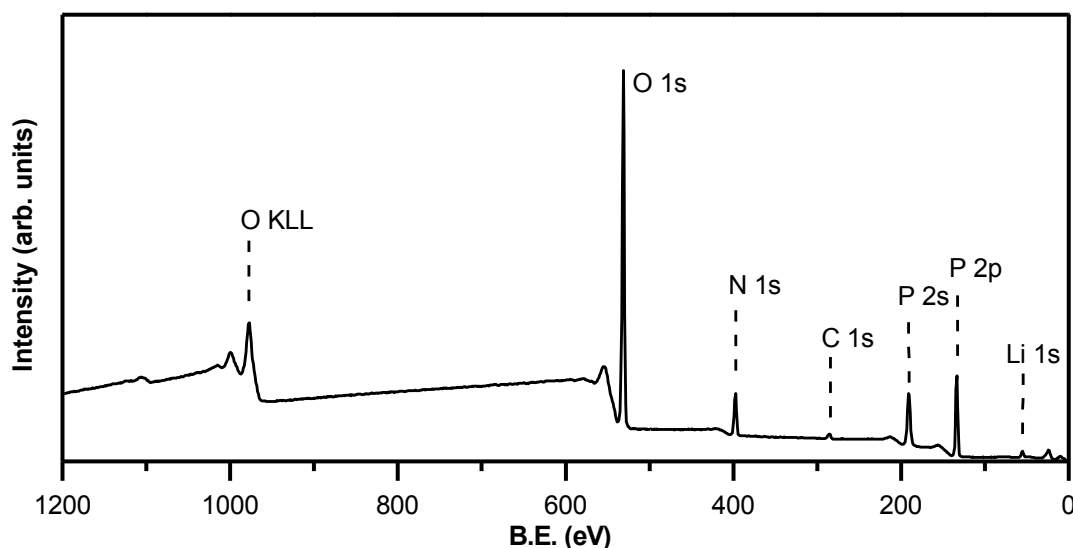


Figure 23. In-situ survey XPS spectra of as-deposited ALD LiPON at 250°C demonstrating ALD film purity.

Due to the lack of carbon in these films, all spectra are calibrated against the Li 1s peak, set at 55.6 eV in line with previously measured values for Li_3PO_4 .¹¹⁷ The Li 1s orbital generally shows the least variation of binding energy with chemical environment among the elements present, warranting its choice for use in calibration. With no PN_2 dose the O1s (531.6 eV), and P2p 3/2 (133.6 eV) XPS peaks are also consistent with

Li_3PO_4 . As the $^{15}\text{N}_2$ dose is increased, the chemistry of the film changes markedly. The overall incorporation of N grows with dose time. The N spectrum demonstrates two chemical species, which are generally associated with atoms linking either two or three P atoms in the glass.⁷⁰ There is a slight shift of the phosphate O1s peak to lower binding energies by ~ 0.1 eV, along with the emergence of a second O1s peak at 533.0 eV, attributed to an increase in bridging oxygen (P-O-P) in the LiPON glass. Interestingly, the parallel increase of both the bridging oxygen and nitrogen content stands in contrast with previous reports on the chemistry of sputtered LiPON films,¹¹⁸ in which more N results in less bridging oxygen. This is likely due to the fact that sputtered LiPON is usually amorphous regardless of N content, and so contains a maximum number of bridging oxygens when no nitrogen is present to substitute for them. In the case of ALD LiPON, the film is also undergoing a transition from crystalline to amorphous with increasing N content, and so the overall number of all bridging species is increasing. Both P2p peaks are slightly broadened with increasing N content, also consistent with LiPON amorphization with higher $^{15}\text{N}_2$ dose, as will be demonstrated below.

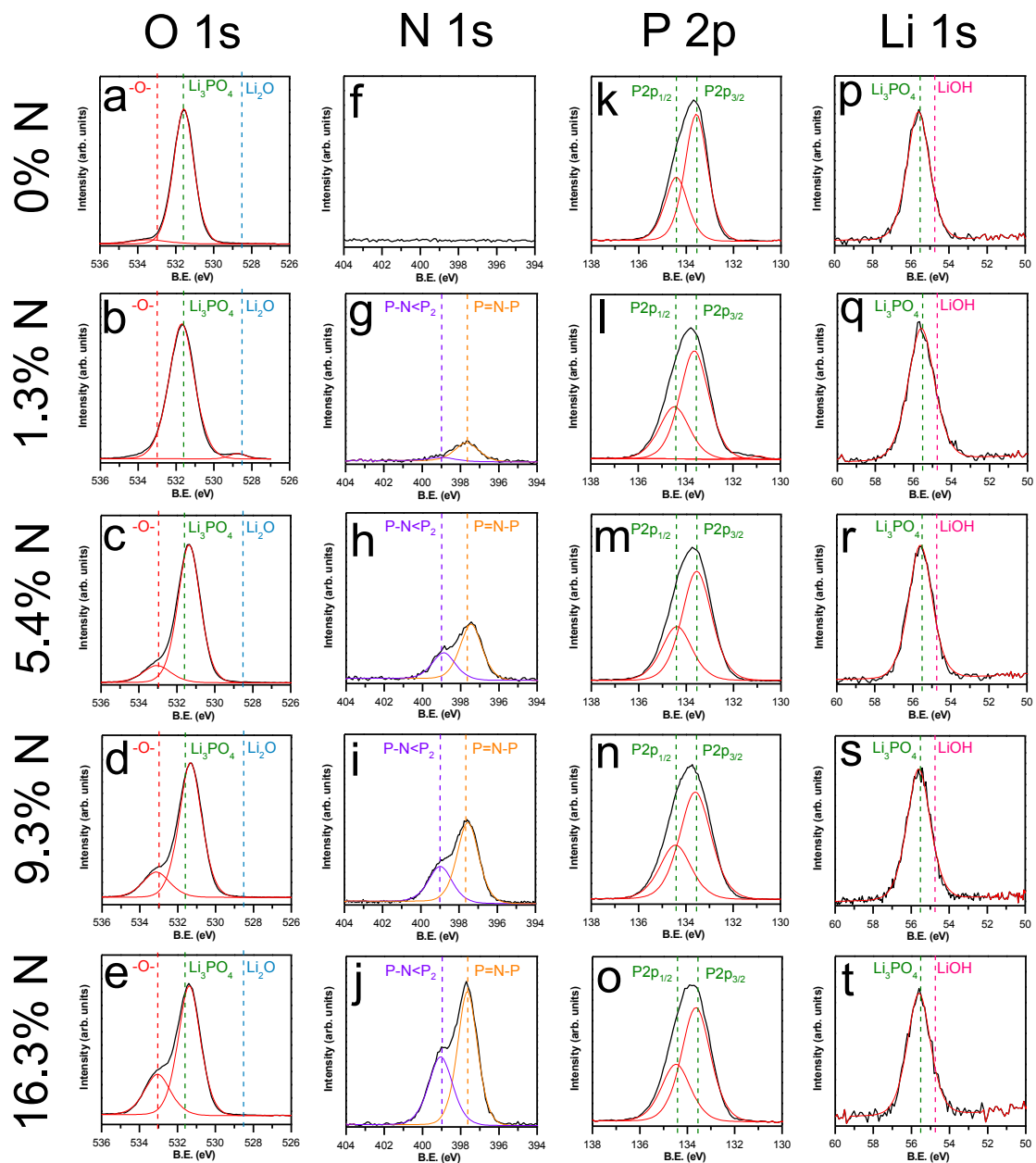


Figure 24. In-situ high-resolution core-level XPS spectra (columns) of as-deposited ALD LiPON at 250°C demonstrating nitrogen doping as a function of N₂ pulse time (rows). Spectra include deconvolution of multicomponent peaks. All ALD films shown here are ~50 nm thick.

In LiPON, nitrogen atoms are incorporated as bridging atoms between lithium-phosphate complexes in either a doubly coordinated or triply coordinated configuration

as seen in Figure 25. To date, no selectivity over the type of N incorporation into LiPON films has been conclusively demonstrated, and it is unclear if one species of N bonding is preferred over the other for enhanced ionic conductivity and material stability.

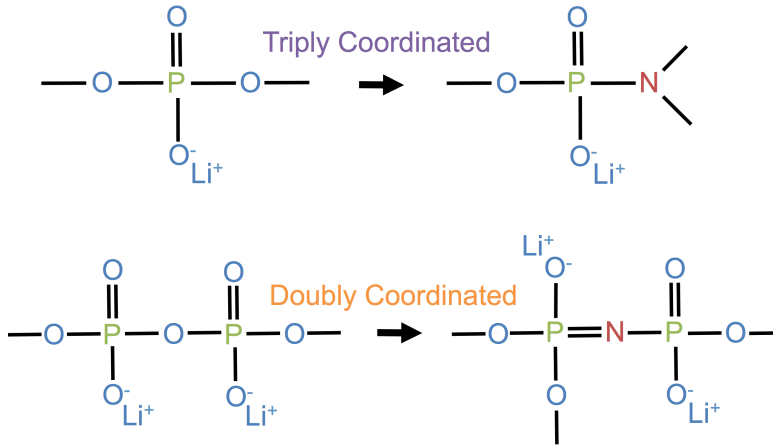


Figure 25. Cartoon representation of the two possible nitrogen coordination environments in LiPON: doubly and triply coordinated.

Despite the variable $^{15}\text{N}_2$ dose during the ALD process, the growth rate is relatively stable around 1.05 \AA/cycle , as shown in Figure 26a. The slope of the fit to the growth rate is within experimental

error. Figure 26b demonstrates the ratio of doubly coordinated N to triply coordinated N in the ALD LiPON is consistent with increasing N dose, indicating that as the N content is increased, the doping environment of the LiPON is chemically similar. This specific ratio of triply coordinated N to doubly coordinated N is likely due to the use of a single energy remote plasma to nitrogenate the films. Modification of the N radical energy in the plasma could likely modify this ratio, however this is currently instrumentation limited. The elemental ratios of the ALD LiPON films as determined by XPS are plotted in Figure 26c. As the $^{15}\text{N}_2$ dose is increased, ALD films transition from polycrystalline Li_3PO_4 to amorphous LiPON, as indicated by the XRD data in Figure 26d. This transition point occurs near 4.5% N content, as ALD LiPON deposited with a 5 second

$^{15}\text{N}_2$ dose remains polycrystalline, while ALD LiPON deposited with a 10 second $^{15}\text{N}_2$ dose is amorphous. To verify that this effect was due to the nitrogen content of the films and not the plasma dose, an ALD LiPON process was run using an Ar plasma instead of the usual $^{15}\text{N}_2$ step, resulting in the deposition of polycrystalline Li_3PO_4 films. Clearly, this indicates that LiPON amorphization is due to inclusion of N in glass forming networks and not as a result of the $^{15}\text{N}_2$ dose.

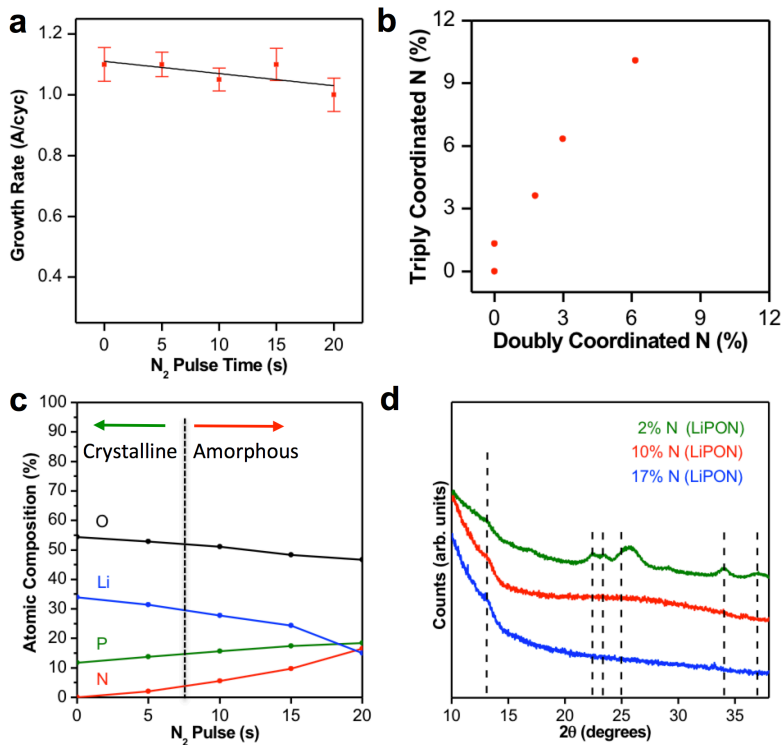


Figure 26. (a) Growth rate as a function of $^{15}\text{N}_2$ dose for ALD LiPON. (b) Ratio of doubly coordinated N to triply coordinated N in the LiPON structure as determined by XPS, indicating a uniform bonding environment as a function of N content. (c) Film stoichiometry as determined by peak fitting the high-resolution XPS peaks in Figure 2. (d) XRD data of 50 nm thick LiPON thin films demonstrating the crystalline to amorphous transition with increasing Nitrogen content.

AFM height maps of ALD LiPON films 40 nm thick with 1.8% N content (Figure 26a) and 16.3% N content (Figure 26b) clearly demonstrate this crystalline to amorphous transition with increasing N content of the ALD films. The RMS roughness of these films is 10.1 nm for the 1.8% N LiPON film, and 0.78 nm for the 16.3% N

LiPON film respectively. SEM images of the same samples are also presented in Figure

26c and Figure 26d, showcasing the film texture. Note that it is incredibly difficult to distinguish features on the SEM image of amorphous ALD LiPON; this is due to the incredible uniformity and lack of texture of the deposited film. This crystalline to amorphous transition is contrary to previous results, which found that sputter deposited Li_3PO_4 exposed to a high energy N_2 plasma discharge exhibited an amorphous to crystalline transition with increasing N content, though this is perhaps not surprising considering the drastically different deposition techniques.¹¹¹

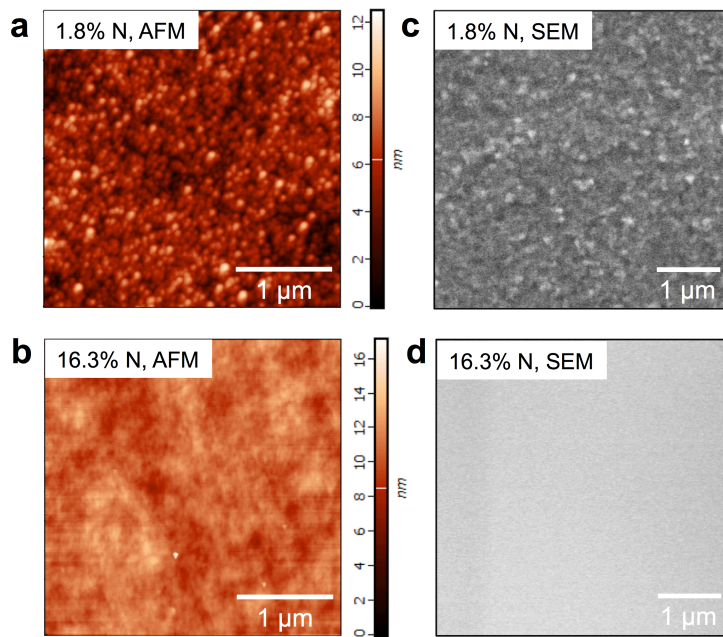


Figure 27. AFM height maps of (a) LiPON film with 2% N and (b) LiPON film with 17% N. (c) and (d) show SEM images of the same films in (a) and (b) to show texture.

One of the hallmarks of the ALD process is the ability to conformally coat high aspect ratio nanostructures with thin, uniform layers. Here, ALD LiPON films with varied N content are deposited on MWCNT sponge scaffolds for both morphological

imaging and ellipsometric thickness calibration. TEM images of MWCNTs covered with ALD LiPON films are shown in Figure 28.

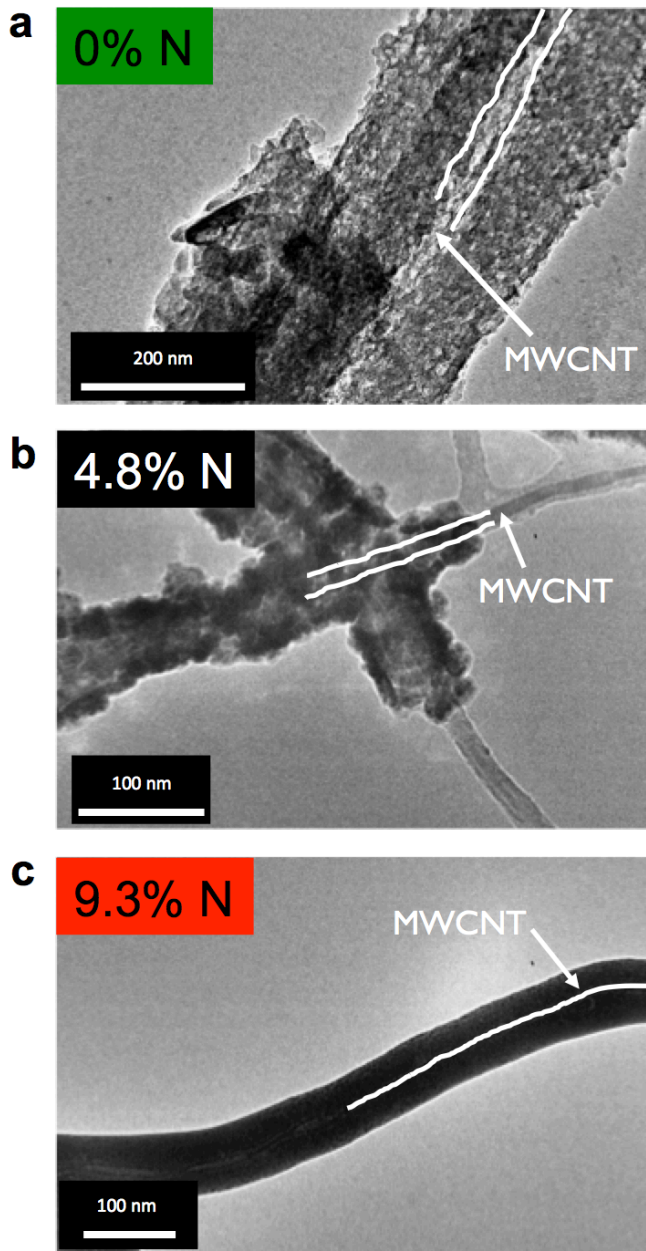


Figure 28. TEM images of ALD LiPON deposited on a MWCNT sponge with (a) 0% N, (b) 4.8% N, and (c) 9.3% N content. Both (a) and (b) are polycrystalline, while (c) is amorphous. The diameter of the MWCNTs is 30-40 nm.

The morphology of these LiPON films is consistent with the AFM and SEM data presented in Figure 27, and clearly demonstrates the uniform deposition possible on high aspect ratio scaffolds through the ALD process. Notably, while crystalline ALD LiPON is stable, amorphous ALD LiPON degrades rapidly upon electron beam exposure, consistent with others' observations.⁸⁹ Amorphous ALD LiPON deposited onto MWCNT substrates exposed to a 200 keV during electron beam during

TEM imaging is shown in Figure 29. After only 180 seconds of

beam exposure (a typical time required for focusing image collection), the ALD LiPON has melted and degraded significantly, making thickness measurements unreliable and

imaging pristine structures impossible. This mechanism is poorly understood and deserves further investigation, however such research is outside the scope of this thesis.

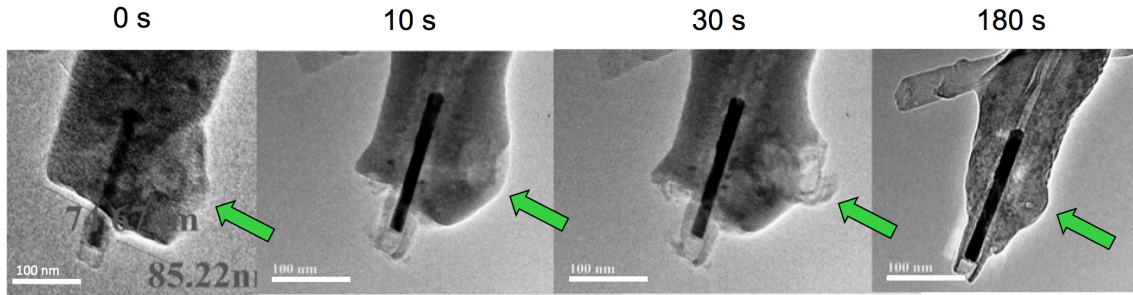


Figure 29. Beam damage to ALD LiPON deposited onto MWCNTs inside a TEM at 200 keV.

More accurate measurements of ALD LiPON thickness are collected using SEM imaging by deposition onto VLS grown silicon nanowires.¹¹⁹ These nanowires are ideal for imaging, as they contain a bead of gold catalyst on the tip of the wire. As the ALD LiPON process nucleates equally well on both Au and Si, imaging of these structures and measurement of the LiPON layer is possible by using the contrast between the Au and the covering LiPON layer in SEM. The lower energy of the electron beam during SEM imaging (10 kV typical) does not measurably degrade the LiPON films, and allows for accurate LiPON thickness measurements.

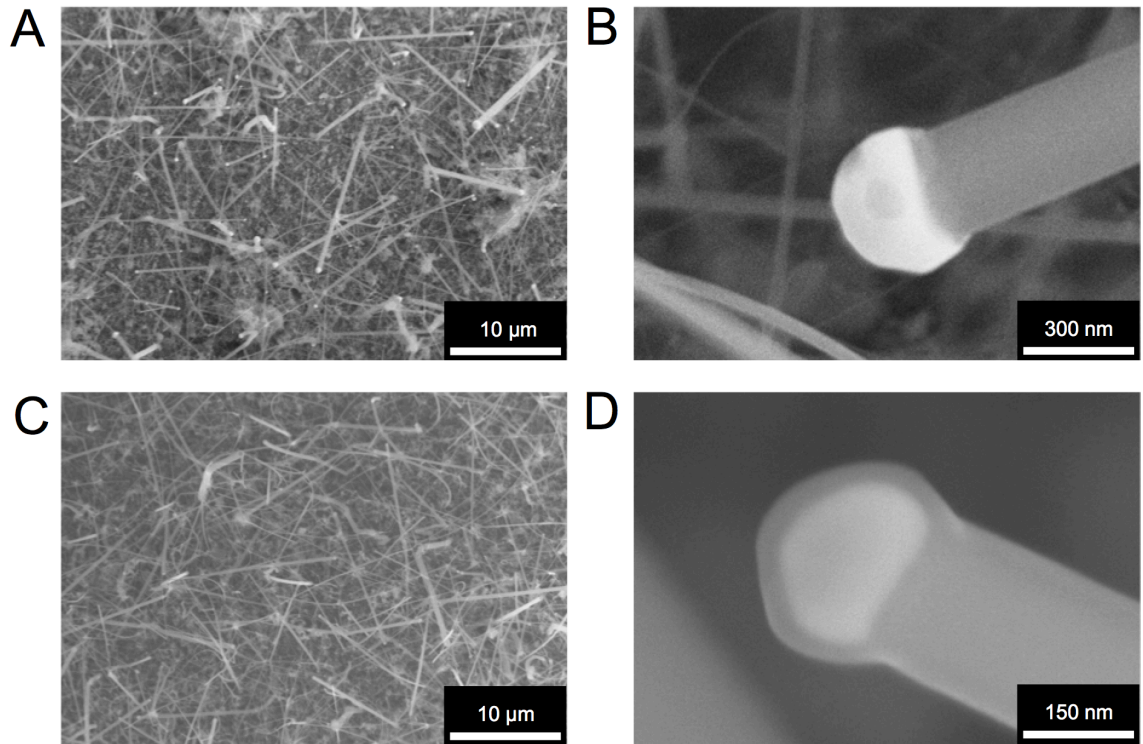


Figure 30. (a) Low resolution and (b) high resolution images of bare Si NWs grown directly on stainless steel substrates using VLS growth.^{119,120} (c) Low resolution and (d) high resolution images of Si NWs coated with 40 nm ALD LiPON.

ALD LiPON Ionic Conductivity Determination

The most common method of determining ionic conductivity of a material is electrochemical impedance spectroscopy (EIS), previously described in

Chapter II: Laboratory Design, Equipment. However, there are many different common experimental setups and associated electrochemical circuit models that can be used depending on the materials to be investigated. In this thesis, I use three different methods to investigate ionic conductivity of LiPON: (1) EIS measurements of LiPON assembled into CR2032 coin cells with a liquid electrolyte and a Li counter electrode, (2) EIS measurements of Au-LiPON-Au solid-state trilayer solid-state structures, and (3) direct ionic current measurements through a single nanopore filled with material.

CR2032 Coin Cells

In this case, the ionic conductivity of ALD LiPON was tested at various thicknesses and N contents by deposition onto stainless steel substrates, which were then assembled into CR2032 coin cells. EIS tests on these LiPON films as a function of film thickness, all with 5.5% N, are shown in Figure 31.

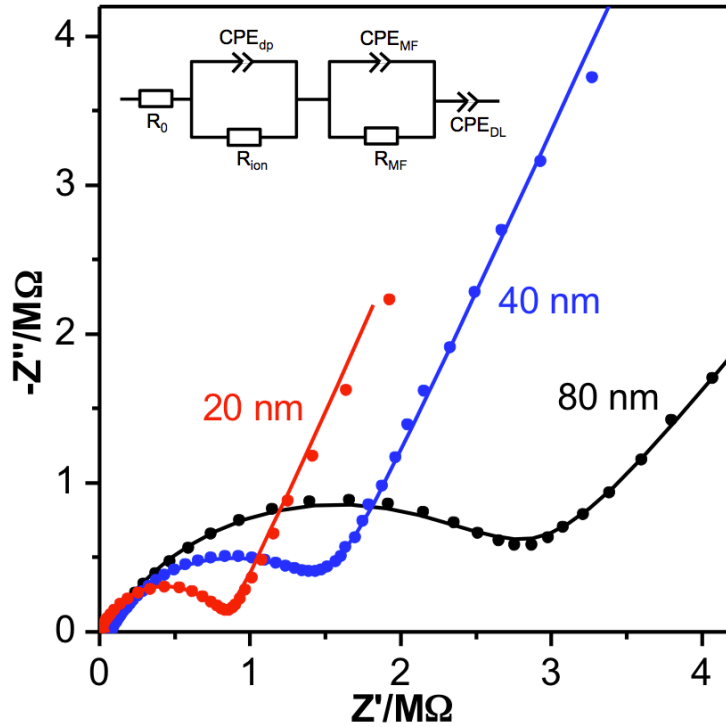


Figure 31. EIS curves for 20 nm, 40 nm, and 80 nm thick ALD LiPON working electrodes in coin cells with a Li metal counter electrode. Dots are measured data, lines are fits to the measured data using the inset circuit model used for impedance analysis adapted from Dudney.¹²¹

Using the circuit model for thin LiPON developed by Dudney (Figure 31 inset),¹²¹ the ionic conductivity is determined to be 1.45×10^{-7} S/cm $\pm 1 \times 10^{-7}$ S/cm, slightly lower than previously published results of sputter deposited LiPON with similar nitrogen content.¹²² However, this value represents the highest conductivity of any ALD

solid electrolyte reported to date^{104,114}. In this model, the ionic conduction is modeled by two pairs of resistors and constant phase elements (frequency-dependent capacitors) at both high (CPE_{dp}/R_{ion}) and medium (CPE_{MF}/R_{MF}) frequencies, as well as a double layer capacitance (CPE_{DL}) at low frequency. Table 1 shows the fitted circuit component values corresponding to the data in Figure 31.

Thickness (nm)	R_0 (Ω)	R_{ion} (Ω)	CPE_{ion} (F^a)	R_{MF} (Ω)	CPE_{iMF} (F^a)	CPE_{DL} (F^a)	Ionic Conductivity (S/cm)
80	3.165	27.74	.481	2768	7.56E-6	6.02E-3	1.45E-7
40	1.4E-2	13.97	.385	544	12.9E-6	4.58E-3	4.41E-7
20	2.4E-3	6.942	.771	809	4.99E-6	10.3E-3	1.45E-7

Table 1. Table of fitted values to circuit components for ALD LiPON thin films with 5% N content.

Dudney's model includes a parallel resistor to model the electronic leakage current detected in very thin LiPON films. However, the EIS measurement setup used in this thesis has the advantage that it adds an electronically insulating liquid electrolyte in parallel with the two conducting electrodes, eliminating the possibility of electronic leakage in our circuit. The ionic conductivity of the ALD LiPON does not change significantly with film thickness, and as such bulk ionic conductivity in the LiPON likely dominates over the interfacial impedance of ALD LiPON.

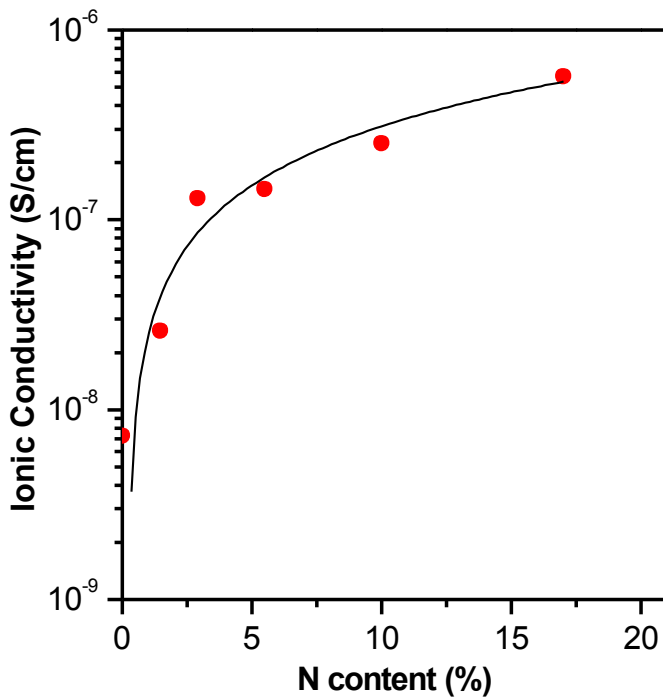


Figure 32. Ionic conductivity of ALD LiPON films plotted as a function of N content along with linear fit to the data.

The conductivity of sputtered LiPON has been reported to increase with increasing N content,⁶⁵ and indeed here a rather large increase in the ionic conductivity of the ALD LiPON is measured with nitrogen content increasing from 1.8% to 16.3%, plotted in

Figure 32. For non-doped ALD Li_3PO_4 , an ionic

conductivity of 6.5×10^{-9} S/cm is measured, in the range of acceptable values previously measured for the ionic conductivity of Li_3PO_4 .¹⁰⁶

Conductivity Measurements With Solid-State MIM Devices

Ideally, the ionic conductivity of ALD LiPON can be reliably measured using fully solid-state stacks to more appropriately model the LiPON performance in a solid-state battery due to the solid-state Au/LiPON interfaces. First, 50 nm Au was evaporated onto a silicon wafer, and then ALD LiPON was deposited on top of this Au bottom electrode. The corner of the wafer was masked from LiPON deposition by a small silicon chunk to maintain a clean bottom electrode contact area for electrical testing. The Au-LiPON stack was then removed from the integrated system, and 200 nm-thick top electrodes of Au were evaporated using a stainless steel shadow mask to define the top electrode area (500 μm diameter, Figure 33). EIS measurements on these MIM devices were performed using a *Bio-Logic* VSP potentiostat connected to a fully automated probe station in the ANSLab constructed by a previous graduate student. Bottom contact was made to the masked Au bottom electrode using a Cu clip as the counter electrode, while the working electrode was connected to an Au pin that made contact to one patterned Au top electrode at a time.

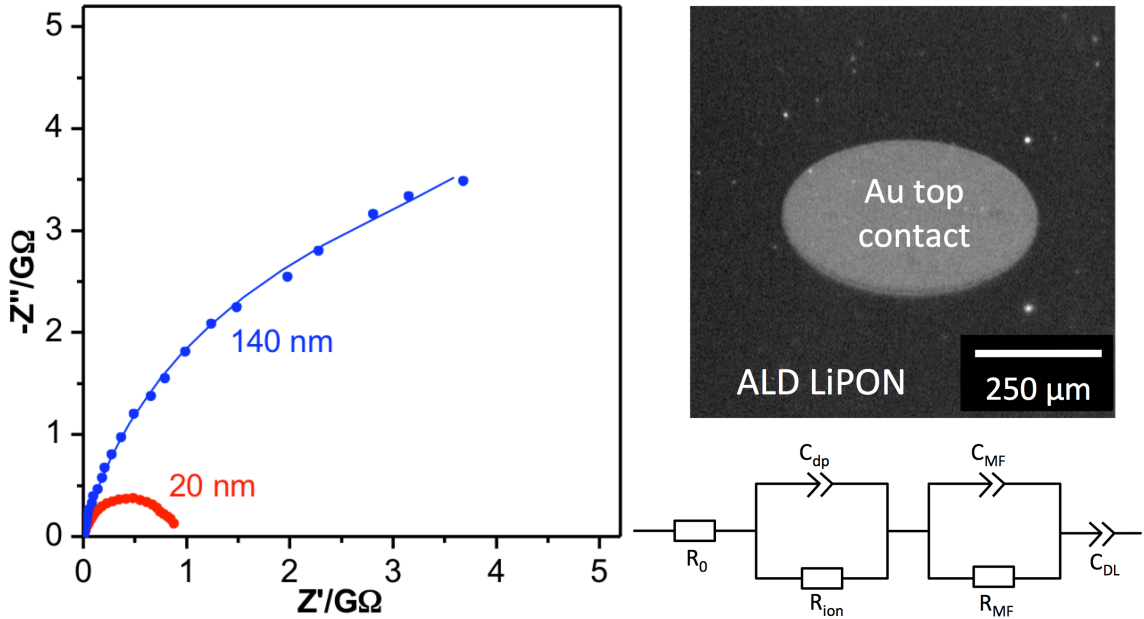


Figure 33. Two EIS plots of Au-LiPON-Au MIM trilayer structures along with data fits, along with an SEM image of one of the top Au contact pads and the same EIS equivalent circuit from Dudney.¹²¹

However, due to problems with device fabrication resulting in approximately 95% of the fabricated devices shorting, likely due to degradation from air exposure during the fabrication process, only two ALD LiPON films with thicknesses of 20 nm and 140 nm were successfully measured on Au-LiPON-Au trilayer devices. To prevent this issue in the future, fabrication will proceed entirely inside the glovebox, and the devices will be tested using an InGa eutectic droplet electrode to prevent physical puncturing of the top contact with the probe station needle. Fitting the previously described EIS model to these devices indicates resistance values corresponding to an ionic conductivity of 8.5×10^{-6} S/cm for both thicknesses, an order of magnitude higher than the conductivity determined using the coin cell measurements. This higher conductivity may be due to electronic leakage currents from one Au electrode to the other in the MIM structure, which the EIS model cannot adequately distinguish from ionic conductivities. While the accepted value

of the electron conductivity of LiPON is 1×10^{-12} S/cm,¹²² similar high leakage currents have been seen in LiPON films less than 20 nm thick.¹²¹ MIM device shorting may be due to a number of different factors: air exposure of the ALD LiPON during loading into the vacuum chamber for top electrode evaporation, electrical testing in atmosphere after top electrode fabrication, or even mechanical damage of the ALD films during the electrical testing procedure.

Single Nanopore Conductivity Measurements

The last method used to measure ionic conductivity of ALD LiPON is a novel method developed by and operated in collaboration with professor Zuza Siwy at UC Irvine.¹²³⁻¹²⁵ This method relies on measurement of ionic current between two electrodes immersed in two electrolyte reservoirs. A SiN membrane with a single nanopore (drilled by a high-energy electron beam inside a TEM) is placed between these reservoirs, allowing ion transport between both reservoirs to be detected by the electrodes. A schematic of the experimental setup is shown in Figure 34A. This technique is advantageous in that it can determine ionic conductivity of the material inside a single nanopore without electronic leakage influencing the measurement. Also, direct measurement of ion current through the nanopore using an applied voltage sweep is an improvement over fitting EIS models to impedance spectroscopy data. Use of an empty nanopore can measure the ionic conductivity of the liquid electrolyte solution in the cell, while filling the nanopore with some other material allows direct measurement of the material inside the nanopore. In this case, ionic current is measured through an empty 12 nm diameter, 30 nm length nanopore. The nanopore is filled with ALD LiPON, and then the conductivity

experiment is repeated. The resulting data from a first attempt at this measurement is shown in Figure 34B, demonstrating the decreased ionic conduction through the LiPON filled nanopore over the liquid electrolyte filled nanopore.

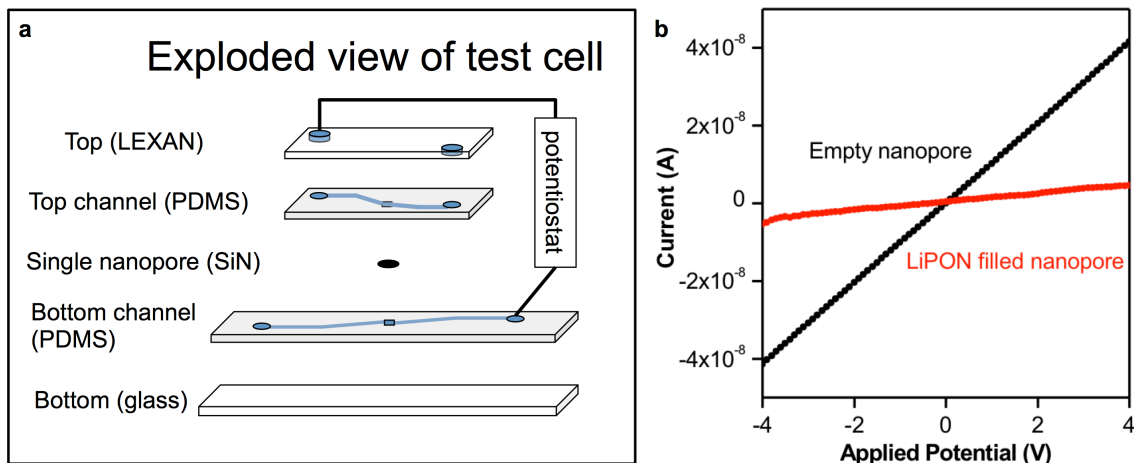


Figure 34. (a) Cartoon representation of the single nanopore ionic conductivity experimental setup. (b) I - V curves of the same empty and ALD LiPON-filled nanopore.

Analysis of these data indicates that the ionic conductivity of the ALD LiPON filled nanopore is approximately 1×10^{-3} S/cm, well above the expected ionic conductivity measured in the two previously described techniques. This discrepancy may be due to degradation of the ALD LiPON due to air exposure during shipping from Maryland to California, due to degradation from reactions with water dissolved in the liquid electrolyte during testing, or due to only partial filling of the nanopore with the ALD LiPON. However, this measurement has demonstrated the utility of the technique to measure the ionic conductivity of materials inside a single nanopore, and the research collaboration still ongoing.

Chapter Summary

I have demonstrated the first reported ALD process for the solid lithium electrolyte LiPON, and shown the ability to modify the N content in the LiPON films from 0% up to 16.3% N by variation of the plasma nitrogen dose at a specific location in the ALD sequence. Ionic conductivity of ALD LiPON has been measured by three different methods, however there remains some unresolved discrepancy among the measurements achieved using these techniques.

The combination of highly tunable thickness during growth, tunable N content, and the ability to conformally deposit LiPON onto high aspect ratio nanostructures is an incredibly desirable combination anticipated to enable deposition of solid electrolyte protection layers onto challenging electrode geometries, as well as enable fabrication of next-generation, 3D solid microbatteries. This work has been submitted to ACS Chemistry of Materials and currently under review.

Chapter VI: Lithium Metal Protection with ALD Solid Electrolytes

Solid Electrolyte Interphase

The solid electrolyte interphase, or SEI, is a degradation byproduct formed at the electrode/electrolyte interface in conventional Li-ion batteries. This layer is composed of reduction products of the liquid electrolyte and lithium halide salts, primarily LiF, Li₂CO₃, but also composed of many different polymeric degradation byproducts.^{126,127}

The SEI serves to stabilize the anode surface upon repeated cycling, however formation of this layer is poorly controlled. Increasing SEI thickness increases cell impedance, eventually leading to high overpotentials upon recharge that can cause Li plating, dendrite formation, and subsequent cell shorting and spectacular failure.¹²⁸

ALD LiPON as an Artificial SEI Layer

One use of ALD coatings has been to apply artificial SEI layers to both anode and cathode materials.^{55,129-131} These coatings are generally made of well-known metal oxide ALD coatings such as ZrO₂, TiO₂, and Al₂O₃. As these metal oxides generally have low ionic conductivities on the order of 1×10^{-10} S/cm, the layer thickness must be < 2 nm to prevent unacceptable impedance increases of the electrodes. Use of higher ionic conductivity coatings such as LiPON enable deposition of thicker artificial SEI layers (on the order of 50 nm and above) to increase both the mechanical stability and electrochemical stability of the electrodes while still allowing acceptable lithium kinetics through the protection layer.^{64,66,67} The drawback of many solid-state ionic protection

coatings is the physical vapor deposition processes used, which suffer from poor thickness control and low interfacial quality.^{37,132}

LiPON For Silicon Electrode Stabilization

In order to demonstrate ALD LiPON's function in a model electrochemical system, LiPON films were applied to sputtered amorphous silicon anodes on copper current collectors, as well as to the bare Cu current collector in order to determine the influence of the ALD LiPON layers on lithiation behavior of the underlying silicon. CV scans of these anodes collected between 10 mV and 1.2 V vs Li/Li⁺ at .1 mV/s sweep rate are shown in Figure 35. The ALD LiPON deposited directly on the Cu current collector shows a lack of peaks in the CV, indicating a lack of redox reactions occurring during lithiation/delithiation in LiPON, expected behavior for an ionic capacitor. Notably, a cathodic current increase due to electrolyte reduction and SEI formation is also not obtained even near 0V vs Li/Li⁺, suggesting the LiPON film is an effective barrier for electron transfer from the electrode to the organic electrolyte.

The uncoated silicon anode behaves electrochemically as expected, with two cathodic peaks associated with the organic electrolyte breakdown and lithiation of the silicon, at ~300 mV and ~180 mV respectively.⁹ Application of both 20 and 40 nm ALD LiPON coatings on the silicon completely extinguishes the cathodic peak associated with SEI formation. On the anodic scan, two peaks commonly associated with delithiation are seen for both uncoated and LiPON coated silicon.

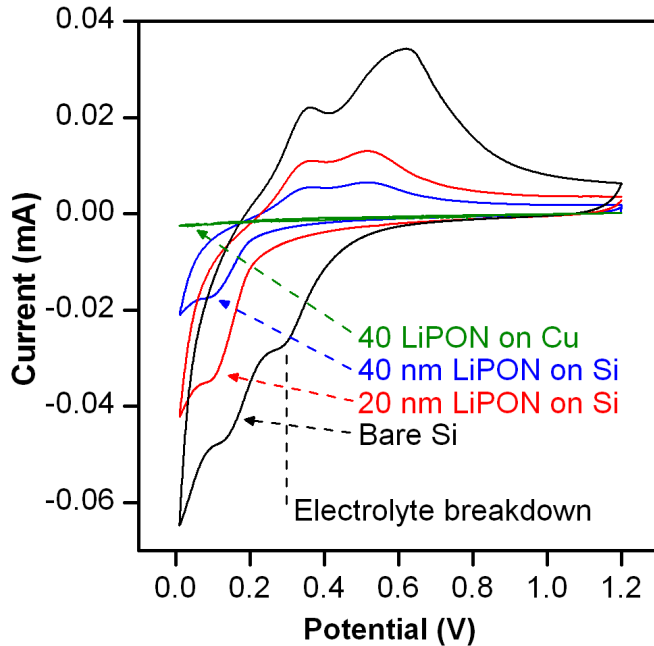


Figure 35. CV curves of (black) bare sputtered Si; (red) 20 nm ALD LiPON on sputtered Si; (blue) 40 nm ALD LiPON on sputtered Si; (green) 40 nm ALD LiPON on Cu. The sweep rate for all CV scans was 0.1 mV/s in 1:1 EC:DEC with 1M LiPF₆ electrolyte and a Li metal counter electrode.

Thicker LiPON layers do show a reduced current response to the applied potential sweep in both anodic and cathodic scan regions, indicating that the impedance of the coated anodes increases with increasing LiPON film thickness as expected.

Lithium Metal Anode Protection

Lithium metal is considered the most promising anode for next-generation batteries due to its high energy density of 3840 mAhg⁻¹. However, the extreme reactivity of the Li surface can induce parasitic reactions with solvents, contamination, and shuttled active species in the electrolyte, reducing performance of batteries employing Li metal anodes. One promising solution to this issue is application of thin chemical protection layers to the Li metal surface. Using a custom made ultrahigh vacuum (UHV) integrated deposition and characterization system, we demonstrate atomic layer deposition (ALD) of protection layers directly on Li metal with exquisite thickness control. We demonstrate as a proof of concept that a 14 nm thick, ALD Al₂O₃ layer can protect the Li surface from corrosion due to atmosphere, sulfur, and electrolyte exposure. Using Li-S battery cells as a test system, we

demonstrate an improved capacity of 60% using ALD Al₂O₃ protected anodes over cells assembled with bare Li metal anodes for up to 100 cycles, while we demonstrate a capacity improvement of 6X using 20 nm LiPON protected anodes for up to 35 cycles.

Motivation

The ever increasing demand for higher energy density storage devices for transportation (electric vehicles), grid storage (power leveling), and other applications is challenging the scientific community to develop a rechargeable battery with cycle life comparable to Li-ion but with significantly higher capacity. Major R&D centers increasingly look to metal anode systems, including Li-S, Li-O₂, and advanced oxide cathode systems combined with Li metal anodes for increased performance. Recent analysis of beyond-Li-ion options by the Joint Center for Energy Storage Research (JCESR) highlights the high priority for metal anode systems, while recognizing that the reactivity of the metal anode poses serious technical and manufacturing challenges⁸.

Realization of stable Li metal anodes in rechargeable batteries is a challenge with many facets. From a processing perspective, lithium metal will oxidize and corrode under atmospheric conditions via reaction with H₂O and CO₂ via the stepwise reactions



producing a characteristic black tarnish on the Li metal surface⁷⁷. This oxidation is prevented by limiting the exposure of the Li metal to H₂O, necessitating the use of costly dry rooms for lithium metal extrusion and battery assembly.

From an operational point of view, lithium's high reactivity with most organic chemicals used in battery electrolytes causes corrosion reactions to occur during cycling due to reduction of solvents, active species, or impurities, leading to degradation of the anode, consumption of electrolyte and active materials, and eventual battery failure.

Lithium metal protection is particularly important in systems where the active material diffuses freely through the electrolyte (e.g. polysulfide in Li-S cells), or if inherent contamination is present in the electrolyte (e.g. H₂O, CO₂, and N₂ in a real Li-air system). In both of these cases the highly reactive Li anode forms a high impedance solid electrolyte interphase (SEI) layer on its surface consuming electrolyte and active material resulting in practical capacity loss and low of coulombic efficiency⁷⁸.

Previous attempts to passivate Li metal with organic molecules^{79,80} and polymeric coatings⁸¹ have achieved limited success due to poor thickness and compositional control of the applied protection layer. Protection with sputtered solid electrolytes^{64,83}, while effective at preventing electrolyte decomposition on the Li metal surface can result in large cell overpotentials during recharge at even moderate rates due to the large thicknesses (~μm) of the sputtered solid electrolytes. Recently, protection of the Li surface with self-assembled carbon spheres⁸⁴ has proven effective at preventing Li dendrite growth upon cycling, but offers limited options for scalable manufacturing and also adds significant mass to the anode.

We suggest a new approach to study Li metal surface stabilization via application of ALD protection layers directly on the Li, creating a new thin phase between the metal and various corrosive surroundings. Using a unique UHV system described elsewhere⁸⁶,

we deposited ALD Al_2O_3 coatings directly on Li metal foil to mitigate corrosion reactions due to both atmosphere and electrolyte exposure. We determine and measure directly, for the first time, the nominal layer thickness for effective Li metal protection, and we use Li-S cells to demonstrate a dramatic capacity increase of protected Li metal anodes over their unprotected counterparts via mitigation of the Li corrosion by Sulfur species shuttling in the electrolyte⁸⁷. While the focus of this work is on Li metal anodes, our study opens a new opportunity for realization of other metal anode based systems such as Na and Mg rechargeable batteries, and for protection of those metal by various thin layers deposited atomically or molecularly.

Deposition of ALD Protection Coatings on Lithium Metal Anodes

ALD is ideally suited to Li metal protection due to its unique properties of angstrom-scale thickness control, pinhole-free conformal films, and low temperature deposition below the melting point of lithium (180°C).⁴³ ALD coatings have proven to be effective passivation layers for metals such as Cu,¹³³ Mg,¹³⁴ and Steel¹³⁵ from corrosion in electrolytes, and effective water vapor transmission barriers on polymers¹³⁶ and even reactive metals such as Ca.¹³⁷ In batteries, thin ALD coatings have been applied to non-metallic anodes^{57,138-140} and cathodes^{129,141,142} to improve battery cycling performance, however to maintain high ionic conductivities without increasing cell impedance these ALD coatings are less than 2 nm thick. In contrast to these previous studies, we find that < 2 nm ALD coatings are not of sufficient thickness for Li metal protection.

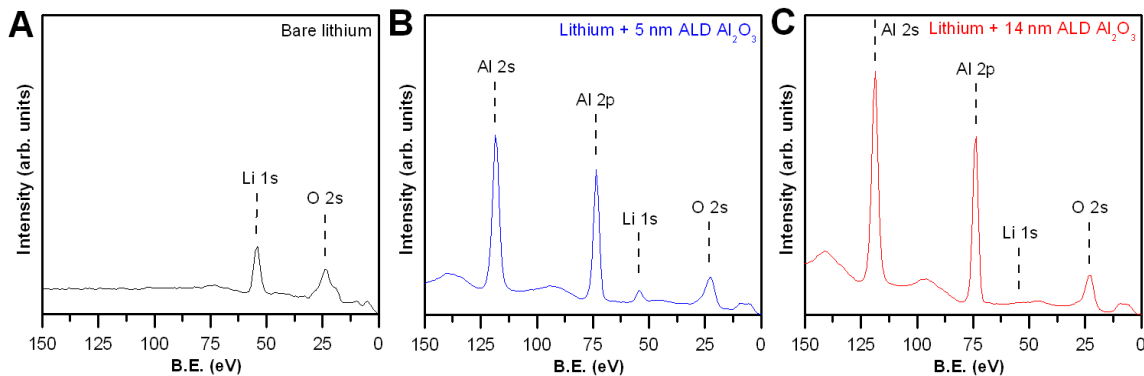


Figure 36. XPS survey spectra of (a) pristine Li metal; (b) uncycled Li metal protected with 5 nm ALD Al_2O_3 ; and (c) uncycled Li metal protected with 14 nm ALD Al_2O_3 .

This section focuses exclusively on ALD Al_2O_3 protection layers, due to the ideal ALD process chemistry able to coat Li metal, and the known lithiation mechanism of Al_2O_3 to form the stable, ionically conductive $\text{Li}_x\text{Al}_2\text{O}_3$ alloy.¹⁴³ While the surface of the Li metal is covered with a native oxide as seen in the Li 1s photoelectron peak in Figure 36A, this peak is extinguished after application of a 14 nm thick ALD protective layer as shown in Figure 36C, which only contains photoelectron peaks consistent with Al_2O_3 . Figure 36B shows 5 nm ALD Al_2O_3 directly on Li metal, which exhibits characteristic photoelectron peaks of both Al_2O_3 and Li metal. At 14 nm, the ALD layer is thicker than the escape depth of the photoelectrons; therefore a lack of a Li 1s peak after application of the Al_2O_3 layer indicates not only that the ALD coating is uniform and pinhole-free, but also that the top ~8 nm of the layer does not lithiate during the ALD process at 100°C. XPS Spectra of thinner ALD layers on Li metal (not shown) do exhibit the Li 1s photoelectron peak, indicating that either these films are thinner than the escape depth of the photoelectrons from the underlying Li metal or may contain pinhole defects.

Lithium Corrosion Prevention in Three Environments

We take a stepwise approach to testing the effectiveness of our ALD protection layers on Li metal surfaces, with the intent of simulating three environments where opportunities for contamination and subsequent chemical corrosion occur either during Li metal processing, battery assembly and storage, and finally during battery operation.

Atmospheric Corrosion

To test the effect of ALD protection layers against atmospheric corrosion of Li metal by H₂O and CO₂ we exposed pristine and ALD Al₂O₃ protected Li metal foil to a controlled laboratory environment of 20°C and 40% R.H. Periodic photographs of the Li metal surface were taken under controlled lighting and camera conditions, and then *ImageJ* was used to calculate the amount of surface corrosion that had occurred. Figure 37A tracks the percent of Li surface tarnishing as a function of air exposure time. Notably, un-protected lithium metal begins tarnishing almost immediately after air exposure (< 1 minute), while lithium foils coated with 14 nm ALD Al₂O₃ can prevent the onset of surface tarnishing by 20 hours, with higher thicknesses both delaying the onset of measurable surface tarnishing as well as hindering the tarnishing rate once it begins.

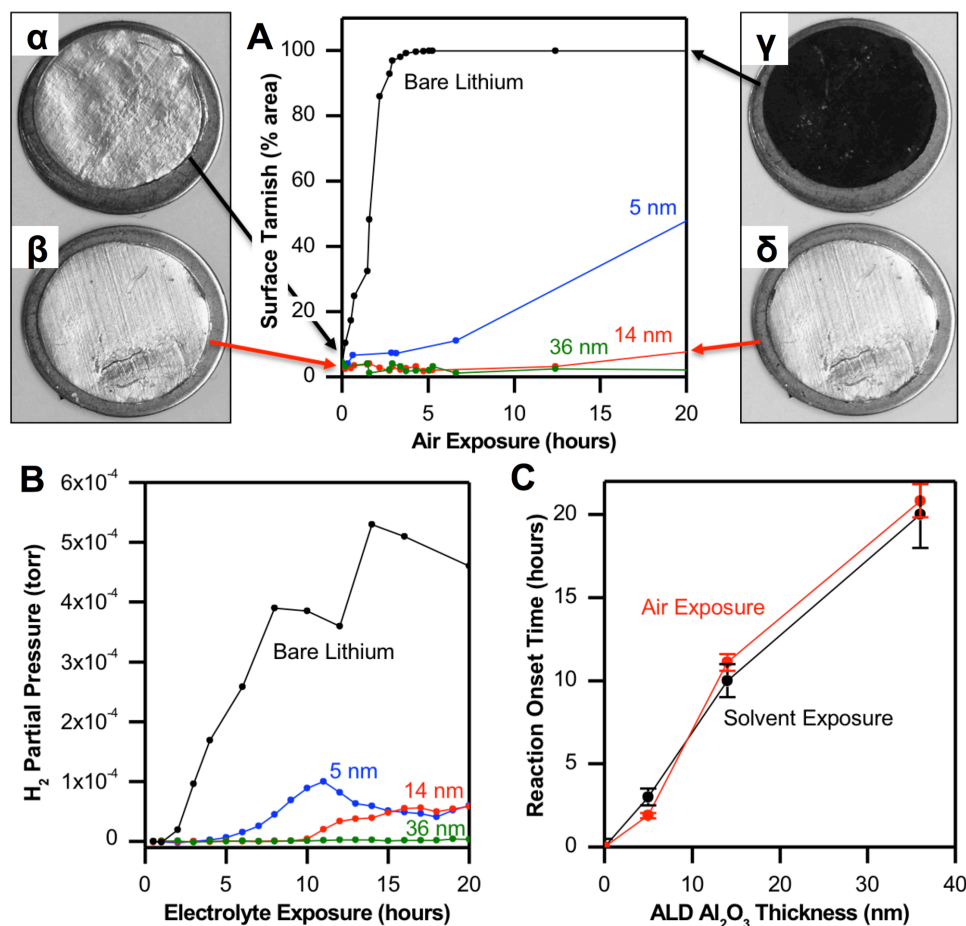


Figure 37. (a) Optical analysis of lithium foil surface tarnishing during atmospheric exposure at 25°C and 40% R.H. (b) Evolution of H₂ gas during organic solvent exposure. (c) Correlation between onset time for atmospheric tarnishing and onset time for H₂ evolution. (α) Unprotected and (β) 14 nm ALD Al₂O₃ protected Li metal foil immediately upon removal from an argon atmosphere. (γ) Bare and (δ) 14 nm ALD Al₂O₃ protected Li metal foil after 20 hours exposed to atmosphere at 25°C and 40% R.H.

Organic Solvent Corrosion

As a test case for the efficacy of ALD protection layers at preventing decomposition due to reactions with organic solvents, we immersed bare and protected Li in propylene carbonate (PC). By using differential quadrupole mass spectroscopy (dQMS) we sampled the gaseous byproducts evolved during the reaction of ALD Al₂O₃ protected and unprotected Li metal with PC. PC was chosen for its known high reactivity with Li

surfaces;¹⁴⁴ indeed the auto-decomposition of PC has been studied as a protection agent of Li surfaces for Li-air batteries.¹⁴⁵ Second, PC has a low vapor pressure, making it suitable for mass-spec headspace sampling without appreciable loss of electrolyte volume over long periods of time (e.g. days). Our approach enables quantitative detection of the gas phase products evolved due to surface reaction of the electrolyte on the interface of bare and protected metallic Li, however for the purposes of this study we only measure the evolved H₂ gas from these solutions, as H₂ gas is a viable indicator of multiple Li metal corrosion and electrolyte decomposition reactions.

In Figure 37B, the H₂ partial pressure in the container headspace is plotted as a function of time for various Al₂O₃ protection layer thicknesses. Hydrogen evolution from Li metal anodes is a well-known indicator of corrosion reactions.¹⁴⁶ These data indicate the onset time for H₂ evolution is linearly proportional to thickness of ALD layer, implying that contamination is diffusing through the ALD layer to the Li metal surface. Additionally, after onset of H₂ evolution, the H₂ partial pressure in the headspace above the ALD protected Li is one order of magnitude lower than that of the bare Li, indicating that ALD protection also reduces the extent of anode degradation *via* parasitic reactions with the electrolyte. This is with good agreement to what we found with the air exposure, as the ALD protection layer is both delaying corrosion and hindering the corrosion reaction once it begins. This is attributed to a self-healing mechanism in which ALD protection layers < 15 nm contain defects which localize electrolyte decomposition reactions, however once a stable phase is formed at these defect sites the corrosion reaction is diminished to match that of the fully protected Li metal.

Both of these experiments demonstrating direct comparison of the reactivity of pristine and protected Li metal allow us to extract a relationship between protection layer thickness and degree of lithium protection, shown in Figure 37C. Remarkably, ALD Al_2O_3 has an effective protection thickness dependence of approximately .56 nm/hour, independent of atmosphere or liquid exposure environment, suggesting that the duration of Li metal protection can be anticipated by careful tailoring of the ALD protection layer thickness.

Dramatic photographic evidence of this protection is exhibited *via* the remarkable optical differences in the lithium surface between unprotected and protected Li metal upon initial air exposure (Figure 37 α and Figure 37 β respectively) and after 20 hours of air exposure (Figure 37 γ and Figure 37 δ respectively) at 25°C and 40% R.H.

Sulfur/DME Corrosion

The efficacy of the Al_2O_3 protection layers on the Li surface was tested by soaking in a solution of dimethoxyethane (DME) and elemental sulfur to simulate a fully assembled Li-S battery in storage. Although the solubility of elemental sulfur from the cathode in glyme electrolytes (commonly used for Li-S batteries) is relatively low, it can still allow enough sulfur in the electrolyte to induce Li anode corrosion. First, long chain soluble Li polysulfides (PS) are formed, changing the visual appearance of the DME solvent from clear to yellow-brown. This effect is shown in Figure 38, where bare Li metal readily forms PS in solution, while 14 nm ALD Al_2O_3 protected Li metal soaked in the same solution demonstrates remarkable stability against spontaneous PS formation.

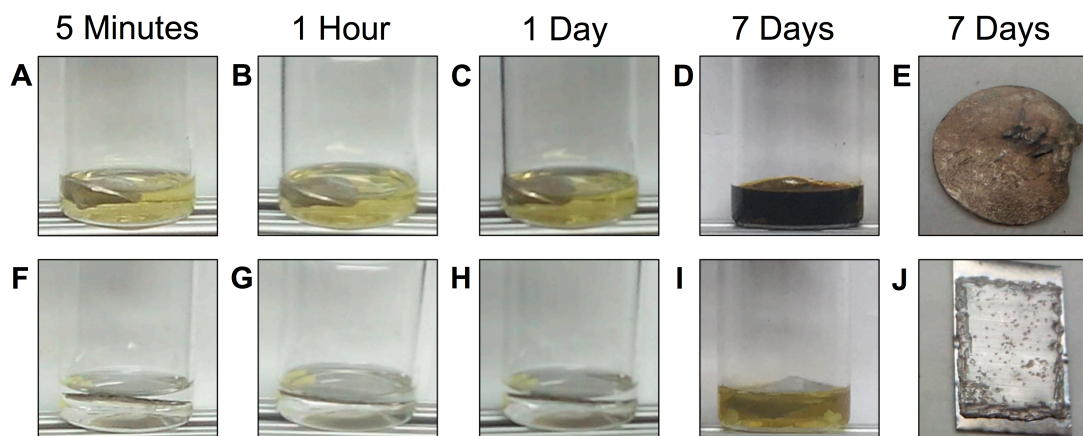


Figure 38. Optical images of (a-e) unprotected and (f-j) 14 nm ALD Al_2O_3 protected Li metal foil soaked in 1M sulfur/DME solution for 7 days.

Once long chain PS are formed in the organic solvent solution, these PS are further reduced into short chain PS and precipitate as insulating Li_2S on the Li anode surface. Bare and protected Li metal soaked in DME/S for 7 days, then washed with pure DME are shown in Figure 38. Clearly, there is significant PS deposition on the bare Li metal surface, while the ALD protected metal surface exhibits improved stability and appears optically similar to the unreacted Li metal surface. SEM images of these surfaces are shown in Figure 39, which in the case of bare Li metal exhibit major morphological changes, while the ALD protected Li metal surface remains intact and relatively free from electrolyte decomposition byproducts.

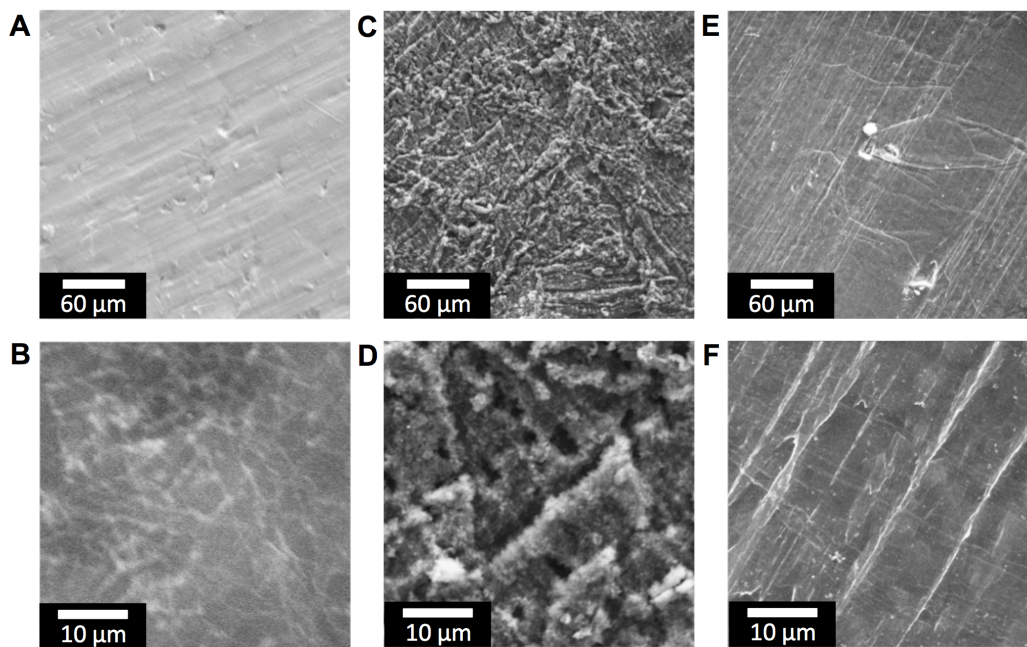


Figure 39. SEM images of (a,b) unprotected Li metal before solvent exposure. (c,d) unprotected Li metal after 7 days exposure to DME/sulfur solution; (e,f) 14 nm ALD Al₂O₃ protected Li metal surface after 7 days exposure to DME/sulfur solution.

This effect may cause Li corrosion even when the battery cell is resting before the start of cycling, and drastically reduces the performance of Li-S cells after manufacture before the battery is placed into service by consuming available sulfur from the cathode into non-electrochemically active species.

Lithiation Behavior of the Protected Anode

Figure 40 shows the CV and impedance responses for both unprotected and 14 nm Al₂O₃ protected lithium metal working electrodes cycled between -1V and 1.1V vs. Li in a Tee-cell configuration to strip and re-plate Li from the working electrode in order to test the influence of the protection layers on the faradaic processes on the anode surface.

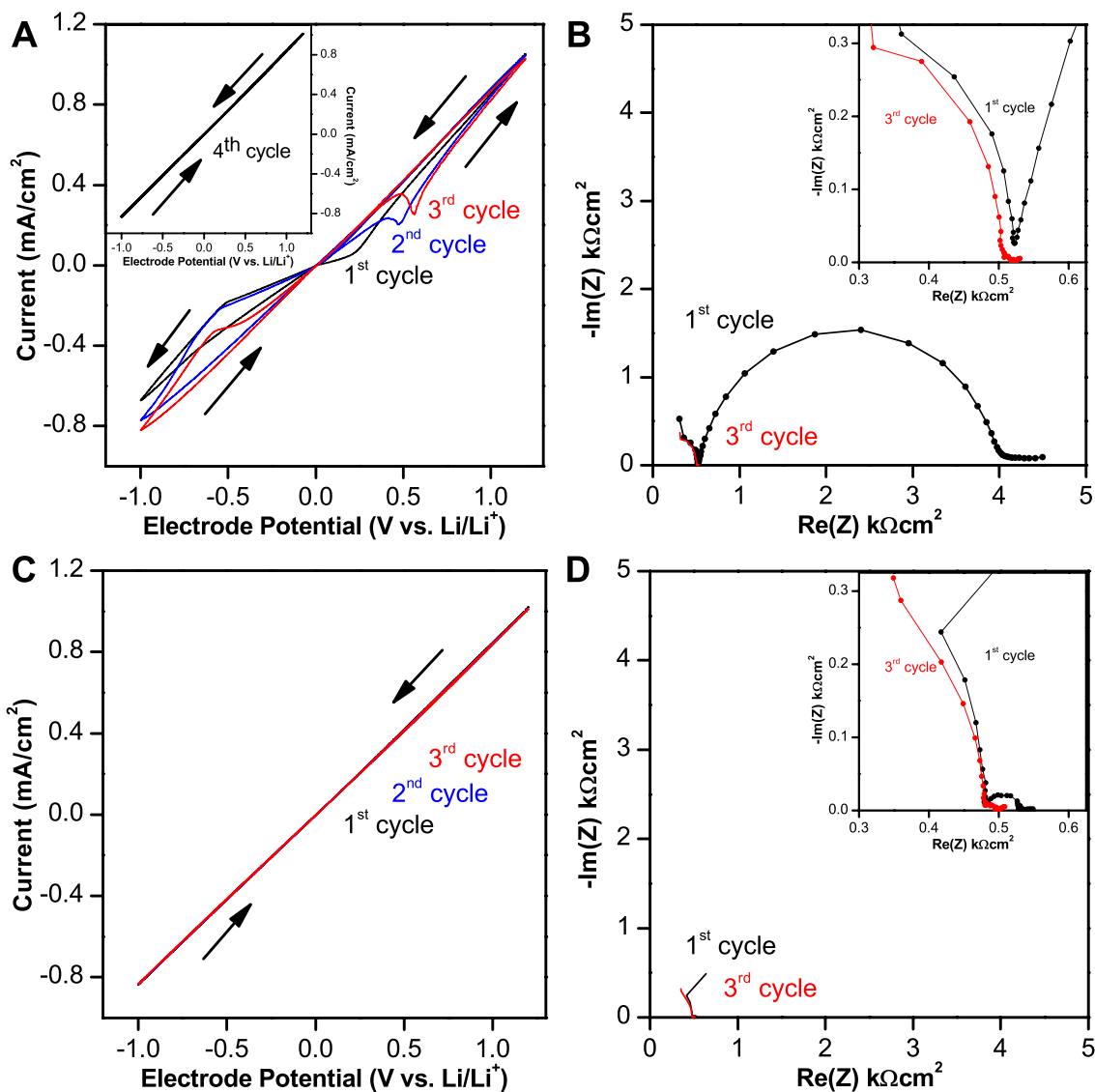


Figure 40. (a) Plot of the first 3 CV cycles of a lithium metal anode protected with 14 nm ALD Al_2O_3 . Inset: 4th CV cycle. (b) Nyquist plot showing EIS of the same protected lithium metal anode after the first (black) and 3rd (red) CV cycles. Inset: expanded region to illustrate high-frequency region of the EIS plot in (b). (c) Plot of the first 3 CV cycles of a bare lithium metal anode. (d) Nyquist plot showing EIS of the same bare lithium metal anode after the first (black) and 3rd (red) CV cycles. Inset: expanded region to illustrate high-frequency region of the EIS plot in (d).

The cathodic scan in Figure 40A on the protected electrode shows two different domains with two different slopes for Li plating, whereas the cathodic scan of the bare Li

metal in Figure 40C exhibits only 1 line with an identical slope. After the first 3 CV cycles, the plating and stripping behavior of both anodes is identical (Figure 40A inset). We attribute the dual-slope behavior of the protected Li CV to a changing impedance for Li plating resulting from initial lithiation of the Al_2O_3 layer followed by a subsequent impedance decrease at lower potentials after further lithiation of the Al_2O_3 (Figure 40B, Figure 40D). For the anodic scan regions similar lithiation behavior was achieved and maintained for the first 3 cycles, while again after the first 3 CV scans the protected anode exhibits identical behavior to the bare Li anode.

While the CV study of the protected and unprotected Li anodes shown in Figure 40 represents the behavior of the $\text{Li}/\text{Al}_2\text{O}_3$ interface during a potential sweep, the Li anode does not experience a voltage shift of 1.2V vs. Li/Li^+ in a real battery. Instead, the Li anode responds to relatively small shifts of the anode voltage by supplying compensation current. Therefore the effect of both the 14nm Al_2O_3 layer and a 20 nm LiPON layer on the overpotential of the Li anode during galvanostatic (GV) cycling of symmetric cells were tested. Overpotential and impedance spectra (EIS Nyquist plots) of symmetric cells composed of 2 bare Li electrodes, and a symmetric cell composed of 2 Al_2O_3 protected Li electrodes shown in Figure 41 demonstrate that the overpotential increase upon application of 1 mAcm^{-2} (a reasonable current density for a working battery) is minimal. However, application of the high conductivity LiPON coating actually reduces the overpotential during cycling compared to a bare Li anode, as shown in Figure 42.

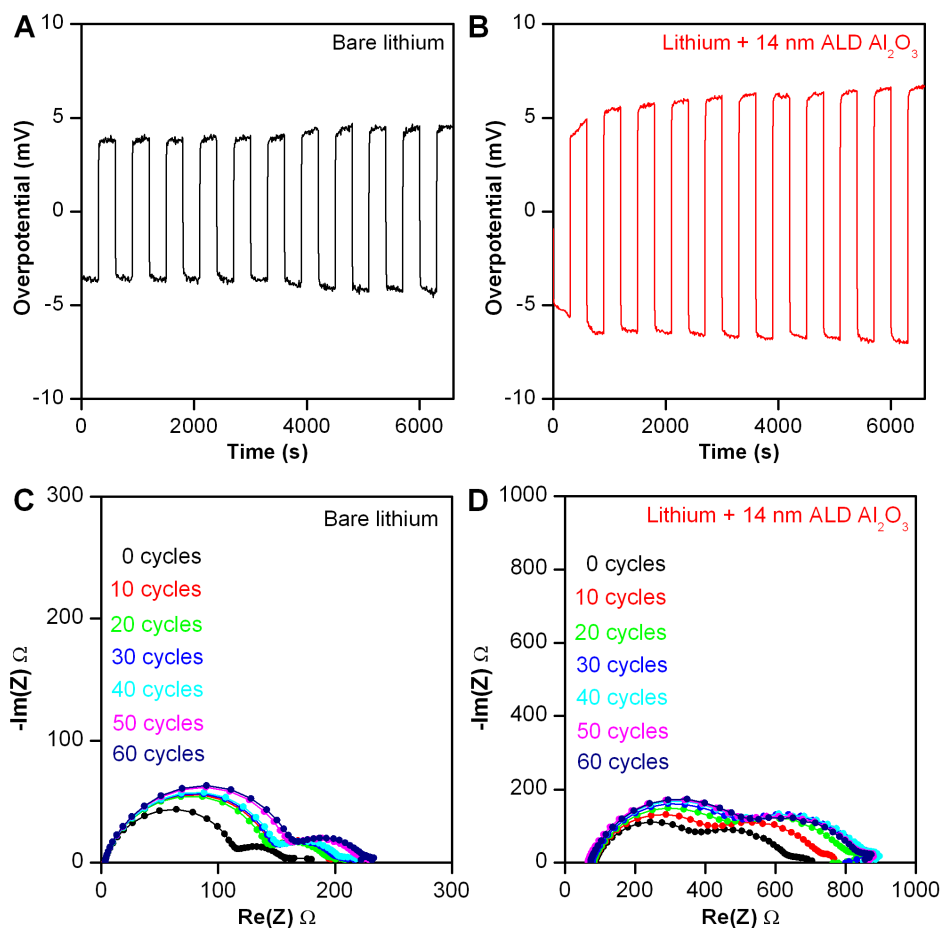


Figure 41. The first 10 GV cycles of symmetric coin cell with (a) two bare lithium metal current collectors and (b) two lithium metal electrodes protected with 14 nm ALD Al_2O_3 showing the overpotential evolution during lithium plating and stripping at 10 mAcm^{-2} . (c) EIS response (Nyquist plot) of the symmetric bare lithium metal coin cell before cycling and then subsequently after every 10 GV cycles. (d) Nyquist plot of the symmetric 14 nm ALD Al_2O_3 protected lithium metal coin cell before cycling and then subsequently after every 10 GV cycles.

This behavior is consistent with previously reported lithium plating studies, and in fact we find the influence of the thin ALD Al_2O_3 on the EIS response is similar to the recently published effect of aging the battery in the electrolyte before cycling.¹⁴⁷

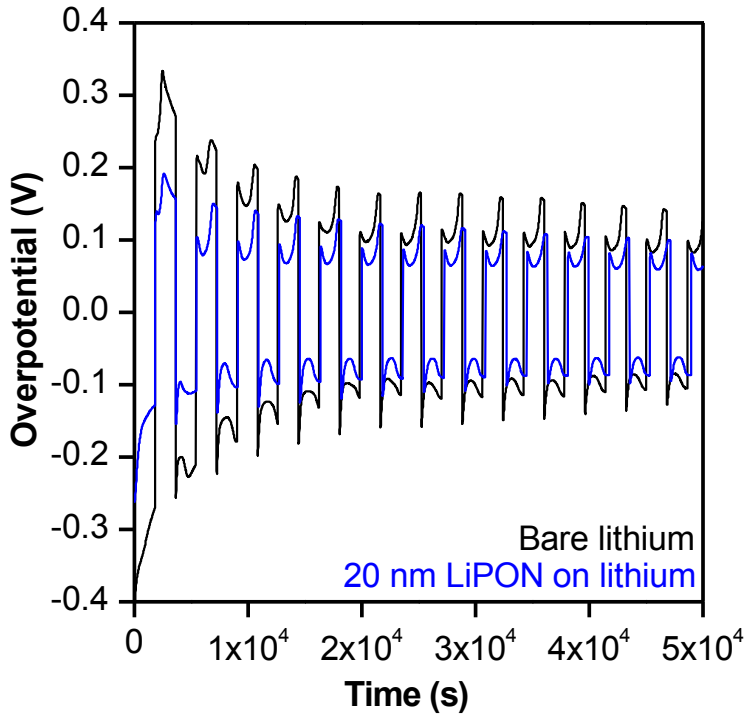


Figure 42. Overpotential trace of bare Li metal vs. 20 nm ALD LiPON protected Li metal at $2\text{mA}/\text{cm}^2$ current density, above the threshold for Li dendrite formation.

case of a metal anode.

Lithium Sulfur Battery Testing

CR2032 Li-S coin cells were assembled with activated carbon cloth (ACC)/sulfur composite cathodes, a previously demonstrated Li-S system with adequate behavior suitable as a proof of concept platform to test the efficacy of the ALD anode passivation procedure.¹⁴⁸⁻¹⁵⁰ Li-S battery cathodes were fabricated by impregnation of commercial activated carbon cloth (ACC) with sulfur under rough vacuum (10^{-3} Torr) at 150°C until the desired loading amount of S was obtained, typically ~ 12 hours impregnation for a total loading amount of 35% S.

It is important to note that the increase in impedance of a full cell will be half the impedance presented in Figure 40, as both sides of our symmetric cell are protected with identical 14 nm thick ALD Al_2O_3 layers. In a full Li-S device, slow Li^+ kinetics of the sulfur-based cathode will dominate the cell impedance, especially in the

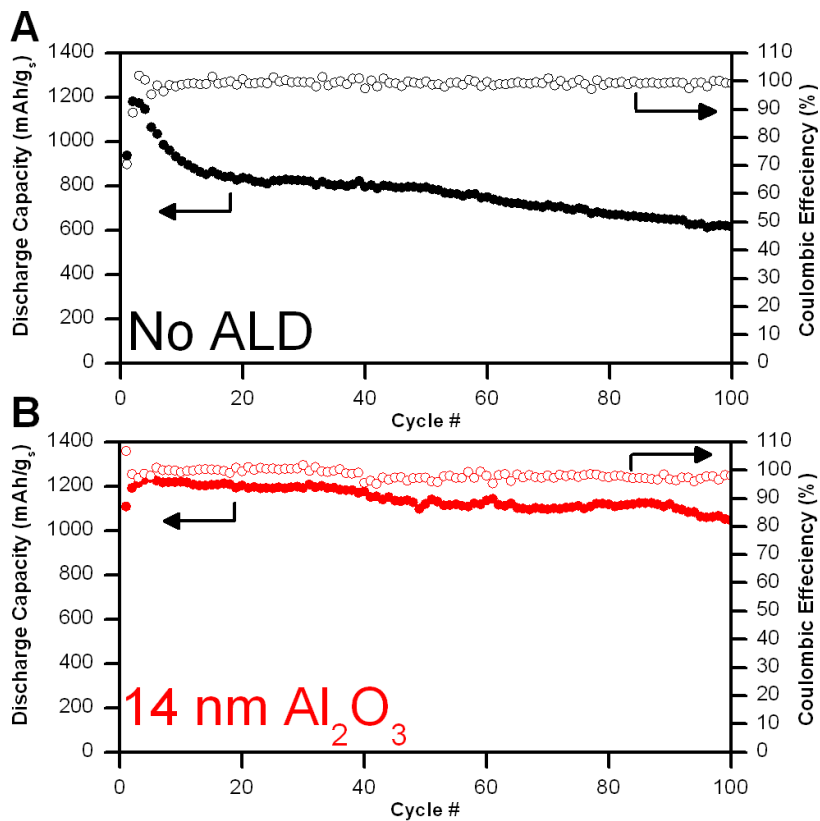


Figure 43. Discharge capacity (solid circles, left axis) and Coulombic efficiency (open circles, right axis) of both (a) bare Li metal anode and (b) anode protected with 14 nm ALD Al_2O_3 Li-S cells.

The long term cycling performance of these cells is shown in Figure 43. In the case of the bare Li anode, the lowered capacity of the 1st cycle strongly suggests a self-discharge mechanism similar to that suggested by Cairns *et. al.*,¹⁵¹ an often

downplayed phenomenon in work focusing on Li-S cathode performance. This self-discharge mechanism reduces dissolved sulfur species to polysulfides on the anode surface even before the start of cycling, proceeding as a self-propagating reaction since the medium chain polysulfides can shuttle back to the cathode and reduce sulfur to long chain polysulfide. This phenomenon will result in an initial decrease in cell capacity in the 1st cycle, and as available sulfur is consumed at the anode upon cycling it will reduce the capacity even further^{82,150}. In our case reactions at the surface of the bare Li metal

anode reduce the cell capacity from $\sim 1200 \text{ mAhg}^{-1}$ to $\sim 800 \text{ mAhg}^{-1}$ after the first 10 cycles, shown in Figure 43A.

Protection of the Li metal with ALD Al_2O_3 not only prevents this self-discharge during the rest period before we begin electrochemical cycling, but also prevents the capacity loss during the first 10 cycles, with the capacity of cells using ALD protected anodes falling a negligible amount from $\sim 1200 \text{ mAhg}^{-1}$ as shown in Figure 43B. This is reinforced by the Coulombic efficiency (CE) of the first two cycles being $>95\%$ in the case of the ALD protected Li and the CE of the first two cycles being 70% and 88% respectively for the bare Li. However, as we are using an excess of Li in our cells, the C.E. may in this case be less relevant metric as C.E. is normally associated with cathode degradation.

After 100 cycles, Li-S cells with bare Li metal anodes have lost nearly 50% of their initial capacity, while those with ALD protected Li metal anodes have lost only $\sim 10\%$ of their initial capacity and maintain a gravimetric capacity 60% higher than those with unprotected Li metal anodes. Clearly, the ALD Al_2O_3 protection layer increased both initial and long-term capacity of the cell *via* improved utilization of the sulfur by preventing Li metal anode corrosion and thus enabled cycling with enhanced capacity for up to 100 charge-discharge cycles.

Li-S batteries fabricated with considerably more S (4 mg/cm^2) were also cycled under similar conditions at an approximate rate of C/20. These cells were only able to be cycled 35 times

After 100 cycles, Li-S cells with bare Li metal anodes have lost nearly 50% of their initial capacity, while those with ALD protected Li metal anodes have lost only ~10% of their initial capacity and maintain a gravimetric capacity 60% higher than those with unprotected Li metal anodes.

To investigate the extreme situation of sulfur corrosion behavior of the anodes, we cycled Li-S coin cells with $\sim 5 \text{ mgcm}^{-2}$ sulfur and no addition of LiNO_3 for 100 charge-discharge cycles with bare, 14 nm ALD Al_2O_3 , and 14 nm ALD LiPON protected anodes, the data from which shown in Figure 45. Higher loading amounts of sulfur in the cathode lead to a higher concentration of dissolved polysulfide species in the electrolyte, eventually leading to significantly worse metal anode corrosion and lowered total Li-S cell capacity.

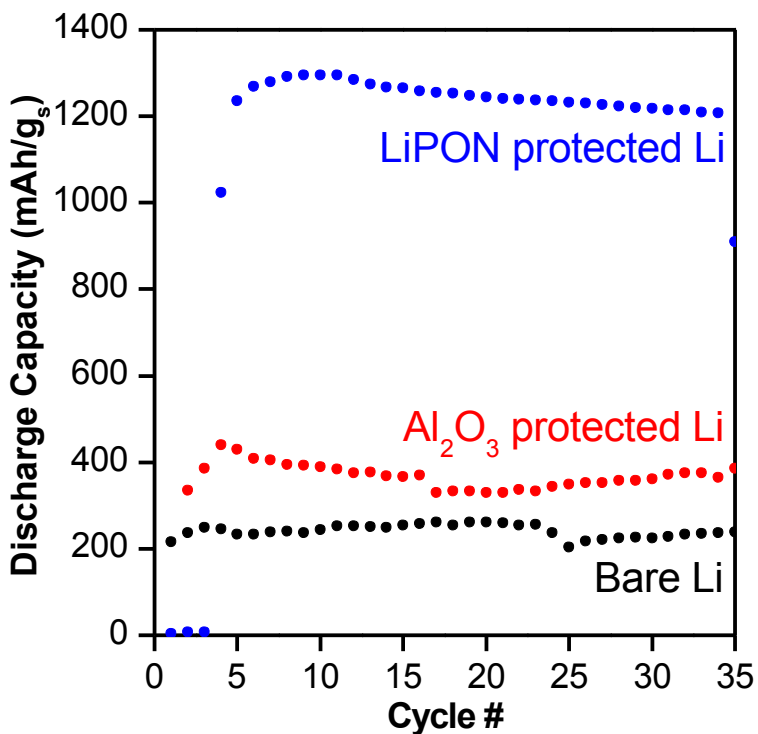


Figure 44. Performance of batteries assembled with (black) bare, (red) 14 nm ALD Al₂O₃ coated, and (blue) 14 nm ALD LiPON coated anodes cycled at 45 mA/g sulfur, corresponding to a cycling rate of approximately C/24.

After 100 cycles, Li-S cells with bare Li metal anodes have lost nearly 50% of their initial capacity, while those with ALD protected Li metal anodes have lost only ~10% of their initial capacity and maintain a gravimetric capacity 60% higher than those with unprotected Li metal anodes.

We disassembled these cells in our glovebox, then washed with DME to remove excess dried salt, and transferred it to our XPS without subsequent air exposure.

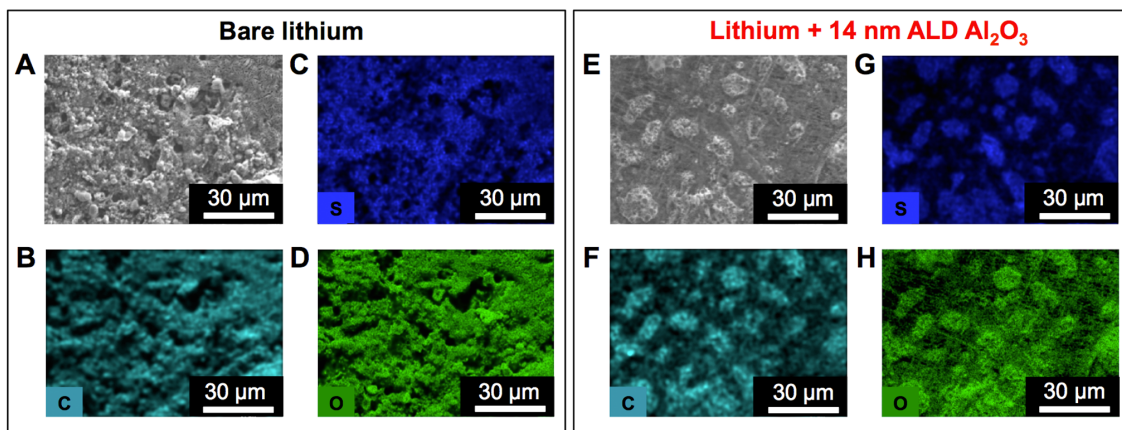


Figure 45. (a) SEM and; (b, c, d) EDX maps of bare Li metal anode after 100 charge-discharge cycles in a Li-S cell; (e) SEM and; (f, g, h) EDX maps of 14 nm ALD Al_2O_3 protected Li metal anode after 100 charge-discharge cycles in a Li-S cell.

EDX images obtained of the Li surface after cycling, shown in Figure 45, show that the density of the sulfur, carbon, and oxygen particulates is significantly lower on the surface of the ALD protected anode than on the unprotected anode. Although we don't thoroughly address the morphology of these deposits, their composition and growth conditions suggest hindered dendrite formation on the protected anode surface upon cycling. Due to the low EDX signal from the Al, we are unable to make any conclusions about the state of the ALD film, and thus do not include it here.

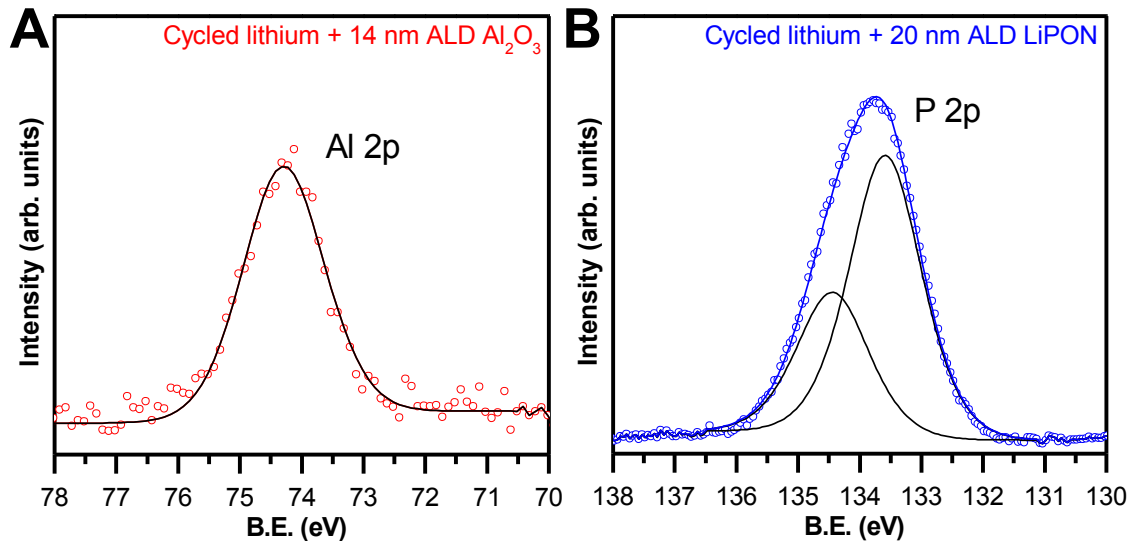


Figure 46. Hi resolution XPS spectra of (a) Li metal protected with 14 nm ALD Al_2O_3 ; (b) Li metal protected with 20 nm ALD LiPON after 100 charge-discharge cycles. Both XPS peaks contain best fits to the data.

Furthermore, XPS analysis of both the Al_2O_3 protected and the LiPON protected Li metal anodes after cycling, shown in Figure 46A and Figure 46B respectively, indicates that both the Al_2O_3 and LiPON remain on the surface of the Li metal after cycling. This is attributed to reduced reactivity of solvent at the protected metal anode interface *via* prevention of electron transfer from the Li metal to the electrolyte, in general agreement with prior theoretical predictions.^{152,153} This will prevent SEI formation on the protected areas of the electrode, and indeed the existence of XPS peaks associated with the ALD protection layers indicates that the SEI is less than ~8 nm thick on top of the protected areas of the electrode.

Lithium Dendrite Prevention via Self-Healing Protection Layers

Figure 47 shows SEM images of both bare and LiPON protected anodes are shown after being assembled into symmetric CR2032 coin cells using 1M LiPF₆ in 1:1 EC:DEC

electrolyte. These coin cells were subjected to 100 30-minute charge-discharge cycles at varying current densities both below ($500 \mu\text{A}/\text{cm}^2$), at ($1 \text{ mA}/\text{cm}^2$), and above ($2 \text{ mA}/\text{cm}^2$) the threshold current density for dendrite formation.¹⁴⁷

From these images, it is clear that at cycling rates below, and even at the current density required to form Li dendrites, the unprotected metal anodes form an uneven pitted surface morphology resulting from SEI formation. At $2 \text{ mA}/\text{cm}^2$, above the current density required for dendrite formation, Li dendrites are clearly seen forming on the surface of the Li anode, shown in Figure 47D.

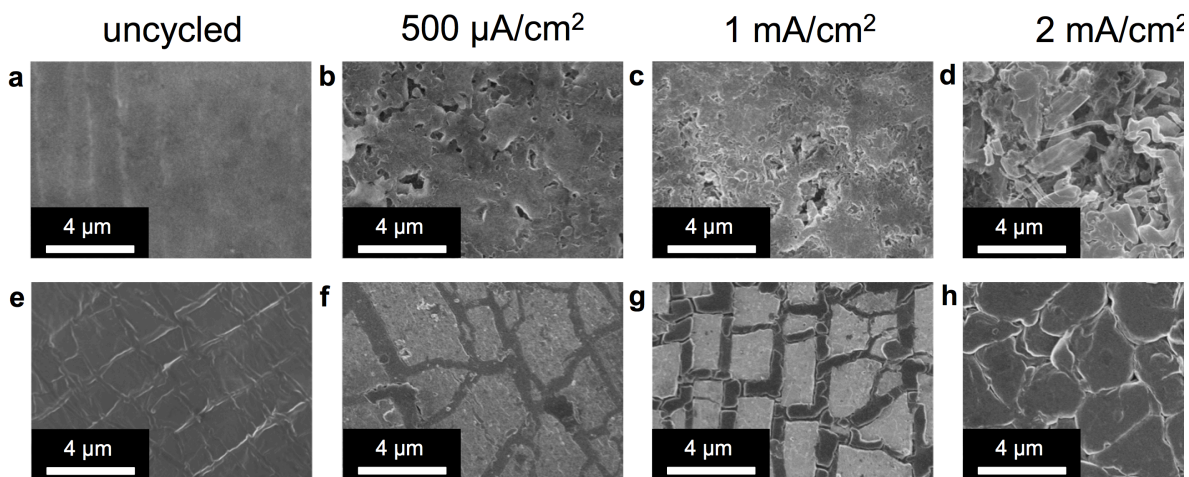


Figure 47. SEM images of (a) bare uncycled and (b-d) bare Li metal cycled at increasing current densities. Note the Li dendrite formation in (d). (e) As-deposited ALD LiPON on Li, showing cracks associated with the differing coefficient of thermal expansion between LiPON and Li metal. (f-g) cycled LiPON protected anodes at increasing current densities.

As for the ALD LiPON protected metal anodes, it is clear that the ALD protection layers crack and break during coin cell assembly, likely due to compression of the Li metal anode when crimping the coin cells. While most would consider cracks in protection layers an absolute failure of the protection layer, we instead find that these

cracks may actually be an ideal attribute of the ALD protection layer that help to stabilize the anode surface via a self-healing mechanism.

As the protected metal anodes are cycled, the Li metal is preferentially plated and stripped through the cracks in the ALD layer, which are the highest conductivity pathway for Li transport. At low cycling rates, minimal SEI formation occurs on the anode surface due to the chemical stability of the LiPON layer against the organic electrolyte, and so the surface of the anode is maintained in a stable state.

At higher cycling rates, electrolyte breakdown, and thus SEI formation is amplified, and the beginnings of SEI formation in the cracks can clearly be seen in Figure 47G. At current densities above those required for dendrite formation, there is significant formation of SEI at the cracks between the solid electrolyte plates. The ALD LiPON plates “float” on the surface of the metal anode, channeling Li transport through the cracks and localizing SEI formation at the cracks.

As this SEI grows and increases in impedance, this Li transport pathway is extinguished. However, due to the stability of the uncracked LiPON plates that remain on the anode surface SEI formation is prevented on the LiPON surface. As the LiPON has a relatively high ionic conductivity, Li transport is maintained through the protection layer, effectively acting as a “seesaw” self healing mechanism on the surface of the anode. As long as the surface area of the cracks can be balanced against the surface area of the remaining protected Li, this self-healing “seesaw” mechanism can prevent Li dendrite formation by extinguishing the Li conduction pathways through defects in the protection layers. This mechanism is shown in detail in the cartoon in Figure 48.

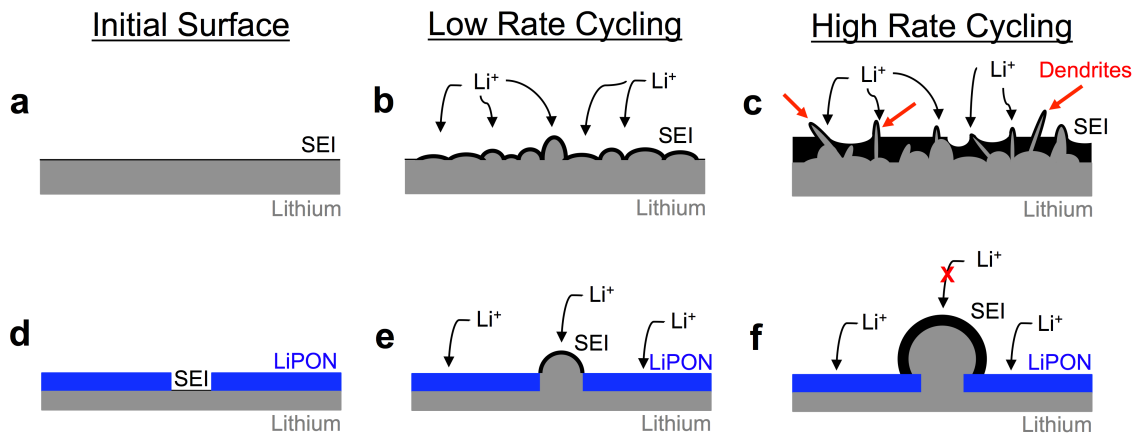


Figure 48. Cartoon demonstrating the proposed self-healing surface protection mechanism of ALD LiPON protected metal anodes. (a) Initial Li surface with spontaneously formed SEI layer. (b) Li surface after low rate cycling (c) Li surface after high rate cycling demonstrating dendrite formation. (d) As-deposited ALD LiPON protection layer directly on the Li metal. SEI only forms at the cracks in the LiPON film. (e) ALD LiPON protected Li metal at low rate cycling, showing concentrated Li plating and stripping. (f) ALD LiPON protected Li metal cycled at rates above the dendrite formation threshold, where the ionic conduction pathways through the cracks in the LiPON are extinguished due to excess SEI formation.

Together, this mechanism indicates that perfect protection layers for Li metal are likely unnecessary, provided that the ionic conductivity of the protection layer is great enough to allow Li transport upon insulating SEI formation at the cracks. As long as the surface area of the cracks can be balanced against the surface area of the remaining protected Li, this self-healing “seesaw” mechanism can prevent Li dendrite formation by extinguishing the Li conduction pathways through defects in the protection layers.

Chapter Summary and Conclusions

ALD coatings applied directly to Li metal foil could be integrated into the battery fabrication process, particularly given recent advances in atmospheric pressure and low temperature roll-to-roll ALD tooling.¹⁵⁴ Protecting Li anodes in this way could potentially enable relaxed environmental controls during Li foil manufacture and battery

assembly in dry rooms, thus reducing costly overhead during battery materials manufacture.

In this chapter, a novel proof-of-principle methodology for protection of metallic lithium anodes by application of ALD coatings directly on Li metal has been demonstrated. These coatings serve as effective protection barriers against Li metal corrosion upon air, sulfur and organic solvent exposure. Furthermore, it is demonstrated that Li metal protected with only 14 nm ALD Al_2O_3 can drastically reduce first cycle capacity loss in the Li-S system due to prevention of anode corrosion in the presence of sulfur species in the electrolyte, and maintain a 60% increased gravimetric capacity after 100 cycles. 20 nm of higher conductivity ALD LiPON coatings can increase the gravimetric capacity by up to 6X for at least 35 cycles over unprotected anodes, and it is expected that this capacity improvement could be maintained for significantly longer cycling.

These thin ALD coatings do crack upon cycling, and indeed this may be beneficial to operation of the battery via a self-healing mechanism that can prevent Li dendrite formation at high operational currents.

Together, these results clearly demonstrate that ALD is an effective method for protecting Li metal anodes. The demonstration of this proof of concept metal anode protection using ALD Al_2O_3 has recently been published in ACS Nano.¹⁵⁵ However, research into this idea will continue, as the versatility of known ALD chemistries provides further options for the composition and functionality of the protection layers; of particular interest are flexible hybrid organic-ceramic electrolytes. Finally, it seems

likely that corresponding benefits can be accessed for other reactive metal anode systems beyond lithium, e.g., Na, Mg, and Al metal anodes as well, some of which will be investigated in the future.

Chapter VII: Solid 3D Battery Development

Motivation

Solid-state batteries are inherently significantly safer than their liquid electrolyte-based counterparts, and moving from conventional bulk electrodes to thin-film geometries can actually improve both the gravimetric and volumetric energy density by factors of 2-3.⁵⁰ The scope of this potential improvement is shown in Figure 49 in comparison to current Li-ion technology. This chart however doesn't even take into account the geometric capacity enhancement offered by moving from planar geometries to 3D structures, which can, in practice, enhance volumetric energy density by up to an incredible 100X, and possibly more.^{26,48}

However, current physical vapor deposition techniques suitable for fabrication of thin-film solid-state batteries cannot adequately fabricate high-aspect ratio structures with the required uniformity and film quality as is necessary for high-performance 3D devices.^{37,49,156,157} These techniques can fabricate single nanoscale model batteries for study, however fabrication of uniform large arrays of 3D batteries is currently unachievable.^{47,158}

Finally, use of heavy scaffold materials (including the silicon nanopillars commonly used) limits the improvements possible from gravimetric energy density improvement, and in fact at some as-yet to be determined point the mass gains of increasing the aspect ratio of the scaffold will negate those offered by volumetric energy density improvements due to aspect ratio enhancement.

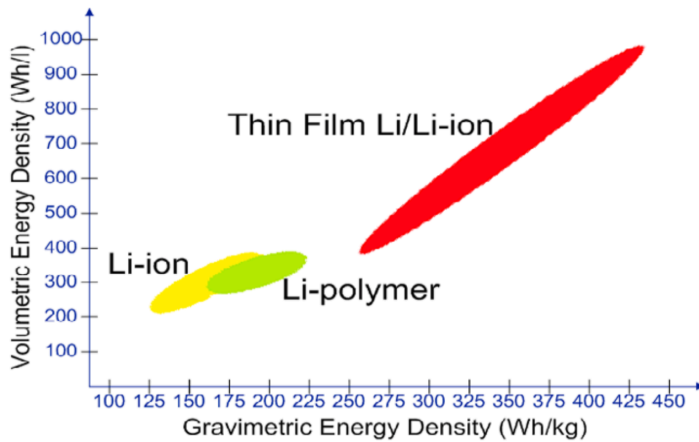


Figure 49. Volumetric and gravimetric energy density increases possible by moving from conventional Li-ion batteries to solid-state planar thin film Li batteries.⁵⁰

The ultimate success of this project would be realized by development and fabrication of an optimized high aspect-ratio lithium battery architecture using ALD processing for all layers of active materials in the device, research that is

currently ongoing in the Rubloff group and will be continued by other graduate students in the future. This 3D solid-state lithium-ion battery would have a number of advantages over current lithium-ion battery technology. Improved cell safety and an increased operational temperature window could be realized due to replacement of the organic electrolyte with a solid-state alternative. Also, removal of this organic electrolyte could drastically reduce total device weight due to elimination of superfluous active material. Lastly, fabrication of the entire battery is simplified by only using one deposition technique, and with recent advances in roll-to-roll ALD manufacturing¹⁵⁴ it is conceivable that that this proposed architecture could be scaled up for future commercialization.

ALD Solid Battery Fabrication Strategy

Generally, fabrication of a 2D planar solid-state battery is significantly easier than fabrication of the same battery on a 3D template using non-ALD deposition techniques,

as the planar substrate is much more forgiving to inhomogeneities in the deposition and patterning processes. Device characterization is also significantly easier in the planar geometry, so planar devices will simplify materials optimization by enabling surface analysis methods such as AFM, XPS, and spectroscopic ellipsometry. Indeed, most of the previous work on solid-state thin film batteries has been on planar geometries due to the limitations of the deposition procedures used, facilitating comparisons among different competing devices.

However, when using ALD processes for the entire battery stack, planar and 3D devices can be fabricated and tested concurrently. As both 2D and 3D devices are fabricated using the same materials and process steps, the only difference is the substrate geometry. As ALD deposition is to an extent geometry independent (certainly in the case of the substrate geometries used in this thesis), deposited film morphology and parameters are expected to be near identical in the case of the 2D and the 3D thin film batteries. This massive overlap in processing allows concurrent device fabrication, but then allows possible destructive characterization of the 2D devices while minimizing possible damage to the 3D devices from characterization and sample handling. However, due to limitations of sample transfer in our integrated system in the ANSLab, only two 2D and two 3D substrates can be processed in parallel, limiting concurrent fabrication to two devices each. The devices discussed below should serve as proof of concept devices, as this work is only in preliminary stages, and do not represent the ideal or optimized devices.

2D Device Fabrication

For the last section of this thesis, planar battery structures were to be fabricated in order to demonstrate a working solid-state electrochemical device using an ALD LiPON electrolyte. A planar device simplifies materials characterization by enabling surface analysis methods such as AFM and XPS, and is significantly simpler than constructing 3D solid electrochemical devices. The planar device will be used to determine the fundamental scaling limits of the ALD solid electrolyte by fabricating devices with varied electrolyte thickness to determine at what point the device ceases to function, which, based on the ionic conductivity measurements of ALD LiPON films should be close to 20 nm.

This first attempt at fabrication and testing of a 2D planar battery device was done using an Au bottom contact, a cathode of 75 nm ALD V_2O_5 (unlithiated), a 140 nm ALD LiPON electrolyte layer, and an anode of 150 nm Au. The first two I-V scans of this device from -7V to 7V are shown in Figure 50.

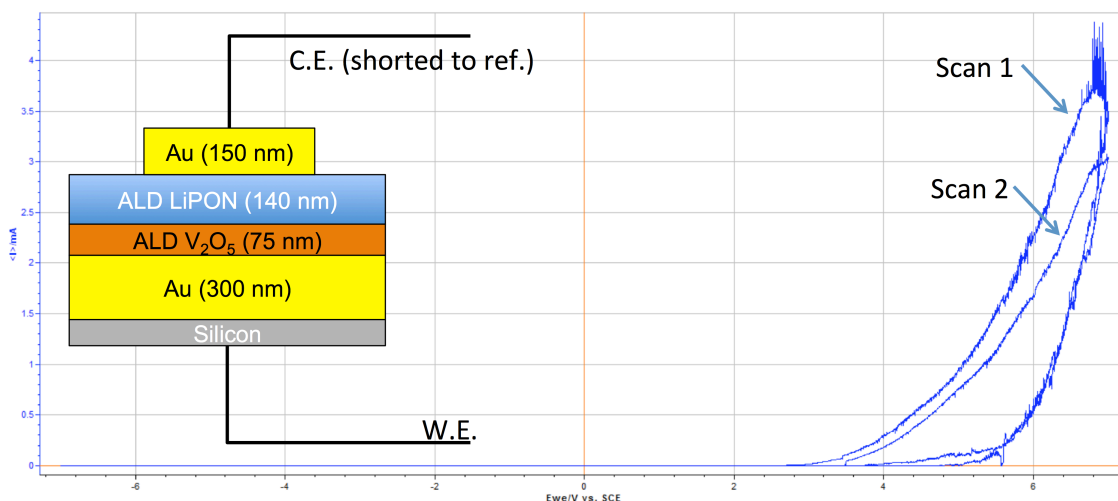


Figure 50. First two I - V measurements of a V_2O_5 -LiPON-Au solid battery stack from $-7V$ to $7V$. Inset: Cartoon of the MIM device stack measured.

Previous reports have suggested that ALD V_2O_5 is lithiated during the ALD process of a Li-containing top layer, however this appears not to be the case for this device. At low potentials of as high a magnitude as $-7V$, there is no current, indicating that ALD LiPON is stable, but with a large potential barrier to lithiation of the ALD V_2O_5 . At potential biases $> 2.5 V$ during the positive potential sweep, there is a large peak associated with breakdown of the ALD LiPON at the Au-LiPON interface, resulting in lithiation of the Au anode (confirmed by XPS, but not shown). However, as the ALD V_2O_5 cathode is unlithiated to begin with, this Li must come from breakdown and delithiation of the ALD LiPON. Indeed, as there is no negative current during the reverse potential sweep, this peak is indicative of a breakdown mechanism in the LiPON, and not of a reversible Li insertion into the Au anode.

Additional devices must be fabricated in order to demonstrate a fully functional device, and this work is currently ongoing. An upgrade of the precursor delivery manifold of the *Ultratech* Fiji F-200 ALD system was recently completed, allowing

addition of two additional liquid precursors. This manifold upgrade will allow deposition of pre-lithiated V_2O_5 cathodes by combining the Li_2O and V_2O_5 ALD processes, resulting in a pre-lithiated cathode for the solid battery. A precursor for deposition of TiO_2 will also be added to this ALD tool, allowing deposition of an amorphous TiO_2 anode, which should enable fabrication of a solid-state battery with 1.5 V.

3D Device Fabrication

In parallel to the planar 2D devices, 3D solid-state batteries were also fabricated. Originally, a nanocone templated developed in collaboration with Alec Talin from NIST was used as a 3D substrate, however due to capability deflation these substrates became unavailable after the first (non-operational) device fabrication.

Nanocone Template

The first attempts at fabricating a 3D device were done in collaboration with Alec Talin at NIST. Talin's group fabricated silicon nanocone templates using nanoimprint lithography, and supplied these substrates for use. However, upon graduation of Alec Talin's postdoc, these substrates were no longer available, so alternative substrates were pursued instead. I was able to fabricate one fully solid-state ALD battery onto the nanocone substrate, however this device was shorted and did not function. FIB X-sections of the fully solid battery were collected to investigate the morphology and quality of the active material layers.

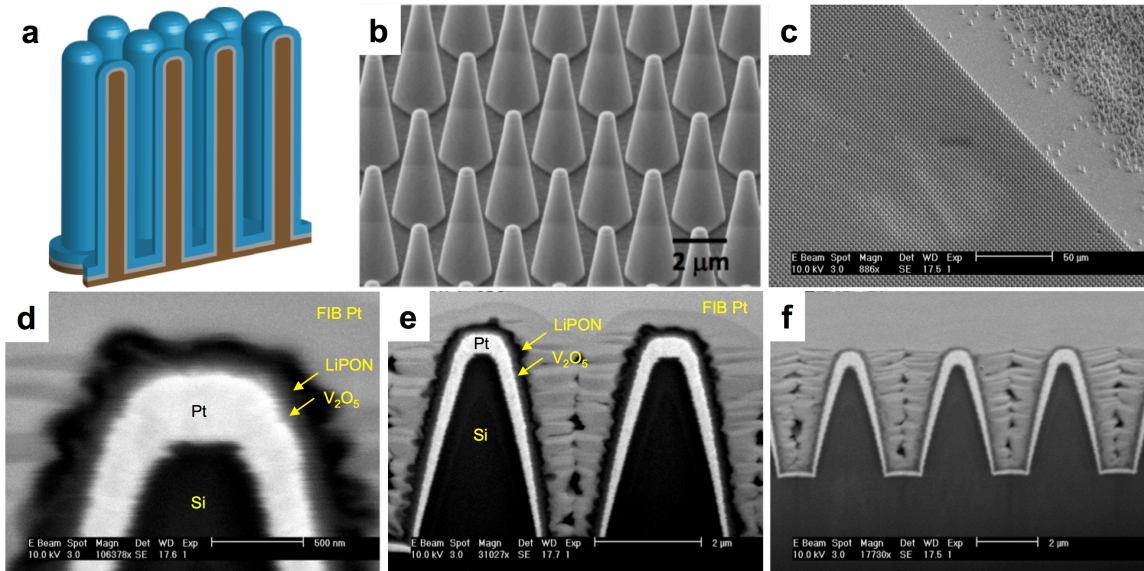


Figure 51. (a) Cartoon showing fabricated ALD solid battery structure. (b) Silicon micropillars fabricated using nanoimprint lithography. (c) Low resolution SEM image of silicon micropillars after sputtering a Pt current collector, cathode of 100 nm ALD V_2O_5 , and electrolyte of 140 nm ALD LiPON. (d-f) FIB x-sections of fabricated ALD 3D solid-state batteries deposited onto silicon micropillar substrates at increasing magnifications.

Lightsmyth Diffraction Grating Template

In-house fabrication of 3D micropillar substrates for 3D batteries is complicated, expensive, and time consuming. To improve throughput and save time, In the future the project will switch to commercial silicon diffraction gratings from Lightsmyth. These gratings cost on the order of \$150/ substrate, and can be ordered with specific dimensions suitable for nanobattery fabrication. We will use two different substrate geometries: 2D nanopillars arrays and 1D nanoline arrays. Three SEM Images of both the 2D and 1D gratings with ideal spacing are shown in Figure 52. Battery materials will be fabricated on top of both of these substrate geometries in parallel so that the 2D substrate can be used for device testing using a nanoprobe, while the 1D substrate can be used for cross-sectional imaging of the solid battery stack.

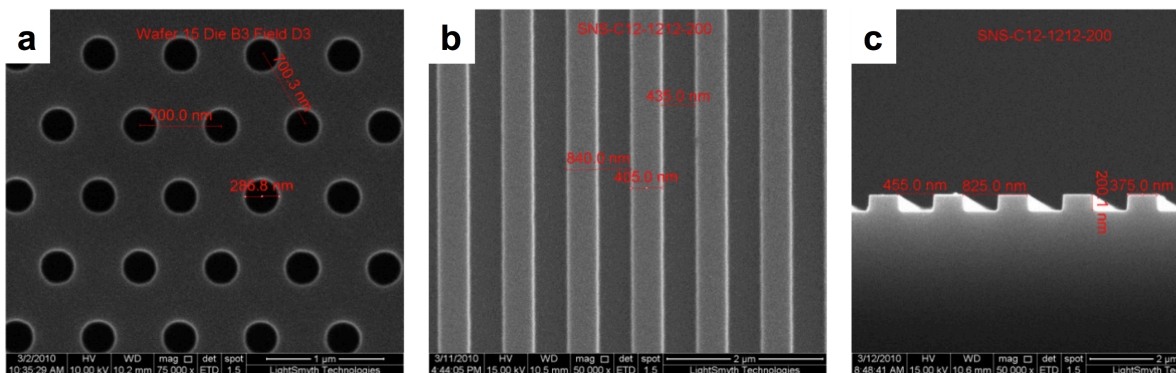


Figure 52. SEM images of commercial Lightsmyth gratings. (a) 2D nanopillar template, (b) 1D nanoline template, (c) side profile of 1D nanoline template. Images from <http://www.lightsmyth.com>.

These commercial gratings will also serve as nanoimprint lithography templates for future synthesis of nanostructured 3D battery templates.

Future Outlook for ALD Solid State Batteries

While the initial proposed outcome of this thesis was development of a solid-state 3D battery fabricated entirely by ALD, constructing such a device has proven to be significantly more challenging than initially anticipated. As such, while prototype 3D batteries have been fabricated using ALD materials for all the active layers, a working prototype has yet to be demonstrated for either a full ALD planar or a full ALD 3D battery due to unanticipated process integration challenges resulting in device shorting. While significant work has already been accomplished towards realizing the ultimate goal of a working all ALD 3D solid battery prototype, further optimization of materials deposition processes, process integration strategies, and tools for device characterization are necessary.

To facilitate prospects for an optimized, commercially competitive device, significant effort should be expended to replace the substrate with an alternative to silicon. Silicon is

ideal from a processing perspective, but likely is too expensive for future commercialization. Also, due to the potential issues associated with lithiation of the silicon substrate and the low electronic conductivity of silicon, both diffusion barriers and current collector layers are necessary, complicating device fabrication. Ideally, substrates would be replaced by a cheap, light, and multifunctional scaffold material that provides both mechanical stability and electronic conductivity, eliminating the need for deposition of a current collector layer. Two of the best alternatives are carbon-based: MWCNT sponges and carbonized wood fibers. An example 3D ALD solid-state battery fabrication sequence on a MWCNT substrate is shown in Figure 53.

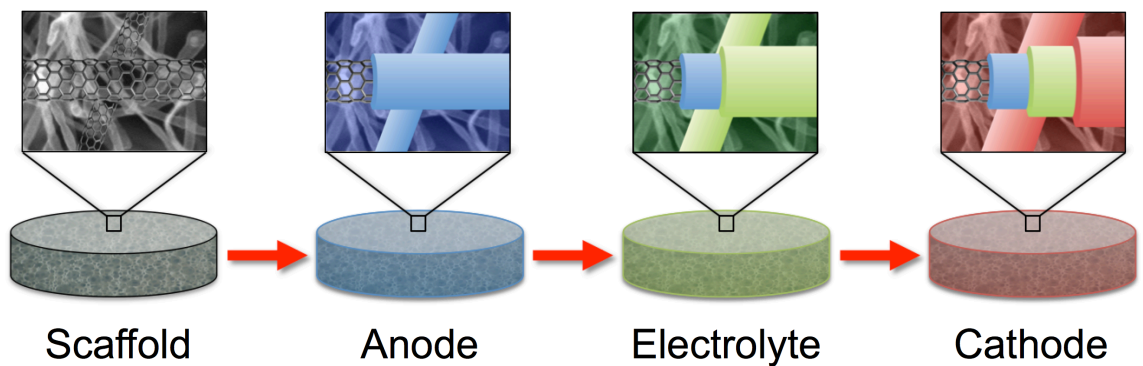


Figure 53. Cartoon representation of an ideal solid battery fabrication sequence utilizing atomic layer deposition onto a nanostructured substrate, in this case a MWCNT sponge.

Both of these carbon-based materials are relatively cheap to produce, environmentally friendly, light weight, high porosity, and electronically conductive, and represent an ideal future direction for continued device architecture development.

Thesis Summary and Professional Output

This thesis not only summarizes my professional body of work, it also expands upon those publications with additional data and analysis, as well as a comprehensive discussion about implications and continuing future research that has stemmed from this work. I have conducted original research to develop ALD processes for the solid electrolyte LiPON, characterized the performance and properties of LiPON and its constituent components, and investigated the application of ALD materials for two applications: metal anode protection for beyond Li-ion batteries and for fabrication of solid-state 3D microbatteries.

A fire in the LAMP lab at UMD in January 2012 set me back over two years research-wise, but in the end I believe this setback has made me significantly stronger as a scientist. From 2012 to the end of 2013, Instead of achieving research output, I spent my time designing and building a new facility, now the ANSLab. ANSLab started from an empty room without electricity or ventilation, and now is a world-class surface science laboratory for the fabrication and testing of ALD heterostructured devices for electrochemical energy storage. However, this facility is not limited to current research topics, and hopefully in the future other students will expand upon the instrumentation and lab capabilities to develop new and exciting avenues of research.

Experimentally, during the course of my time at University of Maryland I first developed the binary ALD process for $\text{Li}_2\text{O}/\text{LiOH}$, and investigated the process kinetics of this pseudo-ALD process. Next, via stepwise precursor addition, I added two additional precursors to fabricate the quaternary ALD process for LiPON. I have

demonstrated the utility of using ALD solid electrolyte protection layers directly on Li metal anodes for beyond Li-ion batteries, and have started work towards the development of an all ALD 3D solid-state heterostructured battery. While this work is incomplete, I expect development and demonstration of ALD LiPON to have a significant impact on the advanced battery fabrication community, as it will enable future successful fabrication of thin film, all solid-state 3D microbatteries, pushing the fundamental size limits of battery technology further towards the nanoscale.

During the course of this thesis, I have co-authored 7 published peer-reviewed works^{15,39,86,88,113,155,159}, and have co-authored 6 more publications submitted in various stages of the peer-review process. I have applied for a provisional patent application for “Metal Anode Protection with Atomic Layer Deposition,” and am in the process of finalizing the patent.

In the future, I expect an expansion of this research both to further investigate the chemistry and effectiveness of ALD films as protection layers for metal anodes in the Li-S, Li-O₂, and Li-NMC battery systems. Another Ph.D. student will continue this research in the future. I also expect continuing research to optimize architectures, process integration, and testing for all ALD 3D solid-state batteries, with the hope that in the near future architectural and process integration challenges will be addressed and a fully working 3D solid-state ALD battery will be realized.

Appendix: Experimental Parameters

This appendix describes in detail all the experimental parameters for the methods used in this thesis, as well as descriptions of the tools used.

Atomic Layer Deposition

ALD materials discussed in this thesis were deposited in an *Ultratech* Fiji F-200 ALD reactor, which was customized for direct coupling to a UHV transfer system.

ALD Li_2O and LiOH films were deposited in Mario from 225°C-300°C, using precursors lithium tert-butoxide (LiO^tBu) (*Aldrich*, 99.7%), de-ionized H_2O , and O_2 gas (*Praxair*, grade 4.3). Argon (*Airgas*, grade 5.0) was used as a carrier gas during deposition. The base pressure of the ALD reactor was $< 2 \times 10^{-6}$ Torr and a process pressure of 200 mTorr was maintained via Ar gas flow. The LiO^tBu precursor was kept at 165°C, and was delivered to the ALD chamber using a bubbler with bypass line and 40 sccm Argon carrier gas flow. ALD films were deposited using precursor saturation doses (controlled by fast-acting ALD valves) of 3s for the LiO^tBu , .06s for the H_2O , and 4s for the TMP. For plasma-enhanced ALD, the plasma O_2 ($^{\text{P}}\text{O}_2$) was pulsed for 20s at a 40 sccm flow rate and a power of 300W. For deposition of Li_3PO_4 ALD films, trimethylphosphate (TMP) (*Aldrich*, 97%) was used and kept at a temperature of 70°C. Fabrication of ALD LiPON was accomplished by addition of a plasma N_2 dose in the Li_3PO_4 ALD process. The final ALD LiPON ALD process uses the following ALD

sequence: LiO^tBu (3s), purge (20s), H₂O (.06s), purge (20s), TMP (.4s), purge (20s), N₂ (10s), purge (20s).

Li metal (*Alpha Aesar*) was protected by application of ALD Al₂O₃ coatings at 150°C. Disks of Li were stamped from 750 μm thick (*Alpha Aesar*) lithium metal ribbon using a punch, and press the disks of Li onto stainless steel metal disks for handling. We then transferred the lithium metal to a *Cambridge Nanotech* Fiji F200 ALD tool also directly connected to the UHV transfer chamber. Precursors used for the ALD process were trimethylaluminum (TMA, *Aldrich*, 97%) and plasma O₂, and the reactor temperature was 150°C. The ALD process used a .06s/30s/10s/5s TMA pulse/purge/^PO₂ pulse/purge pulse sequence with a growth rate of 1.2 Å/cycle. Thickness of the deposited layer was determined by ellipsometric measurements of a blank Si wafer from the same ALD batch using a Cauchy optical model.



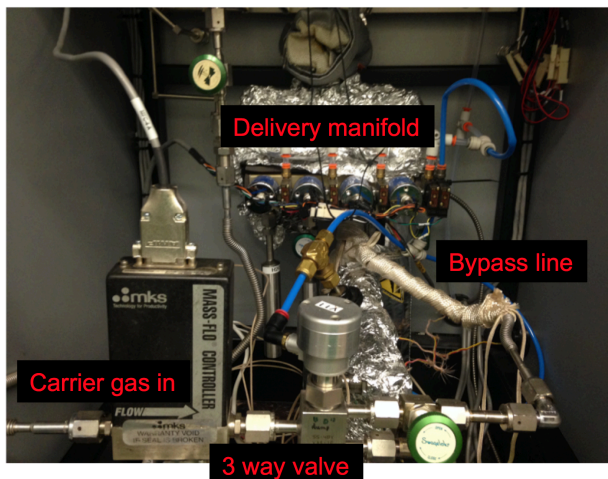


Figure 54. (left) Stock image of an Ultratech Fiji F200 ALD tool. (right) Bubbler-based delivery system constructed in “Mario” in order to deposit Li-containing chemistries.

Atomic Force Microscopy (AFM)

AFM is used to determine morphology, grain size, and roughness of ALD thin films. AFM measures deflection from a surface of a resonating nanoscale probe using laser interferometry to determine surface morphology with nanometer-scale resolution. AFM characterization was conducted using an *NT-MDT* NTEGRA Spectra system in tapping mode at a scan rate of 1 $\mu\text{m/s}$. Two sample stages were used: one for planar solid films used for morphology determination of ALD LiPON, and one stage for liquid samples suitable for study of Li metal in a solvent-based environment.

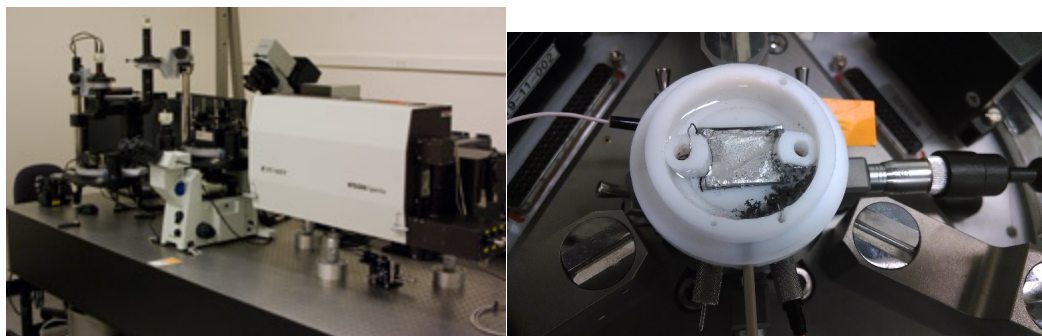


Figure 55. (left) Image of the NT-MDT NTEGRA Spectra tool in ANSLab. (right) Close-up image of the in-situ liquid AFM cell used during Li metal surface chemistry observations.

Battery Testing

CR2032 coin cells were tested using our anodes and ACC/S cathodes with 0.1 M LiTFSI in 1:1 DME:DOL with 1% LiNO₃ electrolyte. For extended cycling, we used Li-S cells loaded with 1.2 and 5 mgcm⁻² of sulfur, corresponding to a cell capacity of 1.4 and 4 mAhcm⁻². The cells were cycled at 0.14 and 0.31 mAcm⁻² between potential limits of 1.7 V and 2.6 V with a rest period of 60 hours before the start of cycling. No LiNO₃ was used in the sulfur cells for XPS characterization, and the cells were loaded with 5 mg of sulfur per coin cell. Electrochemical cycling was done using an *Arbin* potentiostat with constant current. CV and EIS measurements were carried out using a *Bio-Logic* VSP potentiostat in a three electrode tee-cell configuration with Li metal as both the reference and working electrodes. Batteries were assembled in our MBraun LabMaster glovebox using standard coin cell assembly procedures.

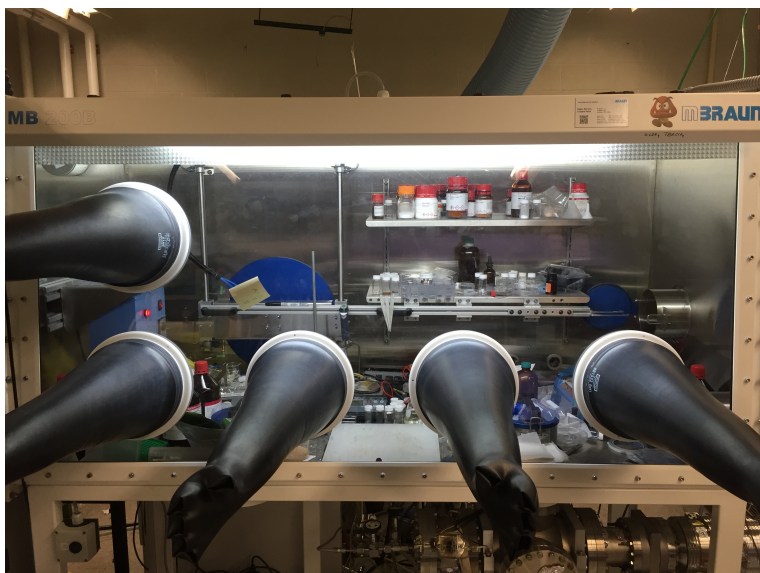


Figure 56. MBraun LabMaster glovebox in ANSLab where batteries were assembled and tested.

Optical Image Analysis

Samples were placed in a controlled laboratory atmosphere at 25°C and 40% R.H and imaged using an 8-megapixel *Apple* iPhone 5 camera from a fixed position under constant lighting conditions. We determined the degree of surface tarnishing using the open source software *ImageJ* to first convert the images to 8 bit black and white files, then to normalize the dynamic range of each pixel from 0 to 255 saturation, and finally to calculate the brightness of each pixel within the lithium metal surface area using binary pixel binning to categorize individual pixels as either non-tarnished or tarnished (0-127 or 128-255 saturation respectively).

X-Ray Diffraction (XRD)

XRD analysis was performed at on a shared *Bruker* D8 diffractometer in the UMD Chemistry XRD center using Cu K α x-rays (1.54 Å). Samples were scanned for ~1 hour

per sample depending on angles used. XRD peaks were compared and matched to the ICDD-2014 database for peak identification.

Transmission Electron Microscopy (TEM)

TEM imaging is used to obtain extremely high resolution pictures of ALD films deposited onto nanotubes, nanowires, and thin cross-sections of material deposited on planar substrates. When samples are thin enough (< 200 nm), high-energy electrons can be transmitted through the samples. Interaction of these electrons with the electrons present in the sample enables not only materials imaging, but also chemical identification and electron diffraction. For this work, a shared *JEM 2100 LaB6* TEM in the UMD NISPLab was used for nanostructure imaging.

Quadrupole Mass Spectroscopy (QMS)

For electrolyte decomposition experiments described in Chapter VI, samples were placed into sealed glass vials with 2 mL of 1M LiClO₄ in PC solution at 25°C. A *MKS Microvision2* differentially pumped quadrupole mass spectroscopy tool was used to sample the evolved gasses in the headspace of the sample containers. This tool is also capable of UHV operation by removal of the differentially pumped manifold.



Figure 57. MKS Microvision 2 quadrupole mass spec tool in ANSLab with control computer rack and screenshot of compound fragmentation software used to identify q/m peaks.

Electrochemistry

For electrochemical testing experiments a number of different experimental setups were used. For CV measurements, coated and uncoated Li in *Swagelok* T cells with .1M LiTFSI in 1:1 DME:DOL electrolyte using Li as both reference and working electrodes were used. Lithium was loaded into the T cell such that the metal was only placed into contact with electrolyte. CV and EIS measurements of the protected anode were done in a three electrode Tee-Cell configuration with Li as both reference and working electrode and a *Bio-Logic* VSP potentiostat. CV and EIS measurements of ALD films deposited directly on stainless steel blocking electrodes were also done in CR2032 coin cells using 1M LiPF₆ in 1:1 EC:DEC electrolyte. EIS spectra were collected from 100 kHz to 10 mHz at 20 mA AC bias potential. Lithium plating and stripping of ALD protected and unprotected Li metal electrodes was done using CR2032 coin cells using 1M LiPF₆ in 1:1 EC:DEC electrolyte.

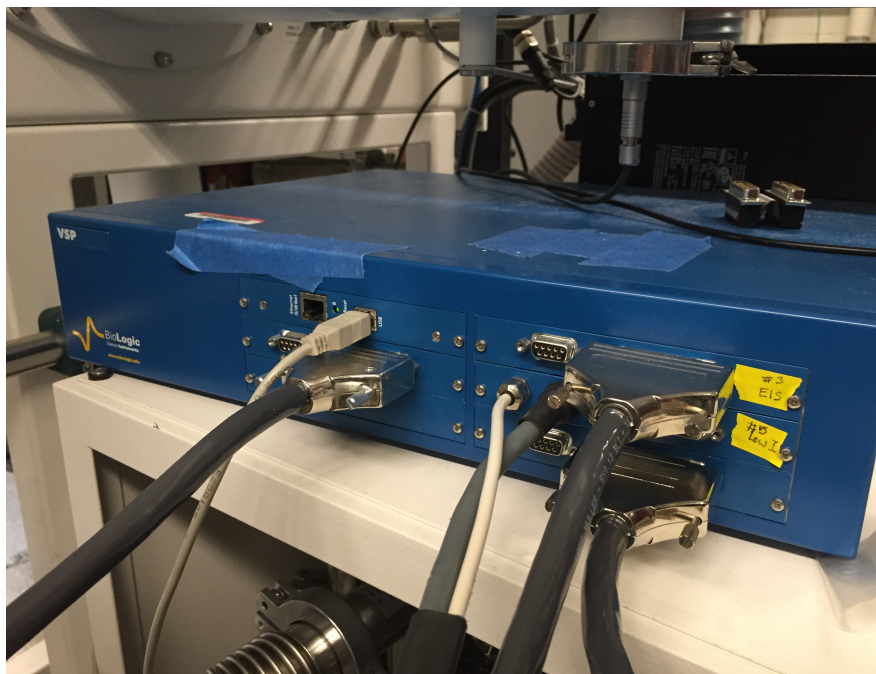


Figure 58. Bio-Logic VSP potentiostat used for CV, GV, EIS, and battery cycling measurements.

X-ray Photoelectron Spectroscopy

XPS was done in a *Kratos* Ultra DLD surface analysis system using a monochromated Al anode. Generally, ALD films were transferred directly from the deposition tool to the *Kratos Ultra DLD* XPS system under UHV conditions in under 3 minutes without air exposure. XPS survey spectra were collected using a monochromatic Al K α source in hybrid lens mode with 160 eV pass energy and 1 eV resolution, while high-resolution spectra were collected in hybrid lens mode with a 20 eV pass energy and 0.1 eV resolution.

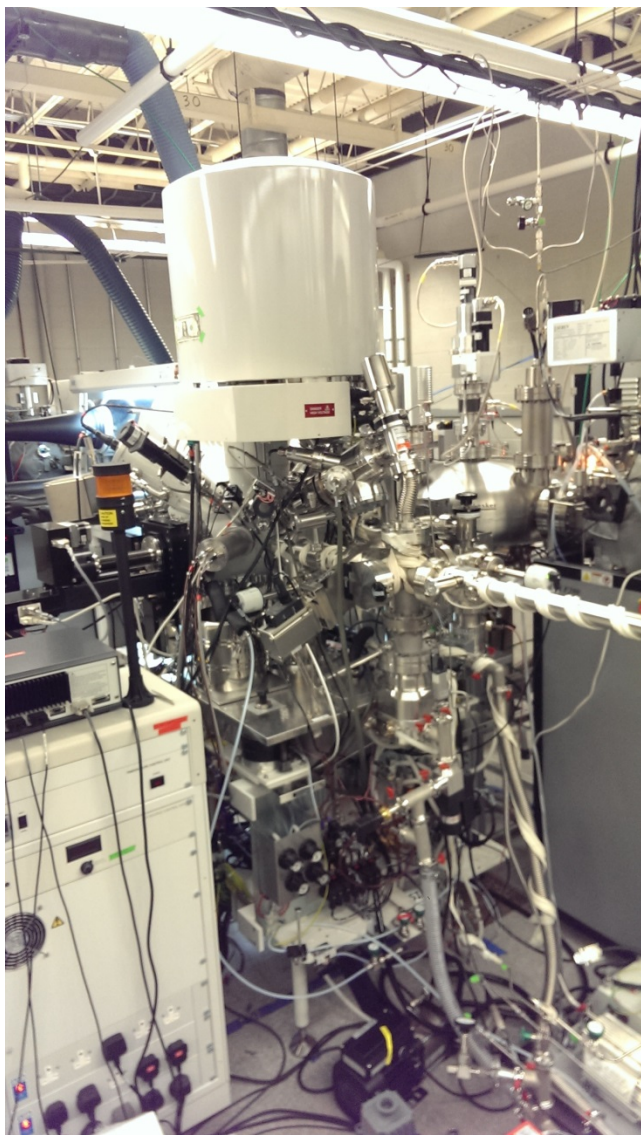


Figure 59. Kratos Ultra DLD surface analysis system in the ANSLab, primarily used for XPS measurements.

Spectroscopic Ellipsometer

We cycled coated and uncoated Li in *Swagelok* T cells with .1M LiTFSI in 1:1 DME:DOL electrolyte using Li as both reference and working electrodes. Lithium was loaded into the T cell such that the metal was only placed into contact with electrolyte. CV and EIS measurements of the protected anode were done in a three electrode Tee-Cell

configuration with Li as both reference and working electrode and a *Bio-Logic* VSP potentiostat.



Figure 60. J.A. Woollam M-2000D spectroscopic ellipsometer used for measuring optical properties of thin films. This image shows the ellipsometer on its base, however the source and detector can be mounted to the Ultratech Fiji F-200 ALD tool for in-situ sensing.

References

- (1) Shukla, A.; Kumar, T. Materials for Next-Generation Lithium Batteries. *Current Science* **2008**, *94*, 314–331.
- (2) Cabana, J.; Monconduit, L.; Larcher, D.; Palacin, M. R. Beyond Intercalation-Based Li-Ion Batteries: the State of the Art and Challenges of Electrode Materials Reacting Through Conversion Reactions. *Adv Mater* **2010**, *22*, E170–E192.
- (3) Anthony Burrell, A. Addressing the Voltage Fade Issue with Li-Mn Rich Oxide Cathode Materials. **2013**, 1–31.
- (4) Seid, K.-A.; Badot, J.-C.; Perca, C.; Dubrunfaut, O.; Soudan, P.; Guyomard, D.; Lestriez, B. An in Situ Multiscale Study of Ion and Electron Motion in a Lithium-Ion Battery Composite Electrode. *Adv. Energy Mater.* **2014**, 1400903–1400913.
- (5) Girishkumar, G.; McCloskey, B.; Luntz, A. C.; Swanson, S.; Wilcke, W. Lithium–Air Battery: Promise and Challenges. *J. Phys. Chem. Lett.* **2010**, *1*, 2193–2203.
- (6) Capsoni, D.; Bini, M.; Ferrari, S.; Quartarone, E.; Mustarelli, P. Recent Advances in the Development of Li–Air Batteries. *J Power Sources* **2012**, *220*, 253–263.
- (7) Lithium-Sulfur Cells: the Gap Between the State-of-the-Art and the Requirements for High Energy Battery Cells. **2015**, 1401986–1401997.
- (8) Gallagher, K. G.; Goebel, S.; Greszler, T.; Mathias, M.; Oelerich, W.; Eroglu, D.; Srinivasan, V. Quantifying the Promise of Lithium–Air Batteries for Electric Vehicles. *Energy Environ. Sci.* **2014**, *7*, 1555.
- (9) McDowell, M. T.; Lee, S. W.; Nix, W. D.; Cui, Y. 25th Anniversary Article: Understanding the Lithiation of Silicon and Other Alloying Anodes for Lithium-Ion Batteries. *Adv Mater* **2013**, *25*, 4966–4985.
- (10) Chan, C. K.; Peng, H.; Liu, G.; McIlwrath, K.; Zhang, X. F.; Huggins, R. A.; Cui, Y. High-Performance Lithium Battery Anodes Using Silicon Nanowires. *Nat Nanotech* **2008**, *3*, 31–35.
- (11) Sun, C.-F.; Karki, K.; Jia, Z.; Liao, H.; Li, T.; Qi, Y.; Cumings, J.; Rubloff, G. W. A Beaded-String Silicon Anode. *ACS Nano* **2013**, *7*, 2717–2724.
- (12) Tarascon, J.-M.; Armand, M. Issues and Challenges Facing Rechargeable Lithium Batteries. *Nature Communications* **2001**, *414*, 359–357.
- (13) Banerjee, P.; Perez, I.; Henn-Lecordier, L.; Lee, S. B.; Rubloff, G. W. Nanotubular Metal-Insulator–Metal Capacitor Arrays for Energy Storage. *Nature Nanotechnology Letters* **2009**, *4*, 292–296.
- (14) Liu, R.; Lee, S. B. MnO₂/Poly(3,4-Ethylenedioxythiophene) Coaxial Nanowires by One-Step Coelectrodeposition for Electrochemical Energy Storage. *J. Am. Chem. Soc* **2008**, *130*, 2942–2943.
- (15) Liu, C.; Gillette, E. I.; Chen, X.; Pearse, A. J.; Kozen, A. C.; Schroeder, M. A.; Gregorczyk, K. E.; Lee, S. B.; Rubloff, G. W. An All-in-One Nanopore Battery Array. *Nature Publishing Group* **2014**, *9*, 1031–1039.
- (16) Ceder, G.; Hautier, G.; Jain, A.; Ong, S. P. Recharging Lithium Battery Research with First-Principles Methods. *MRS Bull.* **2011**, *36*, 185–191.

- (17) Zhu, Y.-R.; Yin, L.-C.; Yi, T.-F.; Liu, H.; Xie, Y.; Zhu, R.-S. Electrochemical Performance and Lithium-Ion Intercalation Kinetics of Submicron-Sized Li₄Ti₅O₁₂ Anode Material. *Journal of Alloys and Compounds* **2013**, *547*, 107–112.
- (18) Lee, J. L.; Chemistruck, A.; Plett, G. L. One-Dimensional Physics-Based Reduced-Order Model of Lithium-Ion Dynamics. *J Power Sources* **2012**, *220*, 430–448.
- (19) Yabuuchi, N.; Makimura, Y.; Ohzuku, T. Solid-State Chemistry and Electrochemistry of LiCo_{1/3}Ni_{1/3}Mn_{1/3}O₂ for Advanced Lithium-Ion Batteries. *J Electrochem Soc* **2007**, *154*, A314.
- (20) Thackeray, M. M.; Kang, S.-H.; Johnson, C. S.; Vaughey, J. T.; Benedek, R.; Hackney, S. A. Li₂MnO₃-Stabilized LiMO₂ (M = Mn, Ni, Co) Electrodes for Lithium-Ion Batteries. *J. Mater. Chem.* **2007**, *17*, 3112.
- (21) Yamada, A.; Chung, S. C.; Hinokuma, K. Optimized LiFePO₄ for Lithium Battery Cathodes. *J Electrochem Soc* **2001**, *148*, A224.
- (22) Simon, P.; Gogotsi, Y. Materials for Electrochemical Capacitors. *Nature Materials* **2008**, *7*, 845–854.
- (23) Kasavajjula, U.; Wang, C.; Appleby, A. Nano-and Bulk-Silicon-Based Insertion Anodes for Lithium-Ion Secondary Cells. *J Power Sources* **2007**, *163*, 1003–1039.
- (24) Liu, R.; Lee, S. B. MnO₂/Poly(3,4-Ethylenedioxythiophene) Coaxial Nanowires by One-Step Coelectrodeposition for Electrochemical Energy Storage. *J. Am. Chem. Soc* **2008**, *130*, 2942–2943.
- (25) Liu, R.; Duay, J.; Lane, T.; Bok Lee, S. Synthesis and Characterization of RuO₂/Poly(3,4-Ethylenedioxythiophene) Composite Nanotubes for Supercapacitors. *Phys. Chem. Chem. Phys.* **2010**, *12*, 4309.
- (26) Patrissi, C. J.; Martin, C. R. Improving the Volumetric Energy Densities of Nanostructured v[Sub 2]O[Sub 5] Electrodes Prepared Using the Template Method. *J Electrochem Soc* **2001**, *148*, A1247.
- (27) Ye, J.-S.; Cui, H. F.; Liu, X.; Lim, T. M.; Zhang, W.-D.; Sheu, F.-S. Preparation and Characterization of Aligned Carbon Nanotube-Ruthenium Oxide Nanocomposites for Supercapacitors. *Small* **2005**, *1*, 560–565.
- (28) Taberna, P. L.; Mitra, S.; Poizot, P.; Simon, P.; Tarascon, J.-M. High Rate Capabilities Fe₃O₄-Based Cu Nano-Architected Electrodes for Lithium-Ion Battery Applications. *Nature Materials* **2006**, *5*, 567–573.
- (29) Wang, W.; Kumta, P. N. Nanostructured Hybrid Silicon/Carbon Nanotube Heterostructures: Reversible High-Capacity Lithium-Ion Anodes. *ACS Nano* **2010**, *4*, 2233–2241.
- (30) Li, N. A High-Rate, High-Capacity, Nanostructured Tin Oxide Electrode. *Electrochemical and Solid State Letters* **1999**, *3*, 316.
- (31) Liu, R.; Cho, S. I.; Lee, S. B. Poly(3,4-Ethylenedioxythiophene) Nanotubes as Electrode Materials for a High-Powered Supercapacitor. *Nanotechnology* **2008**, *19*, 215710.
- (32) Reddy, A. L. M.; Shaijumon, M. M.; Gowda, S. R.; Ajayan, P. M. Coaxial MnO₂/Carbon Nanotube Array Electrodes for High-Performance Lithium Batteries. *Nano Lett* **2009**, *9*, 1002–1006.

- (33) Li, N.; Martin, C. R.; Scrosati, B. Nanomaterial-Based Li-Ion Battery Electrodes. *J Power Sources* **2001**, *97*, 240–243.
- (34) Hu, Y.-S.; Liu, X.; Müller, J.-O.; Schlögl, R.; Maier, J.; Su, D. S. Synthesis and Electrode Performance of Nanostructured V_2O_5 by Using a Carbon Tube-in-Tube as a Nanoreactor and an Efficient Mixed-Conducting Network. *Angew. Chem. Int. Ed.* **2008**, *48*, 210–214.
- (35) Hughes, M.; Shaffer, M. S.; Renouf, A. C.; Singh, C.; Chen, G. Z.; Fray, D. J.; Windle, A. H. Electrochemical Capacitance of Nanocomposite Films Formed by Coating Aligned Arrays of Carbon Nanotubes with Polypyrrole. *Adv Mater* **2002**, *14*, 382–385.
- (36) Long, J.; Dunn, B.; Rolison, D.; White, H. Three-Dimensional Battery Architectures. *Chemical Reviews* **2004**, *104*, 4463–4492.
- (37) Ruzmetov, D.; Oleshko, V. P.; Haney, P. M.; Lezec, H. J.; Karki, K.; Baloch, K. H.; Agrawal, A. K.; Davydov, A. V.; Krylyuk, S.; Liu, Y.; et al. Electrolyte Stability Determines Scaling Limits for Solid-State 3D Li Ion Batteries. *Nano Lett* **2012**, *12*, 505–511.
- (38) Arthur, T. S.; Bates, D. J.; Cirigliano, N.; Johnson, D. C.; Malati, P.; Mosby, J. M.; Perre, E.; Rawls, M. T.; Prieto, A. L.; Dunn, B. Three-Dimensional Electrodes and Battery Architectures. *MRS Bull.* **2011**, *36*, 523–531.
- (39) Rubloff, G. W.; Kozen, A. C.; Bok Lee, S. From Nanoscience to Solutions in Electrochemical Energy Storage. *J. Vac. Sci. Technol. A* **2013**, *31*, 1–21.
- (40) Chen, X.; Zhu, H.; Chen, Y.-C.; Shang, Y.; Cao, A.; Hu, L.; Rubloff, G. W. MWCNT/ V_2O_5 Core/Shell Sponge for High Areal Capacity and Power Density Li-Ion Cathodes. *ACS Nano* **2012**, *6*, 7948–7955.
- (41) Gerasopoulos, K.; Chen, X.; Culver, J.; Wang, C. Self-Assembled Ni/ TiO_2 Nanocomposite Anodes Synthesized via Electroless Plating and Atomic Layer Deposition on Biological Scaffolds. *Chem. Commun.* **2010**.
- (42) Knoops, H. C. M.; Donders, M. E.; Sanden, M. C. M. V. de; Notten, P. H. L.; Kessels, W. M. M. Atomic Layer Deposition for Nanostructured Li-Ion Batteries. *J. Vac. Sci. Technol. A* **2012**, *30*, 010801.
- (43) George, S. M. Atomic Layer Deposition: an Overview. *Chem. Rev.* **2010**, *110*, 111–131.
- (44) Leung, K. First-Principles Modeling of the Initial Stages of Organic Solvent Decomposition on $\text{Li}_x\text{Mn}_2\text{O}_4$ (100) Surfaces. *J Phys Chem C* **2012**, *116*, 9852–9861.
- (45) Notten, P.; Roozeboom, F.; Niessen, R.; Baggetto, L. 3-D Integrated All-Solid-State Rechargeable Batteries. *Adv Mater* **2007**, *19*, 4564–4567.
- (46) Bates, J.; Dudney, N.; Neudecker, B.; Ueda, A.; Evans, C. Thin-Film Lithium and Lithium-Ion Batteries. *Solid State Ionics* **2000**, *135*, 33–45.
- (47) Oleshko, V. P.; Lam, T.; Ruzmetov, D.; Haney, P.; Lezec, H. J.; Davydov, A. V.; Krylyuk, S.; Cumings, J.; Talin, A. A. Miniature All-Solid-State Heterostructure Nanowire Li-Ion Batteries as a Tool for Engineering and Structural Diagnostics of Nanoscale Electrochemical Processes. *Nanoscale* **2014**, *6*, 11756–11768.

- (48) Oudenhoven, J. F. M.; Baggetto, L.; Notten, P. H. L. All-Solid-State Lithium-Ion Microbatteries: a Review of Various Three-Dimensional Concepts. *Adv. Energy Mater.* **2010**, *1*, 10–33.
- (49) Kotobuki, M.; Kanamura, K. Fabrication of All-Solid-State Battery Using Li. *Ceramics International* **2013**, *39*, 6481–6487.
- (50) Goncalves, L. M.; Ribeiro, J. F.; Silva, M. F.; Silva, M. M.; Correia, J. H. Integrated Solid-State Film Lithium Battery. *Procedia Engineering* **2010**, *5*, 778–781.
- (51) Baggetto, L.; Niessen, R. A. H.; Roozeboom, F.; Notten, P. H. L. High Energy Density All-Solid-State Batteries: a Challenging Concept Towards 3D Integration. *Adv. Funct. Mater.* **2008**, *18*, 1057–1066.
- (52) Chen, X.; Pomerantseva, E.; Banerjee, P.; Gregorczyk, K.; Ghodssi, R.; Rubloff, G. Ozone-Based Atomic Layer Deposition of Crystalline V₂O₅ Films for High Performance Electrochemical Energy Storage. *Chem Mater* **2012**, *24*, 1255–1261.
- (53) Gregorczyk, K.; Henn-Lecordier, L.; Gatineau, J.; Dussarrat, C.; Rubloff, G. Atomic Layer Deposition of Ruthenium Using the Novel Precursor Bis(2,6,6-Trimethyl-Cyclohexadienyl)Ruthenium. *Chem Mater* **2011**, *23*, 2650–2656.
- (54) Gregorczyk, K. Atomic Layer Deposition of RuO₂: New Process Development and Electrochemical Characterizations of 3D MWCNT/RuO₂ Core/Shell Battery Electrodes; Manuscript in prep., 2013.
- (55) Jung, Y. S.; Cavanagh, A. S.; Riley, L. A.; Kang, S.-H.; Dillon, A. C.; Groner, M. D.; George, S. M.; Lee, S.-H. Ultrathin Direct Atomic Layer Deposition on Composite Electrodes for Highly Durable and Safe Li-Ion Batteries. *Adv Mater* **2010**, *22*, 2172–2176.
- (56) He, Y.; Yu, X.; Wang, Y.; Li, H.; Huang, X. Alumina-Coated Patterned Amorphous Silicon as the Anode for a Lithium-Ion Battery with High Coulombic Efficiency. *Adv Mater* **2011**, *23*, 4938–4941.
- (57) Xu, W.; Vegunta, S. S. S.; Flake, J. C. Surface-Modified Silicon Nanowire Anodes for Lithium-Ion Batteries. *J Power Sources* **2011**, *196*, 8583–8589.
- (58) Snyder, M. Q.; Trebukhova, S. A.; Ravdel, B.; Wheeler, M. C.; DiCarlo, J.; Tripp, C. P.; DeSisto, W. J. Synthesis and Characterization of Atomic Layer Deposited Titanium Nitride Thin Films on Lithium Titanate Spinel Powder as a Lithium-Ion Battery Anode. *J Power Sources* **2007**, *165*, 379–385.
- (59) Luan, X. X.; Guan, D. D.; Wang, Y. Y. Enhancing High-Rate and Elevated-Temperature Performances of Nano-Sized and Micron-Sized LiMn₂O₄ in Lithium-Ion Batteries with Ultrathin Surface Coatings. *Journal of Nanoscience and Nanotechnology* **2012**, *12*, 7113–7120.
- (60) Jung, Y.; Cavanagh, A.; Dillon, A.; Groner, M.; George, S.; Lee, S. Enhanced Stability of LiCoO Cathodes in Lithium-Ion Batteries Using Surface Modification by Atomic Layer Deposition. *J Electrochem Soc* **2010**, *157*, A75.
- (61) Liu, D.; Liu, Y.; Candelaria, S. L.; Cao, G.; Liu, J.; Jeong, Y.-H. Atomic Layer Deposition of Al₂O₃ on V₂O₅ Xerogel Film for Enhanced Lithium-Ion Intercalation Stability. *J. Vac. Sci. Technol. A* **2012**, *30*, 01A123.

- (62) Sherrill, S. A.; Duay, J.; Gui, Z.; Banerjee, P.; Rubloff, G. W.; Lee, S. B. MnO₂/TiN Heterogeneous Nanostructure Design for Electrochemical Energy Storage. *Phys. Chem. Chem. Phys.* **2011**, *13*, 15221.
- (63) Chiu, K. F.; Chen, C. C.; Lin, K. M.; Lo, C. C.; Lin, H. C.; Ho, W. H.; Jiang, C. S. Lithium Phosphorus Oxynitride Solid-State Thin-Film Electrolyte Deposited and Modified by Bias Sputtering and Low Temperature Annealing. *J. Vac. Sci. Technol. A* **2010**, *28*, 568.
- (64) Dudney, N. J. Addition of a Thin-Film Inorganic Solid Electrolyte (Lipon) as a Protective Film in Lithium Batteries with a Liquid Electrolyte. *J Power Sources* **2000**, *89*, 176–179.
- (65) Mascaraque, N.; Fierro, J.; Durán, A.; Muñoz, F. An Interpretation for the Increase of Ionic Conductivity by Nitrogen Incorporation in LiPON Oxynitride Glasses. *Solid State Ionics* **2013**, *233*, 73–79.
- (66) West, W. C.; Whitacre, J. F.; Lim, J. R. Chemical Stability Enhancement of Lithium Conducting Solid Electrolyte Plates Using Sputtered LiPON Thin Films. *J Power Sources* **2004**, *126*, 134–138.
- (67) Song, J.; Jacke, S.; Becker, D.; Hausbrand, R.; Jaegermann, W. Stabilization of Thin Film LiCoO Electrode by LiPON Coating. *Electrochemical and Solid State Letters* **2011**, *14*, A11.
- (68) Knauth, P. Inorganic Solid Li Ion Conductors: an Overview. *Solid State Ionics* **2009**, *180*, 911–916.
- (69) Meda, L.; Maxie, E. E. Thin Solid Films. *Thin Solid Films* **2012**, *520*, 1799–1803.
- (70) Mascaraque, N.; Tricot, G.; Revel, B.; Durán, A.; Muñoz, F. Nitrogen and Fluorine Anionic Substitution in Lithium Phosphate Glasses. *Solid State Ionics* **2014**, *254*, 40–47.
- (71) Fergus, J. W. Ceramic and Polymeric Solid Electrolytes for Lithium-Ion Batteries. *J Power Sources* **2010**, *195*, 4554–4569.
- (72) Senevirathne, K.; Day, C. S.; Gross, M. D.; Lachgar, A.; Holzwarth, N. A. W. Solid State Ionics. *Solid State Ionics* **2013**, *233*, 95–101.
- (73) Holzwarth, N. A. W.; Du, Y. A. Prediction of a New Material – Lithium Phosphorus Oxynitride – Li, 2010, 1–13.
- (74) Dan, P.; Mengeritski, E.; Geronov, Y.; Aurbach, D. Performances and Safety Behaviour of Rechargeable AA-Size Li/Li X MnO₂ Cell. *J Power Sources* **1995**, *54*, 143–145.
- (75) Xu, K. Nonaqueous Liquid Electrolytes for Lithium-Based Rechargeable Batteries. *Chem. Rev.* **2004**, *104*, 1–116.
- (76) Mao, H. Polymerizable Aromatic Additives for Overcharge Protection in Non-Aqueous Rechargeable Lithium Batteries. 5879834, 1999.
- (77) Arora, P.; White, R. Capacity Fade Mechanisms and Side Reactions in Lithium-Ion Batteries. *J Electrochem Soc* **1998**, *145*, 3647–3667.
- (78) Wujcik, K. H.; Velasco-Velez, J.; Wu, C. H.; Pascal, T.; Teran, A. A.; Marcus, M. A.; Cabana, J.; Guo, J.; Prendergast, D.; Salmeron, M.; et al. Fingerprinting

Lithium-Sulfur Battery Reaction Products by X-Ray Absorption Spectroscopy. *J Electrochem Soc* **2014**, *161*, A1100–A1106.

(79) Heine, J.; Krüger, S.; Hartnig, C.; Wietelmann, U.; Winter, M.; Bieker, P. Coated Lithium Powder (CLiP) Electrodes for Lithium-Metal Batteries. *Adv. Energy Mater.* **2013**, 1–7.

(80) Marchioni, F.; Star, K.; Menke, E.; Buffeteau, T.; Servant, L.; Dunn, B.; Wudl, F. Protection of Lithium Metal Surfaces Using Chlorosilanes. *Langmuir* **2007**, *23*, 11597–11602.

(81) Choi, S. M.; Kang, I. S.; Sun, Y.-K.; Song, J.-H.; Chung, S.-M.; Kim, D.-W. Cycling Characteristics of Lithium Metal Batteries Assembled with a Surface Modified Lithium Electrode. *J Power Sources* **2013**, *244*, 363–368.

(82) WU, F.; Qian, J.; Chen, R.; Lu, J.; LI, L.; Wu, H.; Chen, J.; Zhao, T.; Ye, Y.; Amine, K. An Effective Approach to Protect Lithium Anode and Improve Cycle Performance for Li–S Batteries. *ACS Appl. Mater. Interfaces* **2014**, 15542–15549.

(83) Chung, K.-I.; Kim, W.-S.; Choi, Y.-K. Lithium Phosphorous Oxynitride as a Passive Layer for Anodes in Lithium Secondary Batteries. *Journal of Electroanalytical Chemistry* **2004**, *566*, 263–267.

(84) Zheng, G.; Lee, S. W.; Liang, Z.; Lee, H.-W.; Yan, K.; Yao, H.; Wang, H.; Li, W.; Chu, S.; Cui, Y. Interconnected Hollow Carbon Nanospheres for Stable Lithium Metal Anodes. *Nat Nanotech* **2014**, *9*, 618–623.

(85) Li, Y.; Fitch, B. Effective Enhancement of Lithium-Ion Battery Performance Using SLMP. *Electrochemistry Communications* **2011**, *13*, 664–667.

(86) Kozen, A. C.; Schroeder, M. A.; Osborn, K. D.; Lobb, C. J.; Rubloff, G. W. Examining the Role of Hydrogen in the Electrical Performance of in Situ Fabricated Metal-Insulator-Metal Trilayers Using an Atomic Layer Deposited Al₂O₃ Dielectric. *Applied Physics Letters* **2013**.

(87) Yamin, H.; Gorenshtein, A.; Penciner, J.; Sternberg, Y.; Peled, E. Lithium Sulfur Battery Oxidation/Reduction Mechanisms of Polysulfides in THF Solutions. *J Electrochem Soc* **1988**, *135*, 1045–1048.

(88) Kozen, A. C.; Kozen, A. C.; Pearse, A. J.; Lin, C. F.; Schroeder, M. A.; Lee, S. B.; Rubloff, G. W. Atomic Layer Deposition and in Situ Characterization of Ultraclean Lithium Oxide and Lithium Hydroxide. *J. Phys. Chem. C* **2014**, *118*, 27749–27753.

(89) Zheng, H.; Liu, Y.; Mao, S. X.; Wang, J.; Huang, J. Y. Beam-Assisted Large Elongation of in Situ Formed Li₂O Nanowires. *Sci. Rep.* **2012**, *2*.

(90) Yeh, J. J.; Lindau, I. Atomic Subshell Photoionization Cross Sections and Asymmetry Parameters: 1 to Z to 103. *Atomic data and nuclear data tables* **1985**, *32*, 1–155.

(91) Aspnes, D. E. Spectroscopic Ellipsometry—a Perspective. *J. Vac. Sci. Technol. A* **2013**, *31*, 058502.

(92) Oda, T.; Tanaka, S. Modeling of Li Diffusivity in Li₂O by Molecular Dynamics Simulation. *Journal of Nuclear Materials* **2009**, *386-388*, 1087–1090.

(93) Cavanagh, A. S.; Lee, Y.; Yoon, B.; George, S. Atomic Layer Deposition of LiOH and LiCO₃ Using LiOtBu as the Lithium Source. In: ECS; pp 223–229.

- (94) Putkonen, M.; Aaltonen, T.; Alnes, M.; Sajavaara, T.; Nilsen, O.; Fjellvåg, H. Atomic Layer Deposition of Lithium Containing Thin Films. *J. Mater. Chem.* **2009**, *19*, 8767.
- (95) Hoenigman, J. R.; Keil, R. G. An XPS Study of the Adsorption of Oxygen and Water Vapor on Clean Lithium Films. *Applications of surface science* **1984**, *18*, 207–222.
- (96) Dinh, L. N.; McLean, W., II; Schildbach, M. A.; LeMay, J. D.; Siekhaus, W. J.; Balooch, M. The Nature and Effects of the Thermal Stability of Lithium Hydroxide. *Journal of Nuclear Materials* **2003**, *317*, 175–188.
- (97) Yao, K. P. C.; Kwabi, D. G.; Quinlan, R. A.; Mansour, A. N.; Grimaud, A.; Lee, Y. L.; Lu, Y. C.; Shao-Horn, Y. Thermal Stability of Li₂O₂ and Li₂O for Li-Air Batteries: in Situ XRD and XPS Studies. *J Electrochem Soc* **2013**, *160*, A824–A831.
- (98) Donders, M. E.; Arnoldbik, W. M.; Knoops, H. C. M.; Kessels, W. M. M.; Notten, P. H. L. Atomic Layer Deposition of LiCoO₂ Thin-Film Electrodes for All-Solid-State Li-Ion Micro-Batteries. *J Electrochem Soc* **2013**, *160*, A3066–A3071.
- (99) Comstock, D. J.; Elam, J. W. Mechanistic Study of Lithium Aluminum Oxide Atomic Layer Deposition. *J Phys Chem C* **2013**, *117*, 1677–1683.
- (100) Gurvich, L. V.; Bergman, G. A.; Gorokhov, L. N.; Iorish, V. S.; Leonidov, V. Y.; Yungman, V. S. Thermodynamic Properties of Alkali Metal Hydroxides. Part 1. Lithium and Sodium Hydroxides. *Journal of Physical and Chemical Reference Data* **1996**, *25*, 1211.
- (101) Dinh, L. N.; Cecala, C. M.; Leckey, J. H.; Balooch, M. The Effects of Moisture on LiD Single Crystals Studied by Temperature-Programmed Decomposition. *Journal of Nuclear Materials* **2001**, *295*, 193–204.
- (102) Mosqueda, H. A.; Vazquez, C.; Bosch, P.; Pfeiffer, H. Chemical Sorption of Carbon Dioxide (CO₂) on Lithium Oxide (Li₂O). *Chem Mater* **2006**, *18*, 2307–2310.
- (103) Liu, J.; Liu, J.; Banis, M. N.; Banis, M. N.; Sun, Q.; Sun, Q.; Lushington, A.; Lushington, A.; Li, R.; Li, R.; et al. Rational Design of Atomic-Layer Deposited LiFePO₄ as a High Performance Cathode for Lithium Ion Batteries. *Adv Mater* **2014**.
- (104) Aaltonen, T.; Alnes, M.; Nilsen, O.; Costelle, L.; Fjellvåg, H. Lanthanum Titanate and Lithium Lanthanum Titanate Thin Films Grown by Atomic Layer Deposition. *J. Mater. Chem.* **2010**, *20*, 2877.
- (105) Hamalainen, J.; Holopainen, J.; Munnik, F. Lithium Phosphate Thin Films Grown by Atomic Layer Deposition. *J Electrochem Soc* **2012**, *159*, A259–A263.
- (106) Xie, J.; Oudenhoven, J. F. M.; Harks, P. P. R. M. L.; Li, D.; Notten, P. H. L. Chemical Vapor Deposition of Lithium Phosphate Thin-Films for 3D All-Solid-State Li-Ion Batteries. *J Electrochem Soc* **2014**, *162*, A249–A254.
- (107) Dudney, N. J.; Gruzalski, G. R.; Zuhr, R. A.; Choudhury, A.; Luck, C. F.; Robertson, J. D. Fabrication and Characterization of Amorphous Lithium Electrolyte Thin-Films and Rechargeable Thin-Film Batteries. *J Power Sources* **1993**, *43*, 103–110.
- (108) Belous, A. G.; V'yunov, O. I.; Kovalenko, L. L.; Bohnke, O.; Bohnke, C. Synthesis of Thin-Film Electrodes Based on LiPON and LiPON-LLTO-LiPON. *Russ J Electrochem* **2014**, *50*, 523–530.

- (109) Li, J.; Baggetto, L.; Martha, S. K.; Veith, G. M.; Nanda, J.; Liang, C.; Dudney, N. J. An Artificial Solid Electrolyte Interphase Enables the Use of a LiNi_{0.5}Mn_{1.5}O₄ Cathode with Conventional Electrolytes. *Adv. Energy Mater.* **2013**, *3*, 1275–1278.
- (110) Nowak, S.; Berkemeier, F.; Schmitz, G. Ultra-Thin LiPON Films - Fundamental Properties and Application in Solid State Thin Film Model Batteries. *J Power Sources* **2015**, *275*, 144–150.
- (111) Kim, Y. G.; Wadley, H. N. G. The Influence of the Nitrogen-Ion Flux on Structure and Ionic Conductivity of Vapor Deposited Lithium Phosphorus Oxynitride Films. *J Power Sources* **2011**, *196*, 1371–1377.
- (112) Kim, H. T.; Mun, T.; Park, C.; Jin, S. W.; Park, H. Y. Characteristics of Lithium Phosphorous Oxynitride Thin Films Deposited by Metal-Organic Chemical Vapor Deposition Technique. *J Power Sources* **2013**, *244*, 641–645.
- (113) Gregorczyk, K. E.; Kozen, A. C.; Chen, X.; Schroeder, M. A.; Cao, A.; Hu, L.; Rubloff, G. W. Fabrication of 3D Core-Shell Multiwalled Carbon Nanotube@RuO₂ Lithium-Ion Battery Electrodes Through a RuO₂ Atomic Layer Deposition Process. *ACS Nano* **2014**, 141222111241002.
- (114) Perng, Y.-C.; Cho, J.; Sun, S. Y.; Membreno, D.; Cirigliano, N.; Dunn, B.; Chang, J. P. Synthesis of Ion Conducting Li_xAl_ySi_zO Thin Films by Atomic Layer Deposition. *J. Mater. Chem. A* **2014**, *2*, 9566.
- (115) Zheng, Z.; Fang, H.; Yang, F.; Liu, Z. K.; Wang, Y. Amorphous LiLaTiO₃ as Solid Electrolyte Material. *J Electrochem Soc* **2014**, *161*, A473–A479.
- (116) Roh, N. S.; Lee, S. D.; Kwon, H. S. Effects of Deposition Condition on the Ionic Conductivity and Structure of Amorphous Lithium Phosphorus Oxynitrate Thin Film. *Scripta Mater* **1999**, *42*, 43–49.
- (117) Inner-Orbital Photoelectron Spectroscopy of the Alkali Metal Halides, Perchlorates, Phosphates, and Pyrophosphates. **1973**, *95*, 751–755.
- (118) Investigation of the Local Structure of LiPON Thin Films to Better Understand the Role of Nitrogen on Their Performance. **2011**, *186*, 29–36.
- (119) Westwater, J. Growth of Silicon Nanowires via Gold/Silane Vapor–Liquid–Solid Reaction. *J Vac Sci Technol B* **1997**, *15*, 554.
- (120) Givargizov, E. I. Fundamental Aspects of VLS Growth. *Journal of Crystal Growth* **1975**, *31*, 20–30.
- (121) Li, J.; Dudney, N. J.; Nanda, J.; Liang, C. Artificial Solid Electrolyte Interphase to Address the Electrochemical Degradation of Silicon Electrodes. *ACS Appl. Mater. Interfaces* **2014**, *6*, 10083–10088.
- (122) Yu, X. A Stable Thin-Film Lithium Electrolyte: Lithium Phosphorus Oxynitride. *J Electrochem Soc* **1997**, *144*, 524–532.
- (123) Vlasiouk, I.; Smirnov, S.; Siwy, Z. Ionic Selectivity of Single Nanochannels. *Nano Lett* **2008**, *8*, 1978–1985.
- (124) Vlasiouk, I.; Smirnov, S.; Siwy, Z. Nanofluidic Ionic Diodes. Comparison of Analytical and Numerical Solutions. *ACS Nano* **2008**, *2*, 1589–1602.
- (125) Gamble, T.; Decker, K.; Plett, T. S.; Pevarnik, M.; Pietschmann, J.-F.; Vlasiouk, I.; Aksimentiev, A.; Siwy, Z. S. Rectification of Ion Current in Nanopores

Depends on the Type of Monovalent Cations: Experiments and Modeling. *J Phys Chem C* **2014**, *118*, 9809–9819.

(126) Verma, P.; Maire, P.; Novak, P. *Electrochimica Acta*. *Electrochimica Acta* **2010**, *55*, 6332–6341.

(127) Cresce, A. V.; Russell, S. M.; Baker, D. R.; Gaskell, K. J.; Xu, K. In Situ and Quantitative Characterization of Solid Electrolyte Interphases. *Nano Lett* **2014**, *14*, 1405–1412.

(128) Steiger, J.; Richter, G.; Wenk, M.; Kramer, D.; Mönig, R. Comparison of the Growth of Lithium Filaments and Dendrites Under Different Conditions. *Electrochemistry Communications* **2015**, *50*, 11–14.

(129) Lee, J.-T.; Wang, F.-M.; Cheng, C.-S.; Li, C.-C.; Lin, C.-H. Low-Temperature Atomic Layer Deposited Al₂O₃ Thin Film on Layer Structure Cathode for Enhanced Cycleability in Lithium-Ion Batteries. *Electrochimica Acta* **2010**, *55*, 4002–4006.

(130) Zhang, X.; Belharouak, I.; LI, L.; Lei, Y.; Elam, J. W.; Nie, A.; Chen, X.; Yassar, R. S.; Axelbaum, R. L. Structural and Electrochemical Study of Al₂O₃ and TiO₂ Coated Li_{1.2}Ni_{0.13}Mn_{0.54}Co_{0.13}O₂ Cathode Material Using ALD. *Adv. Energy Mater.* **2013**, *3*, 1299–1307.

(131) Zhao, J. Q.; Wang, Y. Ultrathin Surface Coatings for Improved Electrochemical Performance of Lithium Ion Battery Electrodes at Elevated Temperature. *J Phys Chem C* **2012**, *116*, 11867–11876.

(132) Nagao, M.; Hayashi, A.; Tatsumisago, M. *Electrochemistry Communications*. *Electrochemistry Communications* **2012**, *22*, 177–180.

(133) Abdulagatov, A. I.; Yan, Y.; Cooper, J. R.; Zhang, Y.; Gibbs, Z. M.; Cavanagh, A. S.; Yang, R. G.; Lee, Y. C.; George, S. M. Al₂O₃ and TiO₂ Atomic Layer Deposition on Copper for Water Corrosion Resistance. *ACS Appl. Mater. Interfaces* **2011**, *3*, 4593–4601.

(134) Wang, P. C.; Shih, Y. T.; Lin, M. C.; Lin, H. C.; Chen, M. J.; Lin, K. M. A Study of Atomic Layer Deposited LiAl_xO_y Films on Mg–Li Alloys. *Thin Solid Films* **2010**, *518*, 7501–7504.

(135) Marin, E.; Guzman, L.; Lanzutti, A.; Ensinger, W.; Fedrizzi, L. Multilayer Al₂O₃/TiO₂ Atomic Layer Deposition Coatings for the Corrosion Protection of Stainless Steel. *Thin Solid Films* **2012**, *522*, 283–288.

(136) Park, M.; Oh, S.; Kim, H.; Jung, D.; Choi, D.; Park, J.-S. Thin Solid Films. *Thin Solid Films* **2013**, *546*, 153–156.

(137) Bertrand, J. A.; George, S. M. Evaluating Al₂O₃ Gas Diffusion Barriers Grown Directly on Ca Films Using Atomic Layer Deposition Techniques. *J. Vac. Sci. Technol. A* **2013**, *31*, 01A122.

(138) Memarzadeh Lotfabad, E.; Kalisvaart, P.; Cui, K.; Kohandehghan, A.; Kupsta, M.; Olsen, B.; Mitlin, D. ALD TiO₂ Coated Silicon Nanowires for Lithium Ion Battery Anodes with Enhanced Cycling Stability and Coulombic Efficiency. *Phys. Chem. Chem. Phys.* **2013**, *15*, 13646–13657.

- (139) Riley, L.; Cavanagh, A.; George, S.; Lee, S.; Dillon, A. Improved Mechanical Integrity of ALD-Coated Composite Electrodes for Li-Ion Batteries. *Electrochemical and Solid State Letters* **2011**, *14*, A29.
- (140) Riley, L. A.; Cavanagh, A. S.; Cavanagh, A. S.; George, S. M.; George, S. M.; Jung, Y. S.; Lee, S.-H.; Dillon, A. C. Conformal Surface Coatings to Enable High Volume Expansion Li Ion Anode Materials. *Chem Phys Chem* **2010**, 2124–2130.
- (141) Atta, S. V.; Cavanagh, A. S.; George, S. M.; Liu, P.; Dillon, A. C.; Lee, S.-H. Electrochemical Effects of ALD Surface Modification on Combustion Synthesized LiNi_{1/3} Mn_{1/3} Co_{1/3} O₂ as a Layered-Cathode Material. *J Power Sources* **2011**, *196*, 3317–3324.
- (142) Kim, H.; Lee, J. T.; Lee, D.-C.; Magasinski, A.; Cho, W.-I.; Yushin, G. Plasma-Enhanced Atomic Layer Deposition of Ultrathin Oxide Coatings for Stabilized Lithium-Sulfur Batteries. *Adv. Energy Mater.* **2013**, *3*, 1308–1315.
- (143) Jung, S. C.; Han, Y.-K. How Do Li Atoms Pass Through the Al₂O₃ Coating Layer During Lithiation in Li-Ion Batteries? *J. Phys. Chem. Lett.* **2013**, *4*, 2681–2685.
- (144) Aurbach, D.; Aurbach, D.; Talyosef, Y.; Talyosef, Y.; Markovsky, B.; Markovsky, B.; Markevich, E.; Markevich, E.; Zinigrad, E.; Asraf, L.; et al. Design of Electrolyte Solutions for Li and Li-Ion Batteries: a Review. *Electrochimica Acta* **2004**.
- (145) Peng, Z.; Freunberger, S. A.; Chen, Y.; Bruce, P. G. A Reversible and Higher-Rate Li-O₂ Battery. *Science* **2012**.
- (146) Holzapfel, M.; Wuersig, A.; Scheifele, W.; Vetter, J.; Novak, P. Oxygen, Hydrogen, Ethylene and CO₂ Development in Lithium-Ion Batteries. *J Power Sources* **2007**, *174*, 1156–1160.
- (147) Bieker, G.; Bieker, P. M.; Winter, M. Electrochemical in Situ Investigations of the SEI and Dendrite Formation on the Lithium Metal Anode. *Phys. Chem. Chem. Phys.* **2015**, 1–13.
- (148) Han, X.; Xu, Y.; Chen, X.; Chen, Y.-C.; Weadock, N.; Wan, J.; Zhu, H.; Liu, Y.; Li, H.; Rubloff, G.; et al. Reactivation of Dissolved Polysulfides in Li-S Batteries Based on Atomic Layer Deposition of Al. *Nano Energy* **2013**, 1–10.
- (149) Zhou, G.; Zhao, Y.; Manthiram, A. Dual Confined Flexible Sulfur Cathodes Encapsulated in Nitrogen Doped Double Shelled Hollow Carbon Spheres and Wrapped with Graphene for Li-S Batteries. *Adv. Energy Mater.* **2015**, 1402263–1402273.
- (150) Elazari, R.; Salitra, G.; Garsuch, A.; Panchenko, A.; Aurbach, D. Sulfur-Impregnated Activated Carbon Fiber Cloth as a Binder-Free Cathode for Rechargeable Li-S Batteries. *Adv Mater* **2011**, *23*, 5641–5644.
- (151) Ryu, H.; Ahn, H.; Kim, K.; Ahn, J.; Lee, J.; Cairns, E. Self-Discharge of Lithium-Sulfur Cells Using Stainless-Steel Current-Collectors. *J Power Sources* **2005**, *140*, 365–369.
- (152) Leung, K. Electronic Structure Modeling of Electrochemical Reactions at Electrode/Electrolyte Interfaces in Lithium Ion Batteries. *J Phys Chem C* **2013**, *117*, 1539–1547.
- (153) Leung, K.; Qi, Y.; Zavadil, K. R.; Dillon, A. C.; Cavanagh, A. S.; Lee, S.-H.; George, S. M. Using Atomic Layer Deposition to Hinder Solvent Decomposition in

Lithium Ion Batteries: First-Principles Modeling and Experimental Studies. *J. Am. Chem. Soc* **2011**, *133*, 14741–14754.

(154) Kessels, E.; Putkonen, M. Advanced Process Technologies: Plasma, Direct-Write, Atmospheric Pressure, and Roll-to-Roll ALD. *MRS Bull.* **2011**, *36*, 907–913.

(155) Kozen, A. C.; Lin, C.-F.; Pearse, A. J.; Schroeder, M. A.; Han, X.; Hu, L.; Lee, S. B.; Rubloff, G. W.; Noked, M. Next-Generation Lithium Metal Anode Engineering via Atomic Layer Deposition. *ACS Nano* **2015**, 150513155622005–150513155622030.

(156) Choi, J.-A.; Kim, D.-W.; Bae, Y.-S.; Song, S.-W.; Hong, S.-H.; Lee, S.-M. Electrochemical and Interfacial Behavior of a FeSi_{2.7} Thin Film Electrode in an Ionic Liquid Electrolyte. *Electrochimica Acta* **2011**, *56*, 9818–9823.

(157) Whitacre, J. F.; West, W. C.; Ratnakumar, B. V. A Combinatorial Study of Li_yMn_xNi_{2-x}O₄ Cathode Materials Using Microfabricated Solid-State Electrochemical Cells. *J Electrochem Soc* **2003**, *150*, A1676.

(158) Zhang, L.; Liu, X.; Liu, Y.; Huang, S.; Zhu, T.; Gui, L.; Wang, C.; Mao, S.; Ye, Z.; Sullivan, J. Controlling the Lithiation Induced Strain and Charging Rate in Nanowire Electrodes by Coating. *ACS Nano* **2011**, *5*, 4800–4809.

(159) Khalil, M. S.; Gladchenko, S.; Holder, A. M.; Musgrave, C. B.; Kozen, A. C.; Rubloff, G. W.; Liu, Y. Q.; Gordon, R. G.; Yum, J. H.; Banerjee, S. K.; et al. Evidence for Hydrogen Two-Level Systems in Atomic Layer Deposition Oxides. *Applied Physics Letters* **2013**, *103*, 162601.